

1 **Is a scaling factor required to obtain closure between measured and**
2 **modelled atmospheric O₄ absorptions? — An assessment of uncertainties of**
3 **measurements and radiative transfer simulations -~~ease study~~ for two days**
4 **during the MAD-CAT campaign**
5

6 Thomas Wagner¹, Steffen Beirle¹, Nuria Benavent², Tim Bösch³, Kai ~~___~~ Lok Chan⁴,
7 Sebastian Donner¹, Steffen Dörner¹, Caroline Fayt⁵, Udo Frieb⁶, David Garcia-Nieto², Clio
8 Gielen^{5*}, David González-Bartolome⁷, Laura Gomez⁷, François Hendrick⁵, Bas Henzing⁸,
9 Jun Li Jin⁹, Ted Koenig, Johannes Lampel⁶, Jianzhong Ma¹⁰, Kornelia Mies¹, Mónica
10 Navarro⁷, Ivan Ortega, Enno ~~Peters~~⁴Peters^{3**}, Gaia Pinardi⁵, Olga Puentedura⁷, Janis
11 Puķīte¹, Julia Remmers¹, Andreas Richter³, Alfonso Saiz-Lopez², Reza Shaiganfar¹, Holger
12 Sihler¹, Michel Van Roozendael⁵, Rainer Volkamer, Yang Wang¹, Margarita Yela⁷
13

14 ¹ Max Planck Institute for Chemistry, Mainz, Germany

15 ² Department of Atmospheric Chemistry and Climate, Institute of Physical Chemistry
16 Rocasolano (CSIC), Spain.

17 ³ University of Bremen, Germany

18 ⁴ Meteorological Institute, Ludwig-Maximilians-Universität München, Germany

19 ⁵ Royal Belgian Institute for Space Aeronomy (BIRA-IASB), Brussels, Belgium

20 ⁶ University of Heidelberg, Germany

21 ⁷ Instituto Nacional de Tecnica Aeroespacial (INTA), Spain

22 ⁸ TNO, Netherlands Institute for Applied Scientific Research

23 ⁹ CMA Meteorological Observation Center, China

24 ¹⁰ Chinese Academy of Meteorological Science, China

25 * currently at the Institute of Astronomy, KU Leuven, Belgium

26 ** Now at Institute for protection of maritime infrastructures, German Aerospace Center
27 (DLR), Bremerhaven, Germany
28

29
30 **Abstract**

31 In this study the consistency between MAX-DOAS measurements and radiative transfer
32 simulations of the atmospheric O₄ absorption is investigated on two mainly ~~clear~~cloud-free
33 days during the MAD-CAT campaign in Mainz, Germany, in Summer 2013. In recent years
34 several studies indicated that measurements and radiative transfer simulations of the
35 atmospheric O₄ absorption can only be brought into agreement if a so-called scaling factor
36 (<1) is applied to the measured O₄ absorption. However, many studies, ~~in particular~~including
37 such based on direct sun light measurements, came to the opposite conclusion, that there is no
38 need for a scaling factor. Up to now, there is no broad consensus for an explanation for the
39 observed discrepancies between measurements and simulations. Previous studies inferred the
40 need for a scaling factor from the comparison of the aerosol optical depth derived from MAX-
41 DOAS O₄ measurements with that derived from coincident sun photometer measurements. In
42 this study a different approach is chosen: the measured O₄ absorption at 360 nm is directly
43 compared to the O₄ absorption obtained from radiative transfer simulations. The atmospheric
44 conditions used as input for the radiative transfer simulations were taken from independent
45 data sets, in particular from sun photometer and ceilometer measurements at the measurement
46 site. ~~The comparisons are performed for two selected clear days with similar aerosol optical~~
47 ~~depth but very different aerosol properties. This study has three main goals: First For both~~
48 ~~days not only the O₄ absorptions are compared, but also~~ all relevant error sources of the

49 spectral analysis, the radiative transfer simulations as well as the extraction of the input
50 parameters used for the radiative transfer simulations are quantified. One important result
51 obtained from the analysis of synthetic spectra is that the O₄ absorptions derived from the
52 spectral analysis agree within 1% with the corresponding radiative transfer simulations at 360
53 nm. Based on the results from sensitivity studies, recommendations for optimised settings for
54 the spectral analysis and radiative transfer simulations are given.~~The performed tests and~~
55 ~~sensitivity studies might be useful for the analysis and interpretation of O₄-MAX-DOAS~~
56 ~~measurements in future studies.~~ Second, the measured and simulated results are compared
57 ~~Different comparison results are found~~ for both days: On 18 June, measurements and
58 simulations agree within their (rather large) errors (the ratio of simulated and measured O₄
59 absorptions is found to be 1.01±0.16). In contrast, on 8 July measurements and simulations
60 significantly disagree: For the middle period of that day the ratio of simulated and measured
61 O₄ absorptions is found to be ~~0.71-80~~ ±0.1210, which differs significantly from unity. Thus
62 for that day a scaling factor is needed to bring measurements and simulations into agreement.
63 Third, recommendations for further intercomparison exercises are derived. One possible
64 ~~reason for the comparison results on 18 June is the rather large aerosol extinction (and its~~
65 ~~large uncertainty) close to the surface, which has a large effect on the radiative transfer~~
66 ~~simulations.~~ One important recommendation for future studies is that aerosol profile data
67 should be measured at the same wavelengths as the MAX-DOAS measurements. Also the
68 altitude range without profile information close to the ground should be minimised and
69 detailed information of the aerosol optical and/or microphysical properties should be used.
70 Besides the inconsistent comparison results for both days, also no explanation for a O₄ scaling
71 factor could be derived in this study. Thus similar, but more extended future studies should be
72 performed, which preferably include more measurement days, and more instruments ~~and~~
73 ~~should be supported by more detailed independent aerosol measurements.~~ Also additional
74 wavelengths should be included. The MAX-DOAS measurements collected during the recent
75 CINDI-2 campaign are probably well suited for that purpose.

77 **1 Introduction**

79 Observations of the atmospheric absorption of the oxygen collision complex (O₂)₂ (in the
80 following referred to as O₄, see Greenblatt et al. (1990)) are often used to derive information
81 about atmospheric light paths from remote sensing measurements of scattered sun light (made
82 e.g. from ground, satellite, balloon or airplane). Since atmospheric radiative transport is
83 strongly influenced by scattering on aerosol and cloud particles, information on the presence
84 and properties of clouds and aerosols can be derived from O₄ absorption measurements.
85 Early studies based on O₄ measurements focussed on the effect of clouds (e.g. Erle et al.,
86 1995; Wagner et al., 1998; Winterrath et al., 1999; Acarreta et al., 2004; Sneeß et al., 2008;
87 Heue et al., 2014; Gielen et al., 2014; Wagner et al., 2014), which is usually stronger than that
88 of aerosols. Later also aerosol properties were derived from O₄ measurements, in particular
89 from Multi-AXis- (MAX-) DOAS measurements (e.g. Hönninger et al., 2004; Wagner et al.,
90 2004; Wittrock et al., 2004; Friess et al., 2004; Irie et al. Clémer 2010; Friess et al., 2016 and
91 references therein). For the retrieval of aerosol profiles usually forward model simulations for
92 various assumed aerosol profiles are compared to measured O₄ slant column densities (SCD,
93 the integrated O₄ concentration along the atmospheric light path). The aerosol profile
94 associated with the best fit between the forward model and measurement results is considered
95 as the most probable atmospheric aerosol profile (for more details, see e.g. Frieß et al., 2006).
96 Note that in some cases no unique solution might exist, if different atmospheric aerosol
97 profiles lead to the same O₄ absorptions. MAX-DOAS aerosol retrievals are typically
98 restricted to altitudes below about 4 km; see Friess et al. (2006).

99 About ten years ago, Wagner et al. (2009) suggested to apply a scaling factor (SF <1) to the
 100 O₄ SCDs derived from MAX-DOAS measurements at 360 nm in Milano in order to achieve
 101 agreement with forward model simulations. They found that on a day with low aerosol load
 102 the measured O₄ SCDs were larger than the model results, even if no aerosols were included
 103 in the model simulations. If, however, the measured O₄ SCDs were scaled by a SF of 0.81,
 104 good agreement with the forward model simulations (and nearby AERONET measurements)
 105 was achieved. Similar findings were then reported by Clémer et al. (2010), who suggested a
 106 SF of 0.8 for MAX-DOAS measurements in Beijing. Interestingly, they applied this SF to
 107 four different O₄ absorption bands (360, 477, 577, and 630 nm).
 108 While with the application of a SF the consistency between forward model and measurements
 109 was substantially improved, both studies could not provide an explanation for the physical
 110 mechanism behind such a SF. In the following years several research groups applied a SF in
 111 their MAX-DOAS aerosol profile retrievals. However, a similarly large fraction of studies
 112 (including direct sun measurements and aircraft measurements, see Spinei et al. (2015)) did
 113 not find it necessary to apply a SF to bring measurements and forward model simulations into
 114 agreement. An overview on the application of a SF in various MAX-DOAS publications after
 115 2010 is provided in Table 1. Up to now, there is no community consensus on whether or not a
 116 SF is needed for measured O₄ SCDs. This is a rather unfortunate situation, because this
 117 ambiguity directly affects the aerosol results derived from MAX-DOAS measurements and
 118 thus the general confidence in the method.

119
 120 So far, most of the studies deduced the need for a SF in a rather indirect way: aerosol
 121 extinction profiles derived from MAX-DOAS measurements using different SF are usually
 122 compared to independent data sets (mostly AOD from sun photometer observations) and the
 123 SF leading to the best agreement is selected. In many cases SF between 0.75 and 0.9 were
 124 derived.

125 In this study, we follow a different approach: similar to Ortega et al. (2016) we directly
 126 compare the measured O₄ SCDs with the corresponding SCDs derived from a forward model.
 127 For this comparison, atmospheric conditions which are well characterised by independent
 128 measurements are chosen. Such a procedure allows in particular quantifying the influence of
 129 the errors of the individual processing steps.

130 One peculiarity of this comparison is that the measured O₄ SCDs are first converted into their
 131 corresponding air mass factors (AMF), which are defined as the ratio of the SCD and the
 132 vertical column density (VCD, the vertically integrated concentration) (Solomon et al., 1987).
 133

$$134 \quad AMF = \frac{SCD}{VCD} \quad (1)$$

135
 136 The ‘measured’ O₄ AMF is then compared to the corresponding AMF derived from radiative
 137 transfer simulations for the atmospheric conditions during the measurements:
 138

$$139 \quad AMF_{measured} = AMF_{simulated} \quad (2)$$

140
 141 The conversion of the measured O₄ SCDs into AMFs is carried out to ensure a simple and
 142 direct comparison between measurements and forward model simulations. Here it should be
 143 noted that in addition to the AMFs also so-called differential AMFs (dAMFs) will be
 144 compared in this study. The dAMFs represent the difference between AMFs for
 145 measurements at non-zenith elevation angles α and at 90° for the same elevation sequence:
 146

$$147 \quad dAMF_{\alpha} = AMF_{\alpha} - AMF_{90^{\circ}} \quad (3)$$

148
149
150
151
152
153
154
155
156
157
158
159
160
161
162
163
164
165
166
167
168
169
170
171
172
173
174
175
176
177
178
179
180
181
182
183
184
185
186
187
188
189
190
191
192
193
194
195

For the comparison between measured and simulated O₄ (d)AMFs, two mostly ~~clearcloud-free~~ days (18 June and 08 July 2013) during the Multi Axis DOAS Comparison campaign for Aerosols and Trace gases (MAD-CAT) campaign are chosen (http://joseba.mpch-mainz.mpg.de/mad_cat.htm). As discussed in more detail in section 4.2.2, based on the ceilometer and sun photometer measurements, three periods on each of both days are selected, during which the variation of the aerosol profiles was relatively small (see Table 2). In addition to the aerosol profiles, also other atmospheric properties are averaged during these periods before they are used as input for the radiative transfer simulations.

The comparison is carried out for the O₄ absorption band at 360 nm, which is the strongest O₄ absorption band in the UV. In principle also other O₄ absorption bands (e.g. in the visible spectral range) could be chosen, but these bands are not covered by the wavelength range of the MPIC instrument. Thus they are not part of this study.

Deviations between forward model and measurements can have different reasons: In the following an overview on these error sources and the way they are investigated in this study are given:

a) Calculation of O₄ profiles and O₄ VCDs (eq. 1):

Profiles and VCDs of O₄ are derived from pressure and temperature profiles. The errors of the pressure and temperature profiles are quantified by sensitivity studies and by the comparison of the extraction results derived from different groups/persons (see Table 3).

b) Calculation of O₄ (d)AMFs from radiative transfer simulations:

Besides differences between the different radiative transfer codes, the dominating error sources are the uncertainties of the input parameters. They are investigated by sensitivity studies and by the comparison of extracted input data by different groups/persons. Also the effects of operating different radiative transfer models by different groups are investigated.

c) Analysis of the O₄ (d)AMFs from MAX-DOAS measurements:

Uncertainties of the spectral analysis results are caused by errors and imperfections of the measurements/instruments, by the dependence of the analysis results on the specific fit settings, and the uncertainties of the O₄ cross sections. They are investigated by systematic variation of the DOAS fit settings (for measured and synthetic spectra), and by comparison of analysis results obtained from different groups and/or instruments.

The paper is organised as follows: in section 2, information on the selected days during the MAD-CAT campaign, on the MAX-DOAS measurements, and on the data sets from independent measurements is provided. Section 3 presents initial comparison results for the selected days using standard settings. In section 4 the uncertainties associated with each of the various processing steps of the spectral analysis and the forward model simulations are quantified. Section 5 presents a summary and conclusions.

2 MAD-CAT campaign, MAX-DOAS instruments and other data sets used in this study

The Multi Axis DOAS Comparison campaign for Aerosols and Trace gases (MAD-CAT) (http://joseba.mpch-mainz.mpg.de/mad_cat.htm) took place in June and July 2013 on the roof of the Max-Planck-Institute for Chemistry in Mainz, Germany. The main aim of the campaign was to compare MAX-DOAS retrieval results of several atmospheric trace gases like NO₂, HCHO, HONO, CHOCHO as well as aerosols. The measurement location was at 150m above sea level at the western edge of the city of Mainz.

196 2.1 MAX-DOAS instruments

197
198 During the MAD-CAT campaign, 11 MAX-DOAS instruments were operated by different
199 groups; an overview can be found at the website [http://joseba.mpch-](http://joseba.mpch-mainz.mpg.de/equipment.htm)
200 [mainz.mpg.de/equipment.htm](http://joseba.mpch-mainz.mpg.de/equipment.htm). The main viewing direction of the MAX-DOAS instruments
201 was towards north-west (51° with respect to North). Measurements at this viewing direction
202 were the main focus of this study, but a few comparisons using the ‘standard settings’ (see
203 section 3) were also carried out for three other azimuth angles (141° , 231° , 321° , see Fig. A2 I
204 in appendix A1). Each elevation sequence contains the following elevation angles: 1, 2, 3, 4,
205 5, 6, 8, 10, 15, 30 and 90° . In this study, in addition to the MPIC instrument, also spectra from
206 3 other MAX-DOAS instruments were analysed. The instrumental details are given in Table
207 4. The spectra of the MPIC instrument are available at the website [http://joseba.mpch-](http://joseba.mpch-mainz.mpg.de/e_doc_zip.htm)
208 [mainz.mpg.de/e_doc_zip.htm](http://joseba.mpch-mainz.mpg.de/e_doc_zip.htm).

210 2.2 Additional data sets

211
212 In order to constrain the radiative transfer simulations, independent measurements and data
213 sets were used. In particular, information on atmospheric pressure, temperature and relative
214 humidity, as well as aerosol properties is used. In addition to local in situ measurements from
215 air quality monitoring stations and remote sensing measurements by a ceilometer and a sun
216 photometer, also ECMWF reanalysis data were used. An overview on these data sets is given
217 in Table 5. The data sets used in this study are available at the websites [http://joseba.mpch-](http://joseba.mpch-mainz.mpg.de/a_doc_zip.htm)
218 [mainz.mpg.de/a_doc_zip.htm](http://joseba.mpch-mainz.mpg.de/a_doc_zip.htm) and http://joseba.mpch-mainz.mpg.de/c_doc_zip.htm.

220 2.3 RTM simulations

221
222 Several radiative transfer models are used to calculate O_4 (d)AMFs for the selected days. As
223 input, vertical profiles of temperature, pressure, relative humidity and aerosol extinction
224 extracted from the independent data sets (see section 2.2 and 4) were used. The vertical
225 resolution is high in the lowest layers and decreases with increasing altitude (see Table A1 in
226 appendix A1). The upper boundary of the vertical grid is set to 1000 km. The lower boundary
227 of the model grid represents the surface elevation of the instrument (150 m above sea level).
228 For the ‘standard run’, a surface albedo of 5% is assumed and the aerosol optical properties
229 are described by a Henyey-Greenstein phase function with an asymmetry parameter of 0.68
230 and a single scattering albedo of 0.95. Both values represent typical urban aerosols (see e.g.
231 Dubovik et al., 2002). Ozone absorption was not considered, because it is very small at 360
232 nm. The MAD-CAT campaign took place around summer solstice. Thus the same dependence
233 of the solar zenith angle (SZA) and relative azimuth angle (RAZI) on time is used for both
234 days (see Table A2 in the appendix A1). The input data used for the radiative transfer
235 simulations are available at the website http://joseba.mpch-mainz.mpg.de/d_doc_zip.htm. In
236 the following sub-sections the different radiative transfer models used in this study are
237 described.

240 2.3.1 MCARTIM

241
242 The full spherical Monte Carlo radiative transfer model MCARTIM (Deutschmann et al.,
243 2011) explicitly simulates individual photon trajectories including the photon interactions
244 with molecules, aerosol particles and the surface. In this study two versions of MCARTIM are
245 used: version 1 and version 3. Version 1 is a 1-D scalar model. Version 3 can also be run in 3-
246 D and vector modes. In version 1 Rotational Raman scattering (RRS) is partly taken into

247 account: the RRS cross section and phase function are explicitly considered for the
248 determination of the photon paths, but the wavelength redistribution during the RRS events is
249 not considered. In version 3 RRS can be fully taken into account. If operated in the same
250 mode (1-D scalar) both models show excellent agreement.

251

252

253 **2.3.2 LIDORT**

254

255 In this study the LIDORT version 3.3 was used. The Linearized Discrete Ordinate Radiative
256 Transfer (LIDORT) forward model (Spurr et al., 2001; Spurr et al., 2008) is based on the
257 discrete ordinate method to solve the radiative transfer equation (e.g.: Chandrasekhar, 1960;
258 Chandrasekhar, 1989; Stamnes et al., 1988). This model considers a pseudo-spherical multi-
259 layered atmosphere including several anisotropic scatters. The formulation implemented
260 corrects for the atmosphere curvature in the solar and single scattered beam, however the
261 multiple scattering term is treated in the plane-parallel approximation. The properties of each
262 of the atmospheric layers are considered homogenous in the corresponding layer. Using finite
263 differences for the altitude derivatives, this linearized code converts the problem into a linear
264 algebraic system. Through first order perturbation theory, it is able to provide radiance field
265 and radiance derivatives with respect to atmospheric and surface variables (Jacobians) in a
266 single call. LIDORT was used in several studies to derive vertical profiles of aerosols and
267 trace gases from MAX-DOAS (e.g. Clémer et al., 2010; Hendrick et al., 2014; Franco et al.,
268 2015).

269

270

271 **2.3.3 SCIATRAN**

272

273 The RTM SCIATRAN (Rozañov et al. 2014) was used in its full-spherical mode including
274 multiple scattering but without polarization. In the operation mode used here, SCIATRAN
275 solves the transfer equations using the discrete ordinate method. In this study, SCIATRAN
276 was used by two groups: The IUP Bremen group used v3.8.3 for the for the O₄ dAMFs
277 simulations (without Raman scattering). The MPIC group used v3.6.11 for the calculation of
278 synthetic spectra (see Section 2.4) and for the O₄ dAMFs simulations (including Raman
279 scattering).

280

281

282 **2.4 Synthetic spectra**

283

284 In addition to AMFs and dAMFs, also synthetic spectra were simulated. They are analysed in
285 the same way as the measured spectra, which allows the investigation of two important
286 aspects:

287 a) The derived O₄ dAMFs from the synthetic spectra can be compared to the O₄ dAMFs
288 obtained directly from the radiative simulations at one wavelength (here: 360 nm) using the
289 same settings. In this way the consistency of the spectral analysis results and the radiative
290 transfer simulations is tested.

291 b) Sensitivity tests can be performed varying several fit parameters, e.g. the spectral range or
292 the DOAS polynomial, and their effect on the derived O₄ dAMFs can be assessed.

293 Synthetic spectra are simulated using SCIATRAN taking into account rotational Raman
294 scattering. The basic simulation settings are the same as for the RTM simulations of the O₄
295 (d)AMFs described above. In order to minimise the computational effort, for the profiles of
296 temperature, pressure, relative humidity and aerosol extinction the input data for only two
297 periods (18 June: 11:00 – 14:00, 08 July: 7:00 – 11:00, see Table 2) are used for the whole

298 day. Thus ‘perfect’ agreement with the measurements can only be expected for the two
299 selected periods. Aerosol optical properties (phase function and single scattering albedo) are
300 taken from AERONET measurements of the two selected days. Although the wavelength
301 dependencies of both quantities (and also for the aerosol extinction) are considered, it should
302 be noted that the associated uncertainties are probably rather large, since the optical properties
303 in the UV had to be extrapolated from measurements in the visible spectral range. ~~Moreover,~~
304 ~~the phase functions were not available as fully consolidated AERONET level 2.0 data, but~~
305 ~~only as level 1.5 data.~~

306 Spectra were simulated at a spectral resolution of 0.01 nm and convolved with a Gaussian slit
307 function of 0.6 nm full width at half maximum (FWHM), which is similar to those of the
308 measurements. For the generation of the spectra a high resolution solar spectrum (Chance and
309 Kurucz, 2010) and the trace gas absorptions of O₃, NO₂, HCHO, and O₄ are considered (see
310 Table A3 in appendix A1). The assumed tropospheric profiles of NO₂ and HCHO are similar
311 to those retrieved from the MAX-DOAS observations during the selected periods. Time series
312 of the tropospheric VCDs of NO₂ and HCHO for the two selected days are shown in Fig. A1
313 in appendix 1.

314 Two sets of synthetic spectra were simulated, one taking into account the temperature
315 dependence of the O₄ cross section and the other not. For the case without considering the
316 temperature dependence the O₄ cross section for 293 K is used. In addition to spectra without
317 noise, also spectra with noise (sigma of the noise is assumed as $7.5 \cdot 10^{-4}$ times the intensity)
318 were simulated. The synthetic spectra are available at the website [http://joseba.mpch-](http://joseba.mpch-mainz.mpg.de/f_doc_zip.htm)
319 [mainz.mpg.de/f_doc_zip.htm](http://joseba.mpch-mainz.mpg.de/f_doc_zip.htm).

321 **3 Strategies used in this studies and comparison results for ‘standard settings’**

322 **3.1 Selection of days**

323 For the comparison of measured and simulated O₄ dAMFs, two mostly clearcloud-free days
324 during the MAD-CAT campaign (18 June and 8 July 2013) were selected. On both days the
325 AOD measured by the AERONET sun photometer at 360 nm is between 0.25 and 0.4 (see
326 Fig. 1). In spite of the similar AOD, very different aerosol properties at the surface are found
327 on the two days: on 18 June much higher concentrations of large aerosol particles (PM_{2.5} and
328 PM₁₀) are found. These differences are also represented by the large differences of the
329 Ångström parameter for long wavelengths (440 – 870 nm) on both days. Also the aerosol
330 height profiles are different: On 8 July rather homogenous profiles with a layer height of
331 about 2 km occur. On 18 June the aerosol profiles reach to higher altitudes, but the highest
332 extinction is found close to the surface. Also the temporal variability of the aerosol properties,
333 especially the near-surface concentrations, is much larger on 18 June.

334 **3.2 Different levels of comparisons**

335 The comparison between the forward model and MAX-DOAS measurements is performed in
336 different depth for different subsets of the measurements:

337 a) A quantitative comparison of O₄ AMFs and O₄ dAMFs is performed for 3° elevation angle
338 at the standard viewing direction (51° with respect to North) for the middle periods of both
339 selected days. During these periods the uncertainties of the measurement and the radiative
340 transfer simulations are smallest because around noon the measured intensities are high and
341 the variation of the SZA is small. During the selected periods, also the variation of the
342 ceilometer profiles is relatively small. These comparisons thus constitute the core of the
343 comparison exercise and all sensitivity studies are performed for these two periods. The
344 elevation angle of 3° is selected because for such a low elevation angle the atmospheric light
345
346
347
348

349 paths and thus the O₄ absorption are rather large. Moreover, as can be seen in Fig. 2, the O₄
350 (d)AMFs for 3° are very similar to those for 1° and 6°, especially on 8 July 2013. Sensitivity
351 studies showed that a wrong elevation calibration ($\pm 0.5^\circ$) led to only small changes (<1%)
352 of the O₄ (d)AMFs. Changes of the field of view between 0.2 and 1.1° led to even smaller
353 differences. ~~This~~ ~~These~~ findings indicates that possible uncertainties of the calibration of the
354 elevation angles of the instruments can be neglected. Here it is interesting to note that on 18
355 June even slightly lower O₄ (d)AMFs are found for the low elevation angles. This is in
356 agreement with the finding of high aerosol extinction in a shallow layer above the surface (see
357 Fig. 1). The azimuth angle of 51° is chosen, because it was the standard viewing direction
358 during the MAD-CAT campaign and measurements for this direction are available from
359 different instruments.

360 b) The quantitative comparison for 3° elevation and azimuth of 51° is also extended to the
361 periods prior and after the middle periods of the selected days. However, to minimise the
362 computational efforts, some sensitivity studies are not carried out for the first and last periods.
363 c) The comparison is extended to more elevation angles (1°, 3°, 6°, 10°, 15°, 30°, 90°) and
364 azimuth angles (51°, 141°, 231°, 321°). For this comparison only the standard settings for the
365 DOAS analysis and the radiative transfer simulations are applied (see Tables 6 and 7). The
366 comparison results for the MPIC MAX-DOAS measurements are shown in appendix A2. The
367 purpose of this comparison is to check whether for other viewing angles similar results are
368 found as for 3° elevation at 51° azimuth direction.

369 **3.3 Quantitative comparison for 3° elevation in standard azimuth direction**

370 Fig. 3 presents a comparison of the measured and simulated O₄ (d)AMFs for 3° elevation and
371 51° azimuth on both days. For the spectral analysis and the radiative transfer simulations the
372 respective ‘standard settings’ (see Tables 6 and 7) were used. On 8 July the simulated O₄
373 (d)AMFs systematically underestimate the measured O₄ (d)AMFs by up to 40%. Similar
374 results are also obtained for other elevation and azimuth angles (see appendix ~~A1~~A2), the
375 differences becoming smaller towards higher elevation angles. In contrast, no systematic
376 underestimation is observed for most of 18 June. For some periods of that day the simulated
377 O₄ (d)AMFs are even larger than the measured O₄ (d)AMFs. However, here it should be
378 noted that the aerosol extinction profile of the ‘standard settings’ (using linear extrapolation
379 below 180 m where no ceilometer data are available) probably underestimates the aerosol
380 extinction close to the surface. If instead a modified aerosol profile with strongly increased
381 aerosol extinction below 180 m and the maximum AOD during that period is used (see Fig.
382 A31 in appendix A5) the corresponding (d)AMFs fall below the measured O₄ (d)AMFs
383 (green curves in Fig. A4 in appendix A2). More details on the extraction of the aerosol
384 extinction profiles are given in section 4.2.2 and appendix A5).

385 The average ratio of simulated to measured (d)AMFs (for the standard settings) during the
386 middle periods on both days are given in Table 8. For 18 June they are close to unity, for 8
387 July they are much lower (0.83 for the AMF, and 0.69 for the dAMF).

390 **4 Estimation of the uncertainties of the different processing steps**

391 There are 3 major processing steps, for which the uncertainties are quantified in this section:

- 392 a) The determination of the O₄ height profiles and corresponding O₄ vertical column densities.
- 393 b) The simulation of O₄ (d)AMFs by the forward model
- 394 c) The analysis of O₄ (d)AMFs from the MAX-DOAS measurements.

395 **4.1 Determination of the vertical O₄ profile and the O₄ VCD**

400
401
402
403
404
405
406
407
408
409
410
411
412
413
414
415
416
417
418
419
420
421
422
423
424
425
426
427
428
429
430
431
432
433
434
435
436
437
438
439
440
441
442
443
444
445
446
447
448
449

The O₄ VCD is required for conversion of measured (d)SCDs into (d)AMFs (eq. 1). O₄ profiles are also needed for the calculation of O₄ (d)AMFs. The accuracy of the calculated O₄ height profile and the O₄ VCD depends in particular on two aspects:

- a) is profile information on temperature, pressure and (relative) humidity available?
- b) what is the accuracy of these data sets?

Additional uncertainties are related to the details of the calculation of the O₄ concentration and O₄ VCDs from these profiles. Both error sources are investigated in the following sub sections.

4.1.1 Extraction of vertical profiles of temperature and pressure

The procedure of extracting temperature and pressure profiles depends on the availability of measured profile data or surface measurements. If profile data are available (e.g. from sondes or models) they could be directly used. If only surface measurements are available, vertical profiles of temperature and pressure could be calculated making assumptions on the lapse rate (here we assume a value of -0.65 K / 100 m). If no measurements or model data are available, profiles from the US standard atmosphere might be used (United States Committee on Extension to the Standard Atmosphere, 1976). In appendix A3 the different procedures are described in detail for the two days of the MAD-CAT campaign. For these days the optimum choice was to combine the model data and the surface measurements. In that way, the diurnal variation in the boundary layer could be considered.

~~For the two selected days during the MADCAT campaign two data sets of temperature and pressure are available: surface measurements close to the measurement site and vertical profiles from ECMWF ERA-Interim re-analysis data (see Table 5). Both data sets are used to derive the O₄ concentration profiles for the three selected periods on both days. The general procedure is that first the temperature profiles are determined. In a second step, the pressure profiles are derived from the temperature profiles and the measured surface pressure. For the temperature profile extraction, three height layers are treated differently:~~

~~-below 1 km~~

~~Between the surface (~150 m above sea level) and 1 km, the temperature is linearly interpolated between the average of the in situ measurements of the respective period and the ECMWF data at 1 km (see next paragraph). This procedure is used to account for the diurnal variation of the temperature close to the surface. Here it is important to note that for this surface near layer the highest accuracy is required, because a) the maximum O₄ concentration is located near the surface, and b) the MAX-DOAS measurements are most sensitive close to the surface.~~

~~-1 km to 20 km~~

~~In this altitude range, the diurnal variation of the temperature becomes very small. Thus the average of the four ECMWF profiles of each day is used (for simplicity, a 6th-order polynomial is fitted to the ECMWF data).~~

~~-Above 20 km~~

~~In this altitude range the accuracy of the temperature profile is not critical and thus the ECMWF temperature profile for 00:00 UTC of the respective day is used for simplicity.~~

~~The temperature profiles for 8 July 2013 extracted in this way are shown in Fig. 4 (left). Close to the surface the temperature variation during the day is about 10 K.~~

~~In the next step, the pressure profiles are determined from the surface pressure (obtained from the in situ measurements) and the extracted temperature profiles according to the ideal gas law. In principle the effect of atmospheric humidity could also be taken into account, but the effect is very small for surface near layers and is thus ignored here. The derived pressure~~

450 profiles for 8 July 2013 are shown in Fig. 4 (right). Excellent agreement with the
451 corresponding ECMWF pressure profiles is found.
452 Here it should be noted that in principle also the ECMWF pressure profiles could be used.
453 However, we chose to determine the pressure profiles from the surface pressure and the
454 extracted temperature profiles, because this procedure can also be applied if no ECMWF data
455 (or other information on temperature and pressure profiles) is available.
456 If no profile data (e.g. from ECMWF) are available, temperature and pressure profiles can
457 also be extrapolated from surface measurements e.g. by assuming a constant lapse rate of
458 $-0.65 \text{ K} / 100 \text{ m}$ for the altitude range between the surface and 12 km, and a constant
459 temperature above 12 km (as stated above, uncertainties at this altitude range have only a
460 negligible effect on the O_4 VCD). If no measurements or model data are available at all, a
461 fixed temperature and pressure profile can be used, e.g. the US standard atmosphere (United
462 States Committee on Extension to the Standard Atmosphere, 1976).
463 A comparison of the ~~different~~ temperature profiles extracted by the different methods for two
464 selected periods on both days is shown in Fig. 5. For 8 July (right), rather good agreement is
465 found, but for 18 June (left) the agreement is worse (differences up to 20 K). Of course, the
466 differences between the true and the US standard atmosphere profiles can become even larger,
467 depending on location and season. So the use of a fixed temperature and pressure profile
468 should always be the last choice. In contrast, the simple extrapolation from surface values can
469 be very useful if no profile data are available, because the uncertainties of this method are
470 usually smallest at low altitudes, where the bulk of O_4 is located.

472 4.1.2 Calculation of O_4 concentration profiles and O_4 VCDs

473
474 From the temperature and pressure profiles the oxygen (O_2) concentration is calculated. Here
475 also the effect of the atmospheric humidity profiles should be taken into account (see
476 below appendix A3), because it can have a considerable effect on the surface-near layers (at
477 least for temperatures of about $> 20^\circ\text{C}$). Finally, the square of the oxygen concentration is
478 calculated and used as proxy for the O_4 concentration (see Greenblatt et al., 1990). The
479 uncertainties of the derived O_4 concentration (and the corresponding O_4 VCD) caused by the
480 uncertainty of the input profiles is estimated by varying the input parameters (for details see
481 appendix A3). ~~The following uncertainties are derived:~~
482 ~~The variation of the temperature (whole profile) by about 2K leads to variations of the O_4~~
483 ~~concentration (or O_4 VCD) by about 0.8%.~~
484 ~~The variation of the surface pressure by about 3 hPa leads to variations of the O_4~~
485 ~~concentration (or O_4 VCD) by about 0.7%.~~
486 ~~The effect of uncertainties of the relative humidity depends strongly on temperature: For~~
487 ~~surface temperatures of 0°C , 10°C , 20°C , 30°C , and 35°C a variation of the relative humidity~~
488 ~~of 30% leads to variations of the O_4 concentration (or O_4 VCDs) of about 0.15%, 0.3%, 0.6%,~~
489 ~~1.2%, and 1.6%, respectively. If the effect of atmospheric humidity is completely ignored (dry~~
490 ~~air is assumed), the resulting O_4 concentrations (or O_4 VCDs) are systematically~~
491 ~~overestimated by about 0.3%, 0.7%, 1.3%, 2.5%, and 4% for surface temperatures of 0°C ,~~
492 ~~10°C , 20°C , 30°C , and 35°C , respectively (assuming a relative humidity of 70%). In this~~
493 ~~study we used the relative humidity measured by the in-situ sensors. We took these values not~~
494 ~~only for the surface layers, but also for the whole troposphere. Here it should be noted that the~~
495 ~~related uncertainties of the absolute humidity decrease quickly with altitude because the~~
496 ~~absolute humidity itself decrease quickly with altitude. Since both selected days were warm or~~
497 ~~even hot summer days, we estimate the uncertainty of the O_4 concentration and O_4 VCDs due~~
498 ~~to uncertainties of the relative humidity to 1% and 0.4% on 18 June and 8 July, respectively.~~
499 For both selected days during the MAD-CAT campaign Assuming that the uncertainties of
500 the three input parameters are independent, the total uncertainty related to the is se factors is

501 estimated to be about 1.5% assuming that the uncertainties of the individual input
502 parameterinput parameters are independent.

503 Further uncertainties arise from the procedure of the vertical integration of the O₄
504 concentration profiles. We tested the effect of using different vertical grids and altitude
505 ranges. It is found that the vertical grid should not be coarser than 100 m (for which a
506 deviation of the O₄ VCD of 0.3% compared to a much finer grid is found). If e.g. a vertical
507 grid with 500 m layers is used, the deviation increases to about 1.3%. The integration should
508 be performed over an altitude range up to 30 km. If lower maximum altitudes are used, the O₄
509 VCD will be substantially underestimated: deviations of 0.1 %, 0.5 %, and 11% are found if
510 the integration is performed only up to 25 km, 20 km, and 10 km, respectively. Here it should
511 be noted that the exact consideration of the altitude of the measurement site is also very
512 important: A deviation of 50 m already leads to a change of the O₄ VCD by 1%. For the
513 MAD-CAT measurements the altitude of the instruments is 150m ±20m.

514 Finally, the effects of individual extraction and integration procedures are investigated by
515 comparing the results from different groups (see Fig. 6, and Fig. A5 in appendix A3). Except
516 for some extreme cases, the extracted temperatures typically differ by less than 3 K below 10
517 km. However, the deviations are typically larger for the profiles extrapolated from the surface
518 values and in particular for the US standard atmosphere (up to > 10 K below 10 km). Also the
519 variations of the extracted pressure profiles are in general rather small (< 1% below 10 km,
520 except one obvious outlier). Also here the deviations of the profiles extrapolated from the
521 surface values and especially the US standard atmosphere are much larger (up to > 5 % below
522 10 km). The resulting deviations of the O₄ concentration from the different extractions are
523 typically <3% below 10 km (and up to > 20 % below-above 10 km for the US standard
524 atmosphere).

525 In Fig. 7 the O₄ VCDs calculated for the O₄ profiles extracted from the different groups and
526 for the profiles extrapolated from the surface values and the US standard atmosphere are
527 shown. The VCDs for the profiles extracted by the different groups agree within 2.5%. The
528 deviations for the profiles extrapolated from the surface values are only slightly larger
529 (typically within 3%), but show a large variability throughout the day, which is caused by the
530 systematic increase of the surface temperature during the day (with temperature inversions in
531 the morning on the two selected days). The deviations of the US standard atmosphere are up
532 to 5% (but can of course be larger for other seasons and locations, see also Ortega et al.
533 (2016).

534 Ultimately, the accuracy with which O₄ concentrations can be calculated is limited by the
535 assumption that O₄ (O₂-O₂) is pure collision induced absorption. If the oxygen concentration
536 profile is well known, the uncertainty due to bound O₄ is smaller 0.14% in Earth's atmosphere
537 (Thalman and Volkamer, 2013).

538 Together with the uncertainties related to the input data sets, the total uncertainty of the O₄
539 VCDs determined for both selected days is estimated as 3%.

540

541 **4.2 Uncertainties of the O₄ (d)AMFs derived from radiative transfer simulations**

542

543 The most important errors of the simulated O₄ (d)AMFs are related to the uncertainties of the
544 input parameters used for the simulations, in particular the aerosol properties. Further
545 uncertainties are caused by imperfections of the radiative transfer models. These error sources
546 are discussed and quantified in the following sub sections.

547

548 **4.2.1 Uncertainties of the O₄ (d)AMFs caused by uncertainties of the input parameters**

549

550 In this section the effect of the uncertainties of various input parameters on the O₄ (d)AMFs is
551 investigated. The general procedure is that the input parameters are varied individually and

552 the corresponding changes of the O₄ (d)AMFs compared to the standard settings are
553 quantified.

554 First, the effect of the O₄ profile shape is investigated. In contrast to the effect of the
555 (absolute) profile shape on the O₄ VCD (section 4.1), here the effect of the relative profile
556 shape on the O₄ AMF is investigated. The O₄ (d)AMFs simulated for the O₄ profiles extracted
557 by the different groups (and for those derived from the US standard atmosphere and the
558 profiles extrapolated from the surface values, see section 4.1) are compared to those for the
559 MPIC O₄ profiles (using the standard settings). The corresponding ratios are shown in Fig. A6
560 and Table A4 in appendix A4. For the O₄ profiles extracted by the different groups, and for
561 O₄ profiles extrapolated from the surface values, small variations are found (typically < 2%).
562 For the ~~O₄-US~~ standard atmosphere larger deviations (up to 7%) are derived.

563 Next the effect of the aerosol extinction profile is investigated. In this study, aerosol
564 extinction profiles are derived from the combined ceilometer and sun photometer
565 measurements (see Table 5). In short, the ceilometer measurements of the attenuated
566 backscatter are scaled by the simultaneously measured aerosol optical depth (AOD) from the
567 sun photometer to obtain the aerosol extinction profile. Also the self-attenuation of the aerosol
568 is taken into account. The different steps are illustrated in Fig. 8 and described in detail in
569 appendix A5. In the extraction procedure, several assumptions have to be made: First, the
570 ceilometer profiles have to be extrapolated for altitudes below 180 m, for which the
571 ceilometer is not sensitive. Furthermore, they have to be averaged over several hours and are
572 in addition vertically smoothed (above 2 km) to minimise the rather large scatter. Finally,
573 above 5 to 6 km (depending on the ceilometer profiles) the extinction is set to zero because of
574 the further increasing scatter and the usually small extinctions. Another assumption is that the
575 LIDAR ratio is independent of altitude, which is typically not strictly fulfilled (the LIDAR
576 ratio describes the ratio between the extinction and backscatter probabilities of the molecules
577 and aerosol particles).

578 ~~Some of t~~These uncertainties are quantified by sensitivity studies, in particular the effect of
579 the extrapolation below 180 m and the altitude above which the aerosol extinction is set to
580 zero. Other uncertainties, like the effect of the assumption of a constant LIDAR ratio are more
581 difficult to quantify without further information (see below). ~~While a constant LIDAR ratio is~~
582 ~~probably a good assumption for 8 July, for 18 June the surface measurements indicate that the~~
583 ~~aerosol properties strongly change with time. Thus the LIDAR ratio might also vary stronger~~
584 ~~with altitude on that day.~~ The effect of temporal averaging and smoothing is probably
585 negligible for 8 July, because similar height profiles are found for all three periods of that day,
586 but on 18 June the effect might be more important.

587 Fig. 9 shows a comparison of the aerosol extinction profiles extracted by the different groups
588 for the three periods on both days. Especially on 8 July systematic differences are found.
589 They are caused by the different altitudes, above which the aerosol extinction is set to zero. In
590 combination with the scaling of the profiles with the AOD obtained from the sun photometer,
591 this also influences the extinction values close to the surface. Deviations up to 18% are found
592 for the first period of 8 July. These deviations also have an effect on the corresponding O₄
593 (d)AMFs, where higher values are obtained for the profiles (INTA and IUPB 300m) which
594 were extracted for a larger altitude range (Fig. A7 and Table A5 in the appendix A4). Here it
595 is interesting to note that these differences are not related to the direct effect of the aerosol
596 extinction at high altitude, but to the corresponding (via the scaling with the AOD) decrease
597 of the aerosol extinction close to the surface. Larger deviations (up to 4%) are found for 8
598 July, while the deviations on 18 June are within 3%.

599 In Fig. A8 and Table A6 in appendix A4, the effect of the different extrapolations of the
600 aerosol extinction profile below 180 m on the O₄ (d)AMFs is quantified. Similar deviations
601 (up to 5 %) are found for both days.

602 Finally, we investigated the effect of changing aerosol optical properties with altitude
603 (changing LIDAR ratio). Such effects are in particular important if the wavelength of the
604 ceilometer measurements (1020 nm) differs largely from that of the MAX-DOAS observations
605 (360 nm). Based on the partitioning in fine and coarse mode aerosols derived from the sun
606 photometer observations, as well as the corresponding phase functions and optical depths, the
607 sensitivity of the ceilometer to fine mode aerosols can be estimated (for details see appendix
608 A5). While for 18 June the contribution of the fine mode to the ceilometer signal is about 32%
609 on 8 July it is much larger (about 82 %). Thus it can be concluded that the aerosol extinction
610 profile derived from the ceilometer is largely representative for the fine mode aerosols on that
611 day. Nevertheless, the remaining uncertainties of the aerosol extinction profile at 360 nm
612 together with the assumption that the coarse aerosols are probably located close to the surface
613 led to a repartitioning of parts of the aerosol extinction profile (extracted assuming a constant
614 LIDAR ratio). This repartitioning led to a decrease of the aerosol extinction close to the
615 surface which is balanced by an increase at higher altitudes (see Fig. A34). The O₄ dAMFs
616 calculated for the modified profile are by about 15 % larger than those for the standard
617 settings (for details see appendix A5).

618 The effect of elevated aerosol layers (see Ortega et al., 2016) was further investigated by
619 systematic sensitivity studies (appendix A6). On both selected days enhanced aerosol
620 extinction was found at elevated layers (Fig. 9). Compared to those reported by Ortega et al.
621 (2016) the profiles extracted in this study reach even up to higher altitudes. For the
622 investigation of the effect of changes of the aerosol extinction at different altitudes, the
623 aerosol extinction profile on 8 July was subdivided into 3 layers (0-1.7 km; 1.7 – 4.9 km; 4.9
624 – 7 km), and the extinction in the individual layers was increased by +20% or + 40 %. It was
625 found that even a strong increase of the aerosol extinction at high altitudes by 40% leads only
626 to an increase of the O₄ dAMFs by 7 %. Here it should be noted that on 8 July no indications
627 for such a strong underestimation of the aerosol extinction at high altitudes are found.

628
629 Also the effect of horizontal gradients should be briefly discussed. For the selected periods of
630 both days, the wind direction and wind speed were rather constant. On 18 June the wind
631 direction was between 80° and 150° with respect to North, and the wind speed was about 2
632 m/s. On 8 July the wind direction was between 70° and 90°(the wind came from almost the
633 same direction at which the instruments were looking), and the wind speed was about 3 m/s.
634 During the 4 hours of the selected period on 8 July, the air masses moved over a distance of
635 about 40 km. During the 3 hours of the selected period on 18 June, the air masses moved over
636 a distance of about 20 km. These distances are larger than the distances for which the MAX-
637 DOAS observations are sensitive (about 5 – 15 km). Since also the AOD and the aerosol
638 extinction profiles were rather constant during both selected periods, we conclude that for the
639 measurements considered here horizontal gradients can be neglected. Here it should also be
640 noted that the discrepancies between measurements and simulations were simultaneously
641 observed at all 4 azimuth directions.

642
643 In Fig. A9 and Table A7 in appendix A4, the effect of different single scattering albedos
644 (between 0.9 and 1) on the O₄ (d)AMFs is quantified. The effect on the O₄ (d)AMFs is up 4 %
645 on 18 June and up to 2 % on 8 July 2013.

646 The impact of the aerosol phase function is investigated in two ways: First, simulation results
647 are compared for Henyey Greenstein phase functions with different asymmetry parameters.
648 The corresponding results are shown in Fig. A10 and Table A8 in appendix A4. The
649 differences of the O₄ (d)AMFs for the different aerosol phase functions are rather strong: up
650 to 3% for the O₄ AMFs and up to 8% for the O₄ dAMFs (larger uncertainties for the dAMFs
651 are found because of the strong influence of the phase function on the 90° observations). Here
652 it should be noted that the actual deviations from the true phase function might be even larger.

653 In order to better estimate these uncertainties, also simulations for phase functions derived
654 from the sun photometer measurements based on Mie theory (in the following referred to as
655 Mie phase functions) were performed. A comparison of these Mie phase functions with the
656 Henyey Greenstein phase functions is shown in Fig. 10. Large differences, especially in
657 forward direction are obvious. The O_4 (d)AMFs for the Mie phase functions are compared to
658 the standard simulations (using the HG phase function for an asymmetry parameter of 0.68) in
659 Fig. A11 and Table A9 in Appendix A4. Again rather large deviations are found, which are
660 larger on 18 June (up to 9 %) than on 8 July (up to 5%).

661 In Fig. A12 and Table A10 in Appendix A4, the effect of different surface albedos on the O_4
662 (d)AMFs is quantified. For the considered variations (0.03 to 0.1) the changes of the O_4
663 (d)AMFs are within 2 %.

664

665 **4.2.2 Uncertainties of the O_4 (d)AMFs caused by imperfections of the radiative transfer** 666 **models**

667

668 The radiative transfer models used in this study are well established and showed very good
669 agreement in several intercomparison studies (e.g. Hendrick et al., 2006; Wagner et al., 2007;
670 Lorente et al., 2017). Nevertheless, they are based on different methods and use different
671 approximations (e.g. with respect to the Earth's sphericity). Thus we compared the simulated
672 O_4 (d)AMFs for both days in order to estimate the uncertainties associated to these
673 differences. In Fig. A13 and Table A11 (appendix A4), the comparison results are shown.
674 They agree within a few percent with slightly larger differences for 18 June (up to 6 %) than
675 for 8 July (up to 3 %).

676 So far, all radiative transfer simulations were carried out without considering polarisation.
677 Thus in Fig. A14 and Table A12 in appendix A4, the results with and without considering
678 polarisation are compared. The corresponding differences are very small (<1%).

679

680 **4.2.3 Summary of uncertainties of the O_4 AMF from radiative transfer simulations**

681

682 Table 9 presents an overview on the different sources of uncertainties of the simulated O_4
683 (d)AMFs derived from the comparison of the results from different groups and the sensitivity
684 studies. The uncertainties are expressed as relative deviations from the results for the standard
685 settings (see Table 6) derived by MPIC using MCARTIM.

686 In general, larger uncertainties are found for the O_4 dAMFs compared to the O_4 AMFs. This is
687 expected because the uncertainties of the O_4 dAMFs contain the uncertainties of two
688 simulations (at 90° elevation and at low elevation). Another general finding is that the
689 uncertainties on 18 June are larger than on 8 July. This finding is mainly related to the larger
690 uncertainties due to the aerosol phase function, which has an especially strong forward peak
691 on 18 June. Also the error contributions from the O_4 profile extraction, the choice of the
692 radiative transfer model and the extrapolation of the aerosol extinction below 180 m are larger
693 on 18 June than on 8 July. These higher uncertainties are probably mainly related to the high
694 aerosol extinction close to the surface on 18 June (see section 5.1, and appendices A2 and
695 A5).

696 For the total uncertainties two values are given in Table 9: The 'average deviation' is the sum
697 of all systematic deviations of the individual uncertainties (the corresponding mean of the
698 maximum and minimum values). The second quantity (the 'range of uncertainties') is
699 calculated from half the individual uncertainty ranges by assuming that they are independent.

700 Finally, it should be noted that for some error sources (e.g. the effects of the surface albedo or
701 the single scattering albedo) the given numbers probably overestimate the true uncertainties,
702 while for others, e.g. the uncertainties related to the aerosol extinction profiles or the phase
703 functions they possibly underestimate the true uncertainties (although reasonable assumptions

704 were made). The two latter error sources are especially large for 18 June. The differences
705 between both days are discussed in more detail in section 5.

706

707 **4.3 Uncertainties of the spectral analysis**

708

709 The uncertainties of the spectral analysis are caused by different effects:

710 -the specific settings of the spectral analysis like the fit window or the degree of the
711 polynomial. Of particular interest is the effect of choosing different O_4 cross sections as well
712 as its temperature dependence.

713 -the properties (and imperfections) of the MAX-DOAS instruments

714 -the effect of different analysis software and implementations

715 -the effect of the wavelength dependence of the AMF across the fit window.

716 These error sources are discussed and quantified in the following sub sections.

717

718

719 **4.3.1 Comparison of O_4 (d)AMFs derived from the synthetic spectra with O_4 (d)AMFs 720 directly obtained from the radiative transfer simulations**

721

722 Synthetic spectra for both selected days were simulated using the radiative transfer model
723 SCIATRAN (for details see section 2.4 and Table A3 in appendix A1). While spectra for the
724 whole day are simulated (for the viewing geometry see Table A2 in appendix A1) it should be
725 noted that the aerosol properties during the middle periods are used also for the whole day (to
726 minimise the computational efforts). The spectra are analysed using the standard settings and
727 the derived O_4 (d)SCDs are converted to O_4 (d)AMFs using eq. 1. In addition to the spectra,
728 also O_4 (d)AMFs at 360 nm are simulated directly by the RT models using exactly the same
729 settings. These O_4 (d)AMFs are used to test whether the spectral retrieval results are indeed
730 representative for the simulated O_4 (d)AMFs at 360 nm.

731 Spectra are simulated with and without considering the temperature dependence of the O_4
732 cross section. Also one version of synthetic spectra with added random noise is processed.

733 First, the synthetic spectra are analysed using the standard settings (see Table 7). Examples of
734 the O_4 fits for synthetic (and measured) spectra are shown in Fig. 11. Here it is interesting to
735 note that the ratios of the results for the measured spectrum and the simulated spectra are
736 between 0.68 and 0.74, similar to ratio for the dAMFs on 8 July shown in Table 8.

737 In Fig. 12 the ratios of the O_4 (d)AMFs derived from the synthetic spectra versus those
738 directly obtained from the radiative transfer simulations at 360 nm are shown. In the upper
739 part (a) the results for synthetic spectra considering the temperature dependence of the O_4
740 cross section are presented (without noise). Systematically enhanced ratios are found in the
741 morning and evening, while for most of the day the ratios are close to unity. The higher
742 values in the morning and evening are probably partly caused by the increased light paths
743 through higher atmospheric layers (with lower temperatures) when the solar zenith angle is
744 high. Interestingly, if the temperature dependence of the O_4 cross section is not taken into
745 account (Fig. 12 b), still slightly enhanced ratios during the morning and evening are found,
746 which can not be explained anymore by the temperature dependence of the O_4 cross section.
747 Thus we speculate whether part of the enhanced values at high SZAs are probable caused by
748 the wavelength dependence of the O_4 AMFs. Nevertheless, for most of the day the ratio is
749 very close to unity indicating that for $SZA < 75^\circ$ the O_4 (d)AMFs obtained from the spectral
750 analysis are almost identical to the O_4 (d)AMFs directly obtained from the radiative transfer
751 simulations (at 360 nm).

752 In Fig. 12 c results for spectra with added random noise (without consideration of the
753 temperature dependence of the O_4 cross section) are shown. On average similar results as for
754 the spectra without noise (Fig. 12 b) are found but the results now show a large scatter. From

755 these results and also the spectral analyses (Fig. 11) we conclude that the noise added to the
756 synthetic spectra overestimates that of the real measurements.
757 In Table A13 in appendix A4 the average ratios for the middle periods on both selected days
758 are shown. They deviate from unity by up to 2% indicating that the wavelength dependence of
759 the O_4 (d)AMF is negligible for the considered cases for $SZA < 75^\circ$.

760

761 **4.3.2 Sensitivity studies for different fit parameters**

762

763 In this section the effect of the choice of several fit parameters on the derived O_4 (d)AMFs is
764 investigated using both measured and synthetic spectra. Only one fit parameter is varied for
765 each individual test, and the results are compared to those for the standard fit parameters (see
766 Table 7).

767 First the fit window is varied. Besides the standard fit window (352 to 387 nm), which
768 contains two O_4 bands, also two fit windows towards shorter wavelengths are tested: 335 –
769 374 nm (including two O_4 bands) and 345 – 374 nm (including one O_4 band at 360 nm). The
770 ratios of the derived O_4 (d)AMFs versus those for the standard analysis are shown in Fig. A15
771 and Table A14 in appendix A2. On 18 June rather large deviations of the O_4 (d)AMFs are
772 found for both measured (-12%) and synthetic spectra (-5%) for the spectral range 335 to 374
773 nm. On 8 July the corresponding differences are smaller (-6% and -2% for measured and
774 synthetic spectra, respectively). For the spectral range 345 – 374 nm, smaller differences of
775 only up to 1% are found for both days. The reason for the larger deviations on 18 June for the
776 spectral range 335 – 374 nm is not clear. One possible reason could be the differences of the
777 Ångström parameters (see Fig. 1) and phase functions (see Fig 10).

778 In Fig. A16 and Table A15 the results for different degrees of the polynomial used in the
779 spectral analysis are shown. For the measured spectra systematically higher O_4 (d)AMFs (up
780 to 6%) than for the standard analysis are found when using lower polynomial degrees. For the
781 synthetic spectra the effect is smaller (<3%).

782 In Fig. A17 and Table A16 the results for different intensity offsets are shown. Again, for the
783 measured spectra systematically higher O_4 (d)AMFs (up to 16%) than for the standard
784 analysis are found when reducing the order of the intensity offset, while for the synthetic
785 spectra the effect is smaller (<3%). Higher order intensity offsets might compensate for
786 wavelength dependent offsets (e.g. spectral straylight), which can be important for real
787 measurements, while the synthetic spectra do not contain such contributions.

788 In Fig. A18 and Table A17 the results for spectral analyses with only one Ring spectrum are
789 shown. In contrast to the standard analysis, which includes two Ring spectra (one for clear
790 and one for cloudy sky, see Wagner et al., 2009), only the Ring spectrum for clear sky is used.
791 For both selected days, only small deviations (within 2%) compared to the standard analysis
792 are found.

793

794 **4.3.3 Sensitivity studies using different trace gas absorption cross sections**

795

796 In this section the impact of different trace gas absorption cross sections on the derived O_4
797 (d)AMFs is investigated.

798 In Fig. A19 and Table A18 the results for using two NO_2 cross sections (294 and 220 K)
799 compared to the standard analysis (using only a NO_2 cross section for 294 K) are shown. The
800 results are almost the same as for the standard analysis.

801 In Fig. A20 and Table A19 the results for using an additional wavelength-dependent NO_2
802 cross section compared to the standard analysis (using only one NO_2 cross section) are shown.
803 The second NO_2 cross section is calculated by multiplying the original cross section with
804 wavelength (Pukite et al., 2010). Again, only small deviations of the results from the standard
805 analysis (1% for the measured spectra, and 2% for the synthetic spectra) are found.

806 In Fig. A21 and Table A20 results for using and additional wavelength-dependent O₄ cross
807 sections compared to the standard analysis (using only one O₄ cross section) are shown. The
808 second O₄ cross section is calculated like for NO₂, but also an orthogonalisation with respect
809 to the original O₄ cross section (at 360 nm) is performed. The derived O₄ (d)AMFs are almost
810 identical to those from the standard analysis (within 1%).

811 For the spectral retrieval of HONO in a similar spectral range, a significant impact of water
812 vapour absorption around 363 nm was found in Wang et al. (2017c) and Lampel et al. (2017).
813 In Fig. A22 and Table A21 the O₄ results for including a H₂O cross section (Polyansky et al.,
814 2018) compared to the standard analysis (using no H₂O cross section) are shown. The results
815 are almost identical to those from the standard analysis (within 1%).

816 In Fig. A23 and Table A22 the results for including a HCHO cross section (Polyansky et al.,
817 2018) compared to the standard analysis (using no HCHO cross section) are shown.
818 Especially for 18 June a large systematic effect is found: the O₄ dAMFs are by 4 % or 6 %
819 smaller than for the standard analysis for measured and synthetic spectra, respectively. On 8
820 July the underestimation is smaller (2% and 3% for measured and synthetic spectra,
821 respectively).

822

823 **4.3.4 Effect of using different O₄ cross sections**

824

825 In Fig. A24 and Table A23 the results for different O₄ cross sections are compared to the
826 standard analysis (using the Thalman O₄ cross section). The results for both days are almost
827 identical. For the real measurements, the derived O₄ dAMFs using the Hermans and
828 Greenblatt cross sections are by 3% smaller or 8 % larger than those for the standard analysis,
829 respectively. However, if the Greenblatt O₄ cross section is allowed to shift during the
830 spectral analysis, the overestimation can be largely reduced to only +3 %. This confirms
831 findings from earlier studies (e.g. Pinardi et al., 2013) that the wavelength calibration of the
832 original data sets is not very accurate.

833 For the synthetic spectra slightly different results than for the real measurements are found for
834 the Hermans O₄ cross section. The reason for these differences is not clear. However, here it
835 should be noted that the temperature dependent O₄ absorption in the synthetic spectra does
836 probably not exactly represent the true atmospheric O₄ absorption.

837

838 **4.3.5 Effect of the temperature dependence of the O₄ cross section**

839

840 The new set of O₄ cross sections provided by Thalman and Volkamer (2013) allows to
841 investigate the temperature dependence of the atmospheric O₄ absorptions in detail. They
842 provide O₄ cross sections measured at five temperatures (203, 233, 253, 273, 293 K) covering
843 the range of temperatures relevant for atmospheric applications. Using these cross sections,
844 the effect of the temperature dependence of the O₄ absorptions is investigated in two ways:

845 a) In a first test, synthetic spectra are simulated for different surface temperatures assuming a
846 fixed lapse rate. These spectra are then analysed using the O₄ cross section for 293K (which is
847 usually used for the spectral analysis of O₄). From this study the magnitude of the effect of the
848 temperature dependence of the O₄ cross section on MAX-DOAS measurements can be
849 quantified.

850 b) In a second test, measured and synthetic spectra for both selected days are analysed with
851 O₄ cross sections for different temperatures. From this study it can be seen to which degree
852 the temperature dependence of the O₄ cross section can be already corrected during the
853 spectral analysis (if two O₄ cross sections are used simultaneously).

854 For the first study, MAX-DOAS spectra are simulated in a simplified way:

855 -Atmospheric temperature profiles are constructed for surface temperatures between 220 K
856 and 310 K in steps of 10 K assuming a fixed lapse rate of $-0.656 \text{ K} / 100 \text{ m}$.

857 -For each altitude layer (vertical extension: 20 m below 500m, 100 m between 500 m and 2
858 km, 200 m between 2 km and 12 km, 1 km above) the O₄ concentrations (calculated from the
859 US standard atmosphere) are multiplied with the corresponding differential box-AMFs
860 calculated for typical atmospheric conditions and viewing geometries (see Fig. A25 in
861 appendix A4).

862 -High resolution absorption spectra are calculated by applying the Beer-Lambert-law for each
863 height layer using the O₄ cross section of the respective temperature (interpolated between the
864 two adjacent temperatures of the Thalman and Volkamer data set).

865 -The derived high resolution spectra are convolved with the instrument slit function (FWHM
866 of 0.6 nm).

867 -The logarithm of the ratio of the spectra for the low elevation and zenith is calculated and
868 analysed using the O₄ cross section for 293 K.

869 -The derived O₄ dAMFs are divided by the corresponding dAMFs directly obtained from the
870 radiative transfer simulations.

871 These calculated ratios as function of the surface temperature are shown in Fig. 13. A strong
872 and systematic dependence on the surface temperature is found (15 % for a change of the
873 surface temperature between 240 and 310 K). However, except for measurements at polar
874 regions, the deviations are usually small. Since for both selected days the temperatures were
875 rather high (indicated by the two coloured horizontal bars in the figure), the effect of the
876 temperature dependence of the O₄ absorption for the middle periods of both days is very small
877 (-1 to -2% for 18 June, and 0 to +1% on 8 July). It should be noted that the results shown in
878 Fig. 13 are obtained for generalised settings of the radiative transfer simulations. Thus it is
879 recommended that future studies should investigate the effect of the temperature dependence
880 in more detail and using the exact viewing geometry for individual observations. However,
881 since the temperatures on both selected days were rather high, for this study the
882 simplifications of the radiative transfer simulations have no strong influence on the derived
883 results.

884 In the second test the measured and synthetic spectra are analysed using O₄ cross sections for
885 different temperatures. The corresponding results are shown in Fig. A26 and Table A24.

886 If only the O₄ cross section at low temperature (203 K) is used, the derived O₄ AMFs and
887 dAMFs are by about 16% and 30% smaller than for the standard analysis (using the O₄ cross
888 section for 293 K). These results are consistently obtained for the measured and synthetic
889 spectra. If, however, two O₄ cross sections (for 203 and 293 K) are simultaneously included in
890 the analysis, different results are obtained for the measured and synthetic spectra: for the
891 measured spectra the derived O₄ (d)AMFs agree within 4% with those from the standard
892 analysis. In contrast, for the synthetic spectra, the derived O₄ (d)AMFs are systematically
893 smaller (by about 6 to 18 %). This finding was not expected, because exactly the same cross
894 sections were used for both the simulation and the analysis of the synthetic spectra. Detailed
895 investigations (see appendix A4) led to the conclusion that there is a slight inconsistency in
896 the temperature dependence of the O₄ cross sections from Thalman et al. (2013): The ratio of
897 the peak values of the cross section at 360 and 380 nm changes in a non-continuous way
898 between 253 and 223 K (see Fig. A27 in appendix A4). The reason for this inconsistency is
899 currently not known. If these two O₄ bands are included in the spectral analysis (as for the
900 standard settings), the convergence of the spectral analysis strongly depends on the ability to
901 fit both O₄ bands well. Thus the fit results for both O₄ cross sections are mainly determined by
902 the relative strengths of both O₄ bands (see Fig. A27 in appendix A4). If instead a smaller
903 wavelength ranges is used containing only one absorption band (345 – 374 nm), the derived
904 O₄ (d)AMFs are in rather good agreement with the results of the analysis (using only the O₄
905 cross section for 293 K), see Table A25 in appendix A4. In that case, the convergence of the
906 fit mainly depends on the temperature dependence of the line width. It should be noted that
907 the non-continuous temperature dependence of the O₄ absorption cross section only affects

908 the analysis of the synthetic spectra, because for the simulation of the spectra all O₄ cross
909 sections for temperatures between 223 and 293 K were used. For the measured spectra, no
910 problems are found, because in the spectral analysis only the O₄ cross sections for 223 and
911 293 K were used.

912 In Fig. A28 in appendix A4 the ratios of both fit coefficients (for 203 and 293 K) as well as
913 the derived effective temperatures for the analyses of measured and synthetic spectra are
914 shown. For the measured spectra the ratios are close to zero and the derived temperatures are
915 close to 300K for most of the time (except in early morning and evening), because the
916 effective atmospheric temperature for both days is close to the temperature of the high
917 temperature O₄ cross section (293 K) (see Fig. 13). Similar results (at least around noon) are
918 also obtained for the synthetic spectra if the narrow spectral range (345 – 374 nm) is used. For
919 the standard fit range (including two O₄ bands), however, the ratios are much higher again
920 indicating the effect of the inconsistency of the temperature dependence of the O₄ cross
921 sections (see Fig. A27 in appendix A4).

922

923 4.3.6 Results from different instruments and analyses by different groups

924

925 In this section the effects of using measurements from different instruments and having these
926 spectra analysed by different groups are investigated. For that purpose three different
927 procedures are followed: First, MPIC spectra are analysed by other groups; second, the
928 spectra from other instruments are analysed by MPIC~~non-MPIC instruments are analysed by~~
929 ~~the respective group~~; third, the spectra from non-MPIC instruments~~other instruments~~ are
930 analysed by the respective group~~by MPIC~~.

931 In Fig. 14a and Table A25 (in appendix A4) the comparison results of the analysis of MPIC
932 spectra by other groups versus the analysis of MPIC spectra by MPIC are shown. Especially
933 for 18 June rather large differences (between –6% / +5%) to the MPIC standard analysis are
934 found. Interestingly the largest differences are found in the morning when the aerosol
935 extinction close to the surface was strongest. On 8 July smaller differences (between –6% and
936 –1%) are found.

937 In Fig. 14b and Table A25 (in appendix A4) the comparison results of the analysis of spectra
938 from other instruments by MPIC versus the analysis of MPIC spectra by MPIC are shown.
939 For this comparison all analyses are performed in the spectral range 335 – 374 nm, because
940 the standard spectral range (352 – 387 nm) is not covered by all instruments. Again, the
941 largest differences are found for 18 June (up to ±11%). For 8 July the differences reach up to
942 ±6%, but for this day only a few measurements in the morning are available.

943 In Fig. 14c and Table A25 (in appendix A4) the comparison results of the analysis of spectra
944 from other instruments by the respective group versus the MPIC analysis by MPIC (standard
945 analysis) is shown. From this exercise the combined effects of different instrumental
946 properties and retrievals can be estimated. Interestingly, the observed differences are only
947 slightly larger than those for the analysis of the spectra from the different instruments by
948 MPIC (Fig. 14b). This indicates that the largest errors are related to the differences of the
949 different instruments and not to the settings and implementations of the different retrievals.
950 For the middle period of 18 June the uncertainties are within 12%. This range is also assumed
951 for 8 July. Here it is interesting to note that the derived errors of the spectral analysis are
952 probably not representative for most recent measurement campaigns. For example, during the
953 CINDI-2 campaign (<http://www.tropomi.eu/data-products/cindi-2>) the deviations of the O₄
954 spectral analysis results were much smaller than for the selected days during the MAD-CAT
955 campaign.

956

957 4.3.7 Summary of uncertainties of the O₄ AMF from the spectral analysis

958

959 Table 10 presents an overview on the different sources of uncertainties of the measured O₄
960 (d)AMFs obtained in the previous sub-sections. The uncertainties are expressed as relative
961 deviations from the results for the standard settings (see Table 7) derived by MPIC from
962 spectra of the MPIC instrument

963 Like for the simulation results, in general, larger uncertainties are found for the O₄ dAMFs
964 compared to the O₄ AMFs. This is expected because the uncertainties of the O₄ dAMFs
965 contain the uncertainties of two analyses (at 90° elevation and at low elevation). Also, the
966 uncertainties on 18 June are again larger than on 8 July. This finding was not expected, but is
967 possibly related to the higher trace gas abundances (see Fig. 1 and Table A3 in appendix A1)
968 and the higher aerosol extinction close to the surface on 18 June.

969 Another interesting finding is that the uncertainties of the spectral analysis of O₄ are
970 dominated by the effect of instrumental properties up to ±12% in the morning of 18 June.
971 Further important uncertainties are associated with the choice of the wavelength range, the
972 degree of the polynomial and the intensity offset. In contrast, the exact choices of the trace
973 gas cross sections (including their wavelength- and temperature dependencies) play only a
974 minor role (up to a few percent). Excellent agreement (within ±1%) is in particular found for
975 the O₄ analysis of the synthetic spectra using the standard settings and the directly simulated
976 O₄ (d)AMFs at 360 nm. This indicates that the O₄ (d)AMFs retrieved in the wavelength range
977 352 – 387 nm are indeed representative for radiative transfer simulations at 360 nm.

978 As for the uncertainties of the simulated O₄ (d)AMFs, the uncertainties of the spectral
979 analysis are also split into a systematic and a random term: the systematic deviations of the O₄
980 dAMFs from those of the standard settings are about +1% and –1.5% for 18 June and 8 July,
981 respectively. The range of uncertainty is calculated from the uncertainty ranges of the
982 different error sources by assuming that they are all independent. The uncertainty ranges for
983 18 June and 8 July are calculated as ±12.5% and ±10.8%, respectively.

984

985 **4.4 Recommendations derived from the sensitivity studies**

986

987 In this section a short summary of the most important findings from the sensitivity studies is
988 given.

989

990 **Temperature and pressure profiles**

991 Temperature and pressure profiles from sondes or model data should be used if available.
992 Alternatively, of temperature and pressure profiles extrapolated from surface measurements
993 could be used. Typical uncertainties of the O₄ VCD derived from such profiles are still < 2%.
994 For high temperature (>20°C) the atmospheric humidity should be considered. If no
995 measurements are available, prescribed profiles, e.g. from the US standard atmosphere can be
996 used. However, depending on location and season the errors of the resulting O₄ VCD can be
997 rather large (see also Ortega et al., 2016).

998

999 **Integration of the O₄ VCD**

1000 The integration should be performed on a vertical grid with at least 100 m resolution up to an
1001 altitude of 30 km. The surface altitude should be taken into account with an accuracy of at
1002 least 20 m.

1003

1004 **Measurements and spectral analysis**

1005 Instruments should have a small FOV (≤1°), an accurate elevation calibration (better than
1006 0.5°), and a small and preferably well characterized stray light level. For the data analysis the
1007 standard settings as provided in Table 7 should be used. From the analysis of synthetic spectra
1008 it was found that the results for these settings are consistent with simulated O₄ (d)AMFs
1009 within 1 %.

1010
1011
1012
1013
1014
1015
1016
1017
1018
1019
1020
1021
1022
1023
1024
1025
1026
1027
1028
1029
1030
1031
1032
1033
1034
1035
1036
1037
1038
1039
1040
1041
1042
1043
1044
1045
1046
1047
1048
1049
1050
1051
1052
1053
1054
1055
1056
1057
1058
1059

Information on aerosols

Aerosol profiles should be obtained from LIDARs or ceilometers using similar wavelengths as the MAX-DOAS measurements. Preferred LIDAR types are HSRL or Raman LIDARs, which directly provide profiles of aerosol extinction and thus need no assumptions on the LIDAR ratio. They should also have high signal to noise ratios and shallow blind region at the surface in order to cover a large altitude range. Information on aerosol optical properties and size distributions from sun photometers or in situ measurements should be used.

RTM simulations

Radiative transfer models should use Mie phase functions e.g. derived from sun photometer observations. The consideration of polarisation and rotational Raman scattering is not necessary.

If such optimised settings are used, the errors of the radiative transfer simulations and spectral analysis can be largely reduced: the uncertainties of the O_4 dAMFs related to radiative transfer simulations can be reduced from about $\pm 8\%$ as in this study to about $\pm 4\%$; those related to the spectral analysis can be reduced from about $\pm 10\%$ to about $\pm 6\%$.

4.4.1 Preferred scenarios for future studies

In addition to the recommendations given above, future campaigns should aim to cover different meteorological conditions (e.g. low temperatures), viewing geometries (e.g. low SZA), surface albedos (e.g. snow and ice) and wavelengths (e.g. 477, 577, and 630 nm). Also different aerosol scenarios including those with low aerosol optical depths should be covered. Max-DOAS measurements should be performed by at least 2, preferably more instruments. In order to minimise the effects of instrumental properties, the instruments should be well calibrated and should have low straylight levels. Based on the above criteria, measurements during the CINDI-2 campaign are probably well suited for a similar study.

5 Comparison of measurements and simulations

The comparison results for both days are different: On 18 June (except in the evening) measurements and simulations agree within errors (the ratio of simulated and measured O_4 dAMFs for the middle period of that day is 1.01 ± 0.16). In contrast, on 8 July measurements and simulations significantly disagree: Taking into account the errors of the VCD calculation (3%), the radiative transfer simulations ($+16 \pm 6.4\%$) and the spectral analysis ($-1.5 \pm 10.8\%$) for the middle period of that day results in a ratio of simulated and measured O_4 dAMFs of 0.81 ± 0.10 , which differs significantly from unity.

5.1 Important differences between both days

On both selected days similar aerosol AOD were measured. Also the diurnal variation of the SZA was similar because of the proximity to summer solstice. However, also many differences are found for the two days, which are discussed below.

a) temperature, pressure, wind:

1060 On 18 June surface pressure was lower by about 13 hPa and surface temperature was higher
1061 by about 7K than on 8 July, respectively. These differences were explicitly taken into account
1062 in the calculation of the O₄ profiles / VCDs, the radiative transfer simulations and the
1063 interpretation of the spectral analyses. Thus they can very probably not explain the different
1064 comparison results on the two days.

1065 On both days, wind was mainly blowing from East-North-East, but on 18 June it was blowing
1066 from West before about 08:00 and after 20:00 UTC. Wind speeds were lower on 18 June
1067 (between 1 and 2 m/s) than on 8 July (between 1 and 3 m/s).

1068

1069 b) aerosol properties:

1070 The in situ aerosol measurements show very different abundances and properties of aerosols
1071 close to the ground for the selected days. On 18 June much larger concentrations of larger
1072 aerosol particles are found, which cannot be measured by the ceilometer, because the lowest
1073 detecting altitude is 180m. Thus it can be concluded that the enhanced aerosol concentration
1074 on 18 June is confined to a shallow layer at the surface. In general the aerosol concentrations
1075 close to the surface are more variable on 18 June than on 8 July. The high aerosol
1076 concentrations close to the surface probably also affect the LIDAR ratio, which is thus
1077 probably more variable on 18 June. Similarly, also the phase function derived from the sun
1078 photometer (for the integrated aerosol profile) is probably less representative for the low
1079 elevation angles on 18 June because different aerosol size distributions probably existed at
1080 different altitudes. Finally, the Ångström parameter derived from AERONET observations is
1081 different for both days, especially for large wavelengths, which is in qualitative agreement
1082 with the higher in situ aerosol concentrations of large particles on 18 June. Also a larger
1083 forward peak of the derived aerosol phase function is found for 18 June. Both effects probably
1084 cause larger uncertainties on 18 June.

1085

1086 c) spectral analysis

1087 Larger uncertainties of the spectral analysis are found for 18 June compared to 8 July. This
1088 finding was surprising, but was also partly reproduced by the analysis of the synthetic spectra.
1089 One possible explanation is the smaller wavelength dependence of aerosol scattering at low
1090 altitudes on 18 June, which mainly affects measurements at low elevation angles. When
1091 analysed versus a zenith reference, for which the broad band wavelength dependency is much
1092 stronger (because of the larger contribution from Rayleigh scattering), larger deviations can
1093 be expected (e.g. because of differences of instrumental straylight, or the different detector
1094 saturation levels). On 18 June also higher (about doubled) NO₂ and HCHO concentrations are
1095 present compared to 8 July possibly leading to increased spectral interferences with the O₄
1096 absorption, but this effect is expected to be small.

1097

1098

1099 **5.2 Which conditions would be needed to bring measurements and simulations on 8 July**
1100 **into agreement**

1101

1102 This section describes possible (but mostly unrealistic) changes of the atmospheric scenario,
1103 the instrument properties or the input parameters, which could bring measurements and
1104 simulations on 8 July into agreement. If e.g. the aerosol extinction profile is scaled by 0.65,
1105 the corresponding O₄ dAMFs would almost perfectly match the measured ones. In principle
1106 also horizontal gradients of the aerosol extinction could explain the discrepancy. While we are
1107 not able to quantify them, they surely would have to be of the order of several ten percent per
1108 10 km. Another possibility would be aerosol phase functions with very high asymmetry
1109 parameters (>> 0.75). Also systematic errors of the O₄ cross section could explain the
1110 observed discrepancies. Finally, an overcorrection of spectrograph straylight (or any other

1111 intensity offset) could be explain the discrepancies. However, a rather high overcorrection (by
1112 about 20%) would be needed.

1116 ~~5-6 Discussion and e~~Conclusions

1117
1118 We compared MAX-DOAS observations of the atmospheric O₄ absorption with
1119 corresponding radiative transfer simulations for two mainly cloud-free days during the MAD-
1120 CAT campaign. A large part of this study is dedicated to the extraction of input information
1121 for the radiative transfer simulations and the quantification of the associated errors of the
1122 radiative transfer simulations and spectral retrievals. One important result was from the
1123 sensitivity studies is that the O₄ results derived from the analysis of synthetic spectra using the
1124 standard settings are consistent with the simulated O₄ air mass factors within 1%. Also
1125 recommendations for the settings of the radiative transfer simulations, in particular on the
1126 extraction of aerosol and O₄ profiles are given. One important result is that the quality of the
1127 aerosol data sets is crucial to constrain the radiative transfer simulations. For example, it is
1128 recommended that LIDAR instruments are operated at wavelengths close to those of the
1129 MAX-DOAS measurement and have a small sensitivity gap close to the surface. Further
1130 aerosol properties (e.g. size distributions, phase functions) should be available from sun
1131 photometer and/or in situ measurements. If such aerosol data are available the corresponding
1132 uncertainties of the radiative transfer simulations could be largely reduced to about ±5%.
1133 Similar uncertainties can also be expected for optimum instrument operations and data
1134 analyses.

1135 The comparison results for both days are different: On 18 June (except in the evening)
1136 measurements and simulations agree within errors (the a ratio of simulated and measured O₄
1137 dAMFs for the middle period of that day is 1.01 ± 0.16). In contrast, on 8 July measurements
1138 and simulations significantly disagree: Taking into account the errors of the VCD calculation
1139 (3%), the radiative transfer simulations ($\pm 16 \pm 6.41\%$) and the spectral analysis ($-1.5 \pm 10.8\%$)
1140 for the middle period of that day results in a ratio of simulated and measured O₄ dAMFs of
1141 $0.71-81 \pm 0.12-10$, which differs significantly from unity. No plausible explanation for the
1142 observed discrepancies on 8 July were found.

1143 ~~On 18 June larger uncertainties both for the measurements and radiative transfer simulations~~
1144 ~~exist, mainly related to the high aerosol concentration close to the surface. A summary of the~~
1145 ~~most important differences between both days is given in section 5.1.~~

1146 ~~A large part of this study was dedicated to the extraction of input information for the radiative~~
1147 ~~transfer simulations and to the quantification of the errors of the radiative transfer simulations~~
1148 ~~and spectral retrievals. In particular, the analysis of synthetic spectra indicated that the O₄~~
1149 ~~results derived from the spectral analysis using the standard settings are consistent with the~~
1150 ~~simulated O₄ air mass factors within 1%.~~

1151 ~~Based on this study, also recommendations for similar future studies are derived (see section~~
1152 ~~5.2). In general, the largest errors sources arise from spectral analyses (partly related to~~
1153 ~~imperfections of the MAX-DOAS instruments) and the uncertainties of the aerosol phase~~
1154 ~~functions and extinction profiles. Even if the aerosol extinction profiles could be better~~
1155 ~~constraint, e.g. using results from Raman LIDARs or high spectral resolution LIDARs~~
1156 ~~(HSRL), the uncertainties of the aerosol phase function will remain a critical error source.~~
1157 ~~Future measurements should in particular try to minimize these error sources. Here it should~~
1158 ~~be noted that the general larger errors obtained for 18 June are probably not representative for~~
1159 ~~typical measurement conditions. For example, during the CINDI 2 campaign~~
1160 ~~(<http://www.tropomi.eu/data-products/cindi-2>) the deviations of the O₄ spectral analysis~~
1161 ~~results were much smaller than those for 18 June.~~

1162 ~~The main conclusion from this study is that on one of the two selected days during the~~
1163 ~~MADCAT campaign (08 July) a scaling factor (of about 0.71 ± 0.12) is needed to bring~~
1164 ~~measurements and forward model into agreement.~~ As long as the reason for this deviation is
1165 not understood, it is, however, unclear, how representative these findings are for other
1166 measurements (e.g. from other platforms, at other locations/seasons, for other aerosol loads,
1167 and other wavelengths). Thus further studies spanning a large variety of measurement
1168 conditions and also including other wavelengths are recommended.

1169

1170

1171 **5.1 Important differences between both days**

1172

1173 ~~On both selected days similar aerosol AOD were measured. Also the diurnal variation of the~~
1174 ~~SZA was similar because of the proximity to summer solstice. However, also many~~
1175 ~~differences are found for the two days, which are discussed below.~~

1176

1177 a) temperature, pressure, wind:

1178 ~~On 18 June surface pressure was lower by about 13 hPa and surface temperature was higher~~
1179 ~~by about 7K than on 8 June, respectively. These differences were explicitly taken into account~~
1180 ~~in the calculation of the O_4 profiles / VCDs, the radiative transfer simulations and the~~
1181 ~~interpretation of the spectral analyses. Thus they can very probably not explain the different~~
1182 ~~comparison results on the two days.~~

1183 ~~On both days, wind was mainly blowing from East North East, but on 18 June it was blowing~~
1184 ~~from West before about 08:00 and after 20:00 UTC. Wind speeds were lower on 18 June~~
1185 ~~(between 1 and 2 m/s) than on 8 July (between 1 and 3 m/s).~~

1186

1187 b) aerosol properties:

1188 ~~The in situ aerosol measurements show very different abundances and properties of aerosols~~
1189 ~~close to the ground for the selected days. On 18 June much larger concentrations of larger~~
1190 ~~aerosol particles are found, which cannot be measured by the ceilometer, because the lowest~~
1191 ~~detecting altitude is 180m. Thus it can be concluded that the enhanced aerosol concentration~~
1192 ~~on 18 June is confined to a shallow layer at the surface. In general the aerosol concentrations~~
1193 ~~close to the surface are more variable on 18 June than on 8 July. The high aerosol~~
1194 ~~concentrations close to the surface probably also affect the LIDAR ratio, which is thus more~~
1195 ~~variable on 18 June. Since a constant LIDAR ratio is used for the extraction of the aerosol~~
1196 ~~extinction profiles, also the uncertainties of the aerosol profile are probably larger on 18 June.~~
1197 ~~Similarly, also the phase function derived from the sun photometer (for the integrated aerosol~~
1198 ~~profile) is probably less representative for the low elevation angles on 18 June because~~
1199 ~~different aerosol size distributions probably existed at different altitudes. Finally, the~~
1200 ~~Ångström parameter derived from AERONET observations is different for both days,~~
1201 ~~especially for large wavelengths, which is in qualitative agreement with the higher in situ~~
1202 ~~aerosol concentrations of large particles on 18 June. Also a larger forward peak of the derived~~
1203 ~~aerosol phase function is found for 18 June. Both effects probably cause larger uncertainties~~
1204 ~~on 18 June.~~

1205

1206 e) spectral analysis

1207 ~~Larger uncertainties of the spectral analysis are found for 18 June compared to 8 July. This~~
1208 ~~finding was surprising, but was also partly reproduced by the analysis of the synthetic spectra.~~
1209 ~~One possible explanation is the smaller wavelength dependence of aerosol scattering at low~~
1210 ~~altitudes on 18 June, which mainly affects measurements at low elevation angles. When~~
1211 ~~analysed versus a zenith reference, for which the broad band wavelength dependency is much~~
1212 ~~stronger (because of the larger contribution from Rayleigh scattering), larger deviations can~~

1213 ~~be expected (e.g. because of differences of instrumental straylight, or the different detector~~
1214 ~~saturation levels). On 18 June also higher (about doubled) NO₂ and HCHO concentrations are~~
1215 ~~present compared to 8 July possibly leading to increased spectral interferences with the O₄~~
1216 ~~absorption, but this effect is expected to be small.~~

1219 **5.2 Recommendations**

1220
1221 ~~Based on the findings of this comparison study, recommendations for similar future studies~~
1222 ~~are derived. Part of them are also of interest for the interpretation of O₄ measurements in~~
1223 ~~general.~~

1225 ~~a) VCD calculation~~

1226 ~~Temperature and pressure profiles representative for individual days should be used. If such~~
1227 ~~profiles are not available, also profiles extrapolated from surface measurements can be used.~~
1228 ~~They are not ‘perfect’ but usually the associated errors are at the percent level. The vertical~~
1229 ~~grid for the integration of the O₄ profile should not be coarser than 100m. The integration~~
1230 ~~should be carried out up to an altitude of at least 30 km. The exact height of the instrument~~
1231 ~~position needs to be taken into account.~~

1233 ~~b) Radiative transfer simulations~~

1234 ~~If available appropriate phase functions (e.g. from Mie calculations) should be used. Here it is~~
1235 ~~important to note that even if appropriate asymmetry parameters are available, the often used~~
1236 ~~HG parameterisation becomes very imprecise for forward scattering geometries.~~

1238 ~~e) Spectral analysis~~

1239 ~~The spectral range should cover the two O₄ bands at 360 and 380 nm. An intensity offset~~
1240 ~~should be included in the analysis. If the surface temperature differs strongly (more than 25K)~~
1241 ~~from 300K the effect of the temperature dependence of the O₄ absorption should be~~
1242 ~~considered.~~

1244 ~~d) Preferred scenarios for future studies~~

1245 ~~In particular the uncertainties related to aerosols should be minimised. For example,~~
1246 ~~measurements at rather low AOD (≤ 0.1) and with low temporal variability should be selected.~~
1247 ~~Aerosol profiles should be derived from LIDARs/ceilometers which are sensitive down to very~~
1248 ~~shallow altitudes (low overlap ranges). If possible, Raman LIDARs or high spectral~~
1249 ~~resolution LIDARs (HSRL) should be used, because from such observations the aerosol~~
1250 ~~extinction profile can be derived without the assumption of a LIDAR ratio. Also sun~~
1251 ~~photometer measurements should be available. Besides AOD and the Ångström parameter~~
1252 ~~also information on the phase function and single scattering albedo from these measurements~~
1253 ~~should be used.~~

1254 ~~It would be interesting to cover other meteorological conditions (e.g. low temperatures),~~
1255 ~~viewing geometries (e.g. low SZA), surface albedos (e.g. snow and ice) and wavelengths (e.g.~~
1256 ~~477, 577, and 630 nm).~~

1257 ~~In order to minimise the effects of instrumental properties, the instruments should be well~~
1258 ~~calibrated and should have low straylight levels. At least two instruments should be operated~~
1259 ~~at the same site. Based on the above criteria, measurements during the CINDI-2 campaign are~~
1260 ~~probably well suited for a similar study.~~

1263 **Acknowledgments**

1264
 1265
 1266
 1267
 1268
 1269
 1270
 1271
 1272
 1273
 1274
 1275
 1276
 1277
 1278
 1279
 1280
 1281
 1282
 1283
 1284
 1285
 1286
 1287
 1288
 1289
 1290
 1291
 1292
 1293
 1294
 1295
 1296
 1297
 1298
 1299

We are thankful for several external data sets which were used in this study: Temperature and pressure profiles from the ERAInterim reanalysis data set were provided by the European Centre for Medium-Range Weather Forecasts. In situ measurements of trace gas and aerosol concentrations as well as meteorological data were performed by the environmental monitoring services of the States of Rhineland-Palatinate and Hesse (<http://www.luft-rlp.de> and <https://www.hlnug.de/themen/luft/luftmessnetz.html>). We thank M. O. Andreae and Günther Schebeske for operating the Ceilometer and the AERONET instrument at the Max Planck Institute for Chemistry.

Tables

Table 1 Overview on studies which did not apply a scaling factor (upper part) or did apply a scaling factor (lower part) to the measured O₄ dSCDs. Besides the initial studies proposing a scaling factor (Wagner et al., 2009; Clémer et al., 2010) only studies after 2010 are listed.

Reference	Measurement type	Location and period	O ₄ band (nm)	Scaling factor
Studies which did not apply a scaling factor*				
Thalmann and Volkamer, 2010	CE-DOAS	Laboratory	477	1
Peters et al., 2012a	MAX-DOAS	Western Pacific Ocean (Oct 2009)	360, 477	1
Spinei et al. 2015	Direct sun DOAS	JPL, USA (Jul 2007) Pullman, USA (Sep – Nov 2007, Jul – Nov 2011) Fairbanks, USA (Mar-Apr 2011) Huntsville, USA (Aug 2008) Richland, USA (Apr-Jun 2008) Greenbelt, USA (May 2007, 2012-2014) Cabauw, The Netherlands (Jun-Jul	360, 477	1

		2009)		
Spinei et al., 2015 / Volkamer et al., 2015	Airborne DOAS	Subtropical Pacific Ocean (Jan 2012)	360, 477	1
Ortega et al., 2016	MAX-DOAS	Cape Cod, USA (Jul 2012)	360, 477	1
Schreier et al., 2016	MAX-DOAS	Zugspitze, Germany (Apr-Jul 2003) Pico Espeio, Venezuela (2004 - 2009)	360	1
Seyler et al., 2017	MAX-DOAS	German Bight (2013-2016)	360, 477	1
Wang et al., 2017a,b	MAX-DOAS	Wuxi, China (2011 - 2014)	360	1
Gielen et al., 2017	MAX-DOAS	Bujumbura, Burundi (2013-2015)	360, 477	1
Franco et al., 2015	MAX-DOAS	Jungfrauoch (2010 –2012)	360	1
Studies which did apply a scaling factor				
Wagner et al., 2009	MAX-DOAS	Milano, Italy Sep 2013 (FORMAT II)	360	0.81
Clemer et al., 2010	MAX-DOAS	Beijing, China Jul 2008 – Apr 2009	360, 477, 577, 630	0.80
Irie et al., 2011	MAX-DOAS	Cabauw, The Netherlands Jul-Jun 2009 (CINDI-I)	360, 477	0.75±0.1
Merlaud et al., 2011	Airborne DOAS	Arctic Apr 2008 POLARCAT)	360	0.89
Vlemmix et al., 2011	MAX-DOAS	Cabauw, The Netherlands Jul-Oct 2009 (CINDI-I)	477	0.8
Zieger et al., 2011	Overview on MAX-DOAS	Cabauw, The Netherlands Jul-Oct 2009 (CINDI-I)	360 (MPIC) 477 (BIRA) 477 (IUPHD) 477 (JAMSTEC)	0.83 0.75 0.8 0.8*
Wang et al., 2014	MAX-DOAS	Xianghe, China (2010 - 2013)	360	0.8
Kanaya et al., 2014	MAX-DOAS	Cape Hedo, Japan (2007 – 2012) Fukue, Japan (2008 – 2012) Yokosuda, Japan (2007 – 2012) Gwangju, Korea (2008 – 2012) Hefei, China (2008 – 2012) Zvenigorod; Russia (2009 – 2012)	477 477 477 477 477 477	0.8 0.8 0.8 0.8 0.8 0.8
Hendrick et al., 2014	MAX-DOAS	Beijing, China (2008 - 2009) Xianghe, China (2010 – 2012)	360	0.8
Vlemmix et al., 2015	MAX-DOAS	Beijing, China (2008 - 2009) Xianghe, China (2010 – 2012)	360, 477	0.8
Irie et al., 2015	MAX-DOAS	Tsukuba, Japan (Oct 2010)	477	elevation dependent scaling factor**
Wang et al., 2016	MAX-DOAS	Madrid, Spain (Mar – Sep 2015)	360	0.83
Friess et al., 2016	MAX-DOAS	Cabauw, The Netherlands Jul-Jul 2009 (CINDI-I)	477 (AOIFM) 477 (BIRA) 477 (IUPHD) 477 (JAMSTEC) 360 (MPIC)	0.8 0.8 1 0.8*** 0.77

*The authors of part of these studies were probably not aware that a scaling factor was applied by other groups.

**SF = $1 / (1 + EA/60)$

***SF is varied during profile inversion

1300
1301
1302
1303

1304
1305

Table 2 Periods on both selected days, which are used for the comparisons.

day	1 st period	2 nd period	3 rd period
18 June 2013	8:00 – 11:00 UTC	11:00 – 14:00 UTC	14:00 – 19:00 UTC
8 July 2013	4:00 – 7:00 UTC	7:00 – 11:00 UTC	11:00 – 19:00 UTC

1306
1307
1308
1309

Table 3 Participation of the different groups in the different analysis steps

Abbreviation	Institution	Determination of the O ₄ profile and VCD	Extraction of aerosol profiles	Radiative transfer simulations	Spectral analysis
BIRA	BIRA/IASB, Brussels, Belgium				•
CMA	Meteorological Observation Center, Beijing, China			•	•
CSIC	Department of Atmospheric Chemistry and Climate, Institute of Physical Chemistry Rocasolano (CSIC), Spain.	•			•
INTA	Instituto Nacional de Tecnica Aeroespacial, Spain	•	•	•	•
IUP-B	University of Bremen, Germany		•	•	•
IUP-HD	University of Heidelberg, Germany				•
LMU	Ludwig-Maximilians-Universität München, Germany	•	•		
MPIC	MPI for chemistry, Mainz, Germany	•	•	•	•

1310
1311
1312
1313

Table 4 Overview on properties of MAX-DOAS instruments participating in this study

Institute / Instrument type	Spectral range (nm)	Spectral resolution (FWHM, nm)	Spectral range per detector pixel (nm)	Detector type / temperature	Integration time of individual spectra (s)	Reference
BIRA / 2-D scanning MAX-DOAS	300 - 386	0.49	0.04	2-D back-illuminated CCD, 2048 x 512 pixels / -40 °C	60	Clémer et al., 2010
IUP-Bremen / 2-D scanning MAX-DOAS	308 - 376	0.43	0.05	2-D back-illuminated CCD, 1340 x 400 pixels / -35 °C	20	Peters et al., 2012b

IUP-Heidelberg / 1-D scanning MAX-DOAS	294 - 459	0.59	0.09	AvaSpec-ULS 2048 pixels back-thinned Hamamatsu CCD S11071-1106 / 20°C	60	Lampel et al., 2015
MPIC / 4-azimuth MAX-DOAS	320 – 457	0.67	0.14	2-D back-illuminated CCD, 1024 x 255 Pixels / -30°C	10 s	Krautwurst, 2010

1314
1315
1316
1317
1318
1319
1320
1321
1322
1323
1324
1325
1326
1327
1328
1329
1330
1331
1332
1333
1334
1335
1336
1337
1338
1339
1340
1341

Table 5 Independent data sets used to constrain the atmospheric properties during both selected days.

Measurement / data set	Measured quantities	Derived quantities	Temporal / spatial resolution	Source / reference
Ceilmeter	Attenuated backscatter profiles* at 1064 nm	Aerosol extinction profiles at 360 nm	30s** / 15 m	Wiegner and Geiß, 2012
AERONET sun photometer	Solar irradiances, Sky radiances	Aerosol optical depth, single scattering albedo, phase function	Typical integration time: 2 to 15 min	Holben et al., 2001, https://aeronet.gsfc.nasa.gov/
Surface	temperature,		1h	http://www.luft-

measurements air quality stations in Mainz Mombach	pressure, rel. humidity			rlp.de
Surface measurements air quality stations in Mainz and Wiesbaden	pm _{2.5} pm ₁₀		1h (Mainz stations) 30 min (Wiesbaden stations)***	http://www.luft-rlp.de https://www.hlnug.de/themen/luft/luftmessnetz.html
ECMWF ERA-Interim reanalysis	temperature, Pressure, rel. humidity		Average over the area 49.41°-50.53° N, 7.88°-9.00° E, every 6 h	(Dee et al., 2011)

1342 *no useful signal below 180m due to limited overlap

1343 **Here 15 min averages are used.

1344 ***Stations in Mainz: Parcusrstrasse, Zitadelle, Mombach; Stations in Wiesbaden: Schierstein,
1345 Ringkirche, Süd

1346

1347

1348

1349

1350

Table 6 Standard settings for the radiative transfer simulations

Parameter	Standard setting
Temperature and pressure profile	MPIC extraction
O ₄ profile	MPIC extraction
Surface albedo	5 %
Aerosol single scattering albedo	0.95
Aerosol phase function	HG model with asymmetry parameter of 0.68
Aerosol extinction profile	MPIC extraction with linear interpolation < 180 m
Polarisation	Not considered
Raman scattering	Partly considered for synthetic spectra

1351

1352

1353

1354

Table 7 Standard settings for the DOAS analysis of O₄.

Parameter	Value, Remark / Reference
Spectral range	352 – 387 nm
Degree of DOAS polynomial	5
Degree of intensity offset polynomial	2
Fraunhofer reference spectrum	08 July, 10:05:35, SZA: 32.37°, elevation angle: 90° (this spectrum is used for both days)
Wavelength calibration	Fit to high resolution solar spectrum using Gaussian slit function
Shift / squeeze	The measured spectrum is shifted and squeezed against all other spectra
Ring spectrum 1	Normal Ring spectrum calculated from DOASIS
Ring spectrum 2	Ring spectrum 1 multiplied by λ^{-4}
O ₃ cross section	223 K, Bogumil et al. (2003)

NO ₂ cross section	294 K, Vandaele et al. (1997)
BrO cross section	223 K, Fleischmann et al. (2004)
O ₄ cross section	293 K, Thalman and Volkamer (2013)

1355

1356

1357

1358

Table 8 Average ratios (simulation results divided by measurements) of the O₄ (d)AMFs for both middle periods of the selected days.

Period	18.06.2013, 11:00 – 14:00	08.07.2013, 7:00 – 11:00
AMF ratio	0.97	0.83
DAMF ratio	0.94	0.69

1359

1360

1361

1362

1363

1364

1365

1366

Table 9 Summary of uncertainties of the simulated O₄ (d)AMFs for the middle periods of both selected days. The two numbers left and right of the ‘/’ indicate the minimum and maximum deviations. The columns with label ‘Optimum’ indicate the uncertainties which could be reached if optimum information on the measurement conditions was available (e.g. height profiles of temperature, pressure and aerosol extinction as well as well aerosol microphysical or optical properties).

	<u>O₄ AMF</u>			<u>O₄ dAMF</u>		
	18 June	8 July	<u>Optimum settings</u>	18 June	8 July	<u>Optimum settings</u>
Effects of RTM						
Radiative transfer model	-1% / +2%	0% / +1%	<u>±1%</u>	-1% / +5%	0% / +3%	<u>±1%</u>
Polarisation	0% / 0%	0% / 0%	<u>0%</u>	0% / 0%	0% / +1%	<u>0%</u>
Effects of input parameters						
O ₄ profile extraction	0% / + 2%	0% / + 1%	<u>±1%</u>	0% / + 4%	0% / + 2%	<u>±1%</u>
Single scattering albedo	-1% / + 3%	-1% / + 1%	<u>0%</u>	-1% / + 3%	-1% / + 1%	<u>0%</u>
Phase function	-3% / +3%	-2% / 0%	<u>±1%</u>	-5% / + 9%	-5% / +2%	<u>±1.5%</u>
Aerosol profile extraction	-1% / + 1%*	-2% / + 2%	<u>±1%</u>	-2% / + 1%*	-4% / + 4%	<u>±1.5%</u>
Extrapolation below 180 m	0% / + 2%	-1% / + 1%	<u>0%</u>	-1% / + 4%	-2% / + 2%	<u>0%</u>
<u>LIDAR ratio & wrong wavelength</u>	<u>?</u>	<u>+5% / +6%</u>	<u>±2%**</u>	<u>?</u>	<u>+13% / +17%</u>	<u>±3%**</u>
Surface albedo	0% / + 2%	0% / + 1%	<u>0%</u>	0% / + 2%	-1% / + 0%	<u>0%</u>
Total uncertainty						
Average deviation (from results for	+4.5%	<u>+0.56%</u>		+8.5%	<u>+16%</u>	

standard settings)						
Range of uncertainty	$\pm 4.4\%*$	$\pm 2.8\%$	$\pm 2.8%**$	$\pm 8.7%*$	$\pm 6.14\%$	$\pm 3.8%**$

1367
1368
1369
1370
1371
1372
1373
1374
1375
1376

*this uncertainty does not contain the contribution from variation of aerosol properties with altitude, see text
**if LIDAR profiles at the same wavelength and without gaps in the troposphere were available.

Table 10 Summary of uncertainties of the measured O₄ (d)AMFs for the middle periods of both selected days. The two numbers left and right of the ‘/’ indicate the minimum and maximum deviations. The columns with label ‘Optimum’ indicate the uncertainties which could be reached if optimum instrumental performance was ensured and optimum cross section were available.

	<u>O₄ AMF</u>			<u>O₄ dAMF</u>		
	18 June	8 July	<u>Optimum</u>	18 June	8 July	<u>Optimum</u>
Consistency spectral analysis versus RTM						
Analysis of synthetic spectra	-1% / +1%	-1% / 0%	$\pm 1\%$	0% / 0%	0% / +1%	$\pm 1\%$
Fit settings						
Spectral range	-7% / -3%	-3% / 0%	$\pm 1\%$	-12% / -1%	-6% / -1%	$\pm 1\%$
Degree of polynomial	+0% / +4%	0% / + 3%	$\pm 1\%$	0% / +6%	0% / +6%	$\pm 1\%$
Intensity offset*	+1% / +5%	+1% / +3%	$\pm 1\%$	+3% / +11%	+2% / +4%	$\pm 1.5\%$
Ring	+1% / +2%	-1% / +1%	$\pm 1\%$	+1% / +1%	-1% / +1%	$\pm 1.5\%$
Temperature dependence of NO ₂ absorption	0% / 0%	0% / 0%	<u>0%</u>	0% / 0%	0% / 0%	<u>0% / 0%</u>
Wavelength dependence of NO ₂ absorption	-1% / 0%	0% / 0%	<u>0%</u>	-2% / -1%	-1% / 0%	<u>0%</u>
Wavelength dependence of O ₄ absorption	-1% / 0%	-1% / -1%	<u>0%</u>	0% / +1%	-1% / -1%	<u>0%</u>
Including H ₂ O cross section	0% / 0%	0% / 0%	<u>0%</u>	+1% / +1%	+1% / +1%	<u>0%</u>
Including HCHO cross section	-3% / 0%	-1% / 0%	<u>0%</u>	-6% / -4%	-3% / -2%	<u>0%</u>
Different O ₄ cross sections*	-2% / +1%	-2% / +1%	$\pm 2\%$	-3% / +3%	-3% / +3%	$\pm 2\%$
Temperature dependence of the O₄ absorption						
Analysis using two O ₄ cross	0% / 0%	+2% / +2%	$\pm 1\%$	+4% / +4%	+1% / +1%	$\pm 1.5\%$

sections for different temperatures [♥]							
Analysis of synthetic spectra for different surface temperatures	-1% / 0%	-1% / +2%			+4% / +4%	+1% / +1%	
Analysis from different instruments and groups							
Different groups and analyses [♦]	-6% / + 5%	-6% / + 5%	<u>±3%</u> [▲]		-12% / +7%	-12% / +7%	<u>±4.5%</u>
Total uncertainty							
Average deviation (from results for standard settings)	-4.5%	-0.5%			+1%	-1.5%	
Range of uncertainty	±7.0%	±6.5%	<u>±4.2%</u>		±12.5%	±10.8%	<u>±5.7%</u>

1377 *here the case ‘no offset’ is not considered

1378 *here the case of the non-shifted Greenblatt O₄ cross section is not considered

1379 ♥here only the results for the measured spectra in the spectral range 352 – 387 nm are
1380 considered. (temperatures on 18 June: 27–31 °C; 8 July: 20–30 °C)

1381 ♦The results for 18 June are also taken for 8 July due to the lack of measurements on 8 July

1382 ▲see Kreher et al., 2019

1383

1384

1385 References

1386

1387 Acarreta, J. R., De Haan, J. F., and Stammes, P.: Cloud pressure retrieval using the O₂-O₂
1388 absorption band at 477 nm, J. Geophys. Res., 109, D05204, doi:10.1029/2003JD003915,
1389 2004.

1390

1391 Bogumil, K., J. Orphal, T. Homann, S. Voigt, P. Spietz, O.C. Fleischmann, A. Vogel, M.
1392 Hartmann, H. Bovensmann, J. Frerik and J.P. Burrows, Measurements of Molecular
1393 Absorption Spectra with the SCIAMACHY Pre-Flight Model: Instrument Characterization
1394 and Reference Data for Atmospheric Remote-Sensing in the 230-2380 nm Region, J.
1395 Photochem. Photobiol. A., 157, 167-184, 2003.

1396

1397 Chance, K.V., and R.L. Kurucz, An improved high-resolution solar reference spectrum for
1398 earth’s atmosphere measurements in the ultraviolet, visible, and near infrared, J. Quant.
1399 Spectrosc. Radiat. Transfer, 111, 1289-1295, 2010.

1400

1401 Chandrasekhar S. Radiative Transfer. New York: Dover Publications Inc.; 1960.

1402

1403 Chandrasekhar S. Selected papers, vol. 2. New York: University of Chicago Press, 1989.

1404
1405 Clémer, K., Van Roozendael, M., Fayt, C., Hendrick, F., Hermans, C., Pinardi, G., Spurr, R.,
1406 Wang, P., and De Mazière, M.: Multiple wavelength retrieval of tropospheric aerosol optical
1407 properties from MAXDOAS measurements in Beijing, *Atmos. Meas. Tech.*, 3, 863-878,
1408 doi:10.5194/amt-3-863-2010, 2010.
1409
1410 Dee, D. P., Uppala, S. M., Simmons, A. J., Berrisford, P., Poli, P., Kobayashi, S., Andrae, U.,
1411 Balmaseda, M. A., Balsamo, G., Bauer, P., Bechtold, P., Beljaars, A. C. M., van de Berg, L.,
1412 Bidlot, J., Bormann, N., Delsol, C., Dragani, R., Fuentes, M., Geer, A. J., Haimberger, L.,
1413 Healy, S. B., Hersbach, H., Hólm, E. V., Isaksen, I., Kallberg, P., Köhler, M., Matricardi,
1414 M., McNally, A. P., Monge-Sanz, B. M., Morcrette, J.-J., Park, B.-K., Peubey, C., de Rosnay,
1415 P., Tavolato, C., Thépaut, J.-N., and Vitart, F.: The ERA-Interim reanalysis: configuration
1416 and performance of the data assimilation system, *Q. J. Roy. Meteorol. Soc.*, 137, 553–597,
1417 doi:10.1002/qj.828, 2011.
1418
1419 Deutschmann, T., Beirle, S., Frieß, U., Grzegorski, M., Kern, C., Kritzen, L., Platt, U., Pukite,
1420 J., Wagner, T., Werner, B., and Pfeilsticker, K.: The Monte Carlo Atmospheric Radiative
1421 Transfer Model McArtim: Introduction and Validation of Jacobians and 3D Features, *J.*
1422 *Quant. Spectrosc. Ra.*, 112, 1119–1137, doi:10.1016/j.jqsrt.2010.12.009, 2011.
1423
1424 Dubovik, O., Holben, B. N., Eck, T. F., Smirnov, A., Kaufman, Y. J., King, M. D., Tanré, D.,
1425 and Slutsker, I.: Variability of absorption and optical properties of key aerosol types observed
1426 in worldwide locations, *J. Atmos. Sci.*, 59, 590–608, 2002.
1427
1428 Erle, F., K. Pfeilsticker, and U. Platt, On the influence of tropospheric clouds on zenith-
1429 scattered-light measurements of stratospheric species, *Geophys. Res. Lett.*, 22, 2725- 2728,
1430 1995.
1431
1432 Fleischmann, O. C., Hartmann, M., Burrows, J. P., and Orphal, J.: New ultraviolet absorption
1433 cross-sections of BrO at atmospheric temperatures measured by time-windowing Fourier
1434 transform spectroscopy, *J. Photoch. Photobio. A*, 168, 117–132, 2004.
1435
1436 Franco, B., Hendrick, F., Van Roozendael, M., Müller, J.-F., Stavrou, T., Marais, E. A.,
1437 Bovy, B., Bader, W., Fayt, C., Hermans, C., Lejeune, B., Pinardi, G., Servais, C., and Mahieu,
1438 E.: Retrievals of formaldehyde from ground-based FTIR and MAX-DOAS observations at the
1439 Jungfraujoch station and comparisons with GEOS Chem and IMAGES model simulations,
1440 *Atmos. Meas. Tech.*, 8, 1733-1756, <https://doi.org/10.5194/amt-8-1733-2015>, 2015.
1441
1442 Frieß, F., P. S. Monks, J. J. Remedios, A. Rozanov, R. Sinreich, T. Wagner, and U. Platt,
1443 MAX-DOAS O₄ measurements: A new technique to derive information on atmospheric
1444 aerosols. (II) Modelling studies, *J. Geophys. Res.*, 111, D14203,
1445 doi:10.1029/2005JD006618.2006.
1446
1447 Frieß, U., Klein Baltink, H., Beirle, S., Clémer, K., Hendrick, F., Henzing, B., Irie, H., de
1448 Leeuw, G., Li, A., Moerman, M. M., van Roozendael, M., Shaiganfar, R., Wagner, T., Wang,
1449 Y., Xie, P., Yilmaz, S., and Zieger, P.: Intercomparison of aerosol extinction profiles retrieved
1450 from MAX-DOAS measurements, *Atmos. Meas. Tech.*, 9, 3205-3222,
1451 <https://doi.org/10.5194/amt-9-3205-2016>, 2016.
1452
1453 Gielen, C., Hendrick, F., Pinardi, G., De Smedt, I., Fayt, C., Hermans, C., Stavrou, T.,
1454 Bauwens, M., Müller, J.-F., Ndenzako, E., Nzohabonayo, P., Akimana, R., Niyonzima, S.,

1455 Van Roozendael, M., and De Mazière, M.: Characterisation of Central-African aerosol and
1456 trace-gas emissions based on MAX-DOAS measurements and model simulations over
1457 Bujumbura, Burundi, *Atmos. Chem. Phys. Discuss.*, <https://doi.org/10.5194/acp-2016-1104>,
1458 in review, 2017.

1459

1460 Greenblatt G.D., Orlando, J.J., Burkholder, J.B., and Ravishankara, A.R.: Absorption
1461 measurements of oxygen between 330 and 1140 nm, *J. Geophys. Res.*, 95, 18577-18582,
1462 1990.

1463

1464 Hendrick, F., Van Roozendael, M., Kylling, A., Petritoli, A., Rozanov, A., Sanghavi, S.,
1465 Schofield, R., von Friedeburg, C., Wagner, T., Wittrock, F., Fonteyn, D., and De Mazière, M.:
1466 Intercomparison exercise between different radiative transfer models used for the
1467 interpretation of ground-based zenith-sky and multi-axis DOAS observations, *Atmos. Chem.*
1468 *Phys.*, 6, 93-108, doi:10.5194/acp-6-93-2006, 2006.

1469

1470 Hendrick, F., Müller, J.-F., Clémer, K., Wang, P., De Mazière, M., Fayt, C., Gielen, C.,
1471 Hermans, C., Ma, J. Z., Pinardi, G., Stavrakou, T., Vlemmix, T., and Van Roozendael, M.:
1472 Four years of ground-based MAX-DOAS observations of HONO and NO₂ in the Beijing area,
1473 *Atmos. Chem. Phys.*, 14, 765-781, <https://doi.org/10.5194/acp-14-765-2014>, 2014.

1474

1475 Heue, K.-P., Riede, H., Walter, D., Brenninkmeijer, C. A. M., Wagner, T., Frieß, U., Platt, U.,
1476 Zahn, A., Stratmann, G., and Ziereis, H.: CARIBIC DOAS observations of nitrous acid and
1477 formaldehyde in a large convective cloud, *Atmos. Chem. Phys.*, 14, 6621-6642,
1478 <https://doi.org/10.5194/acp-14-6621-2014>, 2014.

1479

1480 Hönninger, G., von Friedeburg, C., and Platt, U.: Multi Axis Differential Optical Absorption
1481 Spectroscopy (MAX-DOAS), *Atmos. Chem. Phys.*, 4, 231–254, 2004.

1482

1483 Holben, B. N., Tanre, D., Smirnov, A., Eck, T. F., Slutsker, I., Abuhassan, N., Newcomb, W.
1484 W., Schafer, J., Chatenet, B., Lavenue, F., Kaufman, Y. J., Vande Castle, J., Setzer, A.,
1485 Markham, B., Clark, D., Frouin, R., Halthore, R., Karnieli, A., O'Neill, N. T., Pietras, C.,
1486 Pinker, R. T., Voss, K., and Zibordi, G.: An emerging ground-based aerosol climatology:
1487 Aerosol Optical Depth from AERONET, *J. Geophys. Res.*, 106, 12067–12097, 2001.

1488

1489 Irie, H., Kanaya, Y., Akimoto, H., Iwabuchi, H., Shimizu, A., and Aoki, K.: First retrieval of
1490 tropospheric aerosol profiles using MAX-DOAS and comparison with lidar and sky
1491 radiometer measurements, *Atmos. Chem. Phys.*, 8, 341–350, doi:10.5194/acp-8-341-2008,
1492 2008.

1493

1494 Irie, H., Takashima, H., Kanaya, Y., Boersma, K. F., Gast, L., Wittrock, F., Brunner, D.,
1495 Zhou, Y., and Van Roozendael, M.: Eight-component retrievals from ground-based MAX-
1496 DOAS observations, *Atmos. Meas. Tech.*, 4, 1027-1044, [https://doi.org/10.5194/amt-4-1027-](https://doi.org/10.5194/amt-4-1027-2011)
1497 2011, 2011.

1498

1499 Irie, H., Nakayama, T., Shimizu, A., Yamazaki, A., Nagai, T., Uchiyama, A., Zaizen, Y.,
1500 Kagamitani, S., and Matsumi, Y.: Evaluation of MAX-DOAS aerosol retrievals by coincident
1501 observations using CRDS, lidar, and sky radiometer inTsukuba, Japan, *Atmos. Meas. Tech.*,
1502 8, 2775-2788, <https://doi.org/10.5194/amt-8-2775-2015>, 2015.

1503

1504 Kanaya, Y., Irie, H., Takashima, H., Iwabuchi, H., Akimoto, H., Sudo, K., Gu, M., Chong, J.,
1505 Kim, Y. J., Lee, H., Li, A., Si, F., Xu, J., Xie, P.-H., Liu, W.-Q., Dzhola, A., Postlyakov, O.,

1506 Ivanov, V., Grechko, E., Terpugova, S., and Panchenko, M.: Long-term MAX-DOAS
1507 network observations of NO₂ in Russia and Asia (MADRAS) during the period 2007–2012:
1508 instrumentation, elucidation of climatology, and comparisons with OMI satellite observations
1509 and global model simulations, *Atmos. Chem. Phys.*, 14, 7909–7927,
1510 <https://doi.org/10.5194/acp-14-7909-2014>, 2014.

1511
1512 [Kreher, K., M. Van Roozendael, F. Hendrick, A. Apituley, E. Dimitropoulou, U. Friess, A.](#)
1513 [Richter, T. Wagner, L. Ang, M. Anguas, A. Bais, N. Benavent, K. Bognar, A. Borovski, I.](#)
1514 [Bruchkovsky, A. Cede, K.L. Chan, S. Donner, T. Drosoglou, C. Fayt, H. Finkenzeller, N.](#)
1515 [Hao, C. Hermans, S. Hoque, H. Irie, J. Jin, P. Johnston, J. Khayyam Butt, F. Khokhar, T.](#)
1516 [Koenig, J. Ma, A. K. Mishra, M. Navarro-Comas, A. Pazmino, E. Peters, M. Pinharanda, A.](#)
1517 [Piters, O. Postlyakov, C. Prados, O. Rodriguez, R. Querel, A. Saiz-Lopez, S. Schreier, A.](#)
1518 [Seyler, E. Spinei, K. Strong, M. Tiefengraber, J.-L. Tirpitz, V. Kumar, R. Volkamer, M.](#)
1519 [Wenig, P. Xie, J. Xu, M. Yela, X. Zhao, W. Zhuoru, Intercomparison of NO₂, O₄, O₃ and](#)
1520 [HCHO slant column measurements by MAX-DOAS and zenith-sky UV-Visible](#)
1521 [spectrometers, to be submitted to Atmos. Meas. Tech., 2019.](#)

1522
1523 Krautwurst, S.: Charakterisierung eines neu aufgebauten MAXDOAS-Systems und
1524 Interpretation von ersten Messergebnissen zu dem Spurenstoff NO₂, Diplomarbeit,
1525 Fachhochschule Coburg, Coburg, Germany, 2010.

1526
1527 Lampel, J., Frieß, U., and Platt, U.: The impact of vibrational Raman scattering of air on
1528 DOAS measurements of atmospheric trace gases, *Atmos. Meas. Tech.*, 8, 3767–3787,
1529 <https://doi.org/10.5194/amt-8-3767-2015>, 2015.

1530
1531 Lampel, J., Pöhler, D., Polyansky, O. L., Kyuberis, A. A., Zobov, N. F., Tennyson, J., Lodi,
1532 L., Frieß, U., Wang, Y., Beirle, S., Platt, U., and Wagner, T.: Detection of water vapour
1533 absorption around 363 nm in measured atmospheric absorption spectra and its effect on
1534 DOAS evaluations, *Atmos. Chem. Phys.*, 17, 1271–1295, [https://doi.org/10.5194/acp-17-](https://doi.org/10.5194/acp-17-1271-2017)
1535 [1271-2017](https://doi.org/10.5194/acp-17-1271-2017), 2017.

1536
1537 Lorente, A., Folkert Boersma, K., Yu, H., Dörner, S., Hilboll, A., Richter, A., Liu, M.,
1538 Lamsal, L. N., Barkley, M., De Smedt, I., Van Roozendael, M., Wang, Y., Wagner, T., Beirle,
1539 S., Lin, J.-T., Krotkov, N., Stammes, P., Wang, P., Eskes, H. J., and Krol, M.: Structural
1540 uncertainty in air mass factor calculation for NO₂ and HCHO satellite retrievals, *Atmos.*
1541 *Meas. Tech.*, 10, 759–782, <https://doi.org/10.5194/amt-10-759-2017>, 2017.

1542
1543 Meller, R. and G. K. Moortgat, Temperature dependence of the absorption cross sections of
1544 formaldehyde between 223 and 323 K in the wavelength range 225–375 nm, *J. Geophys. Res.*,
1545 105, 7089–7101, 2000.

1546
1547 Merlaud, A., Van Roozendael, M., Theys, N., Fayt, C., Hermans, C., Quennehen, B.,
1548 Schwarzenboeck, A., Ancellet, G., Pommier, M., Pelon, J., Burkhardt, J., Stohl, A., and De
1549 Mazière, M.: Airborne DOAS measurements in Arctic: vertical distributions of aerosol
1550 extinction coefficient and NO₂ concentration, *Atmos. Chem. Phys.*, 11, 9219–9236,
1551 [doi:10.5194/acp-11-9219-2011](https://doi.org/10.5194/acp-11-9219-2011), 2011.

1552
1553 Ortega, I., Berg, L. K., Ferrare, R. A., Hair, J. W., Hostetler, C. A., and Volkamer, R.:
1554 Elevated aerosol layers modify the O₂-O₂ absorption measured by ground-based MAX-
1555 DOAS, *J. Quant. Spectrosc. Ra.*, 176, 34–49, [doi:10.1016/j.jqsrt.2016.02.021](https://doi.org/10.1016/j.jqsrt.2016.02.021), 2016.

1556

1557 Paur, R. J. and Bass, A. M.: The Ultraviolet Cross-Sections of Ozone: II. Results and
1558 temperature dependence, in: Atmospheric ozone; Proc. Quadrennial Ozone Symposium,
1559 edited by: Zeferos, C. S. and Ghazi, A., Halkidiki Greece, 1984, Dordrecht: Reidel, D., 611–
1560 615, 1984.
1561
1562 Peters, E., Wittrock, F., Großmann, K., Frieß, U., Richter, A., and Burrows, J. P.:
1563 Formaldehyde and nitrogen dioxide over the remote western Pacific Ocean: SCIAMACHY
1564 and GOME-2 validation using ship-based MAX-DOAS observations, *Atmos. Chem. Phys.*,
1565 12, 11179–11197, <https://doi.org/10.5194/acp-12-11179-2012>, 2012a.
1566
1567 Peters, E., Wittrock, F., Großmann, K., Frieß, U., Richter, A., and Burrows, J. P.:
1568 Formaldehyde and nitrogen dioxide over the remote western Pacific Ocean: SCIAMACHY
1569 and GOME-2 validation using ship-based MAX-DOAS observations, *Atmos.*
1570 *Chem. Phys.*, 12, 11179–11197, <https://doi.org/10.5194/acp-12-11179-2012>, 2012b.
1571
1572 Pinardi, G., Van Roozendaal, M., Abuhassan, N., Adams, C., Cede, A., Clémer, K., Fayt, C.,
1573 Frieß, U., Gil, M., Herman, J., Hermans, C., Hendrick, F., Irie, H., Merlaud, A., Navarro
1574 Comas, M., Peters, E., Pipers, A. J. M., Puentedura, O., Richter, A., Schönhardt, A.,
1575 Shaiganfar, R., Spinei, E., Strong, K., Takashima, H., Vrekoussis, M., Wagner, T., Wittrock,
1576 F., and Yilmaz, S.: MAX-DOAS formaldehyde slant column measurements during CINDI:
1577 intercomparison and analysis improvement, *Atmos. Meas. Tech.*, 6, 167–185,
1578 <https://doi.org/10.5194/amt-6-167-2013>, 2013.
1579
1580 Polyansky, O.L., A.A. Kyuberis, N.F. Zobov, J. Tennyson, S.N. Yurchenko and L. Lodi
1581 ExoMol molecular line lists XXX: a complete high-accuracy line list for water, *Mon. Not. R.*
1582 *astr. Soc.*, submitted, 2018.
1583
1584 Prados-Roman, C., Butz, A., Deutschmann, T., Dorf, M., Kritzen, L., Minikin, A., Platt, U.,
1585 Schlager, H., Sihler, H., Theys, N., Van Roozendaal, M., Wagner, T., and Pfeilsticker, K.:
1586 Airborne DOAS limb measurements of tropospheric trace gas profiles: case studies on the
1587 profile retrieval of O₄ and BrO, *Atmos. Meas. Tech.*, 4, 1241–1260, [doi:10.5194/amt-4-1241-](https://doi.org/10.5194/amt-4-1241-2011)
1588 2011, 2011.
1589
1590 Puķīte, J., Kühl, S., Deutschmann, T., Platt, U., and Wagner, T.: Extending differential optical
1591 absorption spectroscopy for limb measurements in the UV, *Atmos. Meas. Tech.*, 3, 631–653,
1592 [doi:10.5194/amt-3-631-2010](https://doi.org/10.5194/amt-3-631-2010), 2010.
1593
1594 Schreier, S. F., Richter, A., Wittrock, F., and Burrows, J. P.: Estimates of free-tropospheric
1595 NO₂ and HCHO mixing ratios derived from high-altitude mountain MAX-DOAS
1596 observations at midlatitudes and in the tropics, *Atmos. Chem. Phys.*, 16, 2803–2817,
1597 <https://doi.org/10.5194/acp-16-2803-2016>, 2016.
1598
1599 Serdyuchenko, A., Gorshchev, V., Weber, M., Chehade, W., and Burrows, J. P.: High spectral
1600 resolution ozone absorption cross-sections – Part 2: Temperature dependence, *Atmos. Meas.*
1601 *Tech.*, 7, 625–636, <https://doi.org/10.5194/amt-7-625-2014>, 2014.
1602
1603 Seyler, A., Wittrock, F., Kattner, L., Mathieu-Üffing, B., Peters, E., Richter, A., Schmolke, S.,
1604 and Burrows, J. P.: Monitoring shipping emissions in the German Bight using MAX-DOAS
1605 measurements, *Atmos. Chem. Phys.*, 17, 10997–11023, [https://doi.org/10.5194/acp-17-10997-](https://doi.org/10.5194/acp-17-10997-2017)
1606 2017, 2017.
1607

1608 Sneep, M., de Haan, J. F., Stammes, P., Wang, P., Vanbauce, C., Joiner, J., Vasilkov, A. P.,
1609 and Levelt, P. F.: Three-way comparison between OMI and PARASOL cloud pressure
1610 products, *J. Geophys. Res.*, 113, D15S23, doi:10.1029/2007JD008694, 2008.
1611

1612 Solomon, S., A. L. Schmeltekopf, and R. W. Sanders, On the interpretation of zenith sky
1613 absorption measurements, *J. Geophys. Res.*, 92, 8311-8319, 1987.
1614

1615 Spinei, E., Cede, A., Herman, J., Mount, G. H., Eloranta, E., Morley, B., Baidar, S., Dix, B.,
1616 Ortega, I., Koenig, T., and Volkamer, R.: Ground-based direct-sun DOAS and airborne
1617 MAX-DOAS measurements of the collision-induced oxygen complex, O₂O₂, absorption with
1618 significant pressure and temperature differences, *Atmos. Meas. Tech.*, 8, 793-809,
1619 <https://doi.org/10.5194/amt-8-793-2015>, 2015.
1620

1621 Spurr RJD, Kurosu TP, Chance KV. A linearized discrete ordinate radiative transfer model
1622 for atmospheric remote sensing retrieval. *JQSRT* 2001;68:689–735.
1623

1624 Spurr, R., LIDORT and VLIDORT: Linearized Pseudo-Spherical Scalar and Vector Discrete
1625 Ordinate Radiative Transfer Models for Use in Remote Sensing Retrieval Problems, *Light*
1626 *Scattering Reviews*, Vol. 3, edited by: Kokhanovsky, A., Springer, Berlin Heidelberg,
1627 Germany, 2008.
1628

1629 Stamnes K, Tsay S-C, Wiscombe W, Jayaweera K. Numerically stable algorithm for discrete
1630 ordinate method radiative transfer in multiple scattering and emitting layered media. *Appl Opt*
1631 1988; 27:2502-9.
1632

1633 [Thalman, R. and Volkamer, R.: Inherent calibration of a blue LED-CE-DOAS instrument to](#)
1634 [measure iodine oxide, glyoxal, methyl glyoxal, nitrogen dioxide, water vapour and aerosol](#)
1635 [extinction in open cavity mode, *Atmos. Meas. Tech.*, 3, 1797-1814, 2010.](#)
1636

1637 Thalman, R. and Volkamer, R.: Temperature dependent absorption cross-sections of O₂-O₂
1638 collision pairs between 340 and 630 nm and at atmospherically relevant pressure, *Phys.*
1639 *Chem. Chem. Phys.*, 15, 15371, doi:10.1039/c3cp50968k, 2013.
1640

1641 United States Committee on Extension to the Standard Atmosphere: U.S. Standard
1642 Atmosphere, 1976, National Oceanic and Atmospheric Administration, National Aeronautics
1643 and Space Administration, United States Air Force, Washington D.C., 1976.
1644

1645 Vandaele, A. C., C. Hermans, P. C. Simon, M. Carleer, R. Colin, S. Fally, M.-F. Méridienne, A.
1646 Jenouvrier, and B. Coquart, Measurements of the NO₂ Absorption Cross-section from 42000
1647 cm⁻¹ to 10000 cm⁻¹ (238-1000 nm) at 220 K and 294 K, *J. Quant. Spectrosc. Radiat.*
1648 *Transfer*, 59, 171-184, 1997.
1649

1650 Vlemmix, T., Piters, A. J. M., Berkhout, A. J. C., Gast, L. F. L., Wang, P., and Levelt, P. F.:
1651 Ability of the MAX-DOAS method to derive profile information for NO₂: can the boundary
1652 layer and free troposphere be separated?, *Atmos. Meas. Tech.*, 4, 2659-2684,
1653 <https://doi.org/10.5194/amt-4-2659-2011>, 2011.
1654

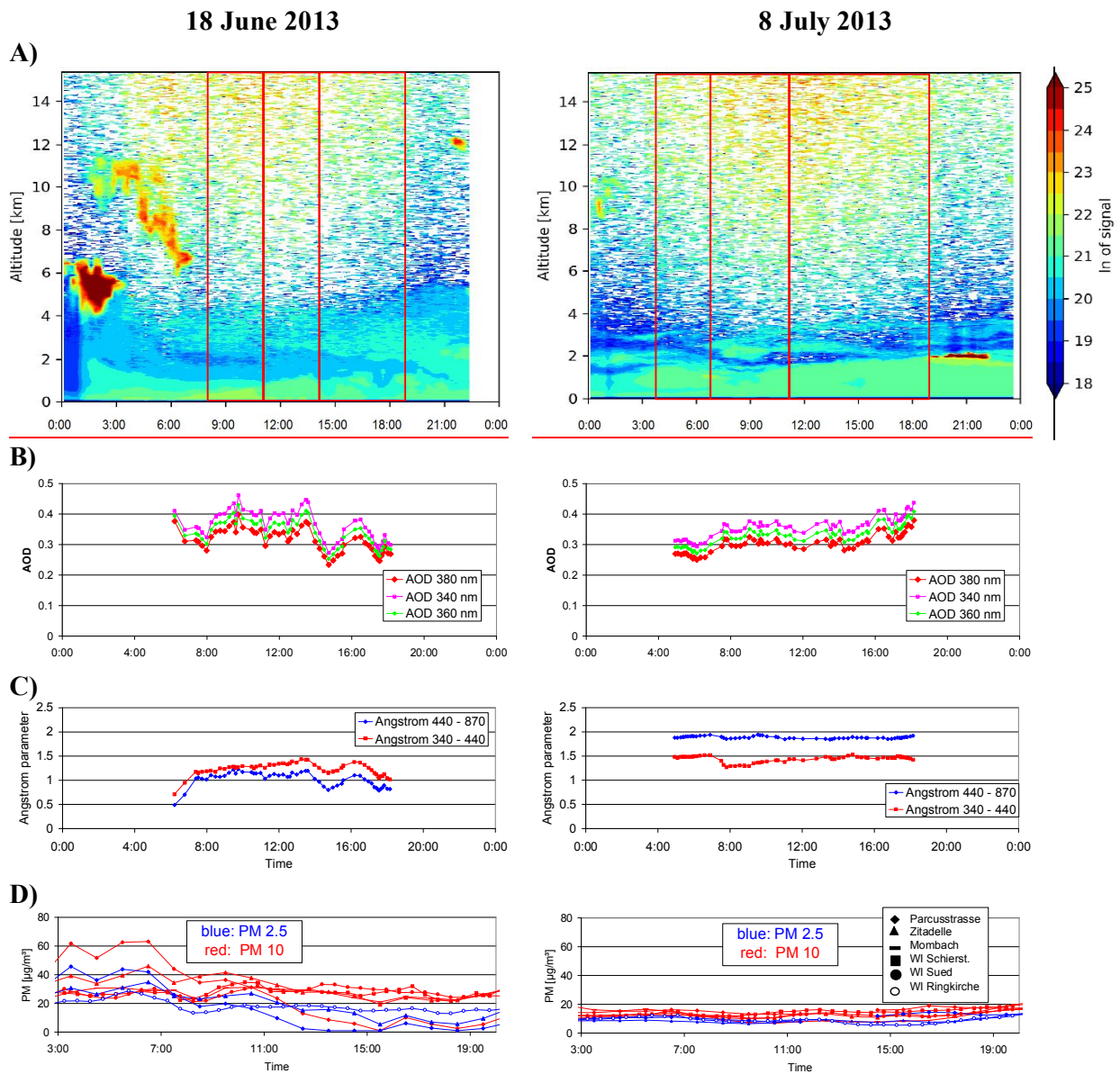
1655 Vlemmix, T., Hendrick, F., Pinardi, G., De Smedt, I., Fayt, C., Hermans, C., Piters, A., Wang,
1656 P., Levelt, P., and Van Roozendaal, M.: MAX-DOAS observations of aerosols, formaldehyde
1657 and nitrogen dioxide in the Beijing area: comparison of two profile retrieval approaches,
1658 *Atmos. Meas. Tech.*, 8, 941-963, <https://doi.org/10.5194/amt-8-941-2015>, 2015.

1659
1660 [Volkamer, R., Baidar, S., Campos, T. L., Coburn, S., DiGangi, J. P., Dix, B., Eloranta, E. W.,](#)
1661 [Koenig, T. K., Morley, B., Ortega, I., Pierce, B. R., Reeves, M., Sinreich, R., Wang, S.,](#)
1662 [Zondlo, M. A., and Romashkin, P. A.: Aircraft measurements of BrO, IO, glyoxal, NO₂, H₂O,](#)
1663 [O₂-O₂ and aerosol extinction profiles in the tropics: comparison with aircraft-/ship-based in](#)
1664 [situ and lidar measurements, *Atmos. Meas. Tech.*, 8, 2121-2148, 2015.](#)
1665
1666 Wagner, T., F. Erle, L. Marquard, C. Otten, K. Pfeilsticker, T. Senne, J. Stutz, and U. Platt,
1667 Cloudy sky optical paths as derived from differential optical absorption spectroscopy
1668 observations, *J. Geophys. Res.*, 103, 25307-25321, 1998.
1669
1670 Wagner, T., B. Dix, C.v. Friedeburg, U. Frieß, S. Sanghavi, R. Sinreich, and U. Platt MAX-
1671 DOAS O₄ measurements – a new technique to derive information on atmospheric aerosols.
1672 (I) Principles and information content, *J. Geophys. Res.*, 109, doi: 10.1029/2004JD004904,
1673 2004.
1674
1675 Wagner, T., J. P. Burrows, T. Deutschmann, B. Dix, C. von Friedeburg, U. Frieß, F.
1676 Hendrick, K.-P. Heue, H. Irie, H. Iwabuchi, Y. Kanaya, J. Keller, C. A. McLinden, H. Oetjen,
1677 E. Palazzi, A. Petritoli, U. Platt, O. Postlyakov, J. Pukite, A. Richter, M. van Roozendaal, A.
1678 Rozanov, V. Rozanov, R. Sinreich, S. Sanghavi, F. Wittrock, Comparison of Box-Air-Mass-
1679 Factors and Radiances for Multiple-Axis Differential Optical Absorption Spectroscopy
1680 (MAX-DOAS) Geometries calculated from different UV/visible Radiative Transfer Models,
1681 *Atmos. Chem. Phys.*, 7, 1809-1833, 2007.
1682
1683 Wagner, T., Deutschmann, T., and Platt, U.: Determination of aerosol properties from MAX-
1684 DOAS observations of the Ring effect, *Atmos. Meas. Tech.*, 2, 495-512, 2009.
1685
1686 Wagner, T., Beirle, S., Deutschmann, T., and Penning de Vries, M.: A sensitivity analysis of
1687 Ring effect to aerosol properties and comparison to satellite observations, *Atmos. Meas.*
1688 *Tech.*, 3, 1723-1751, doi:10.5194/amt-3-1723-2010, 2010.
1689
1690 Wang, T., Hendrick, F., Wang, P., Tang, G., Clémer, K., Yu, H., Fayt, C., Hermans, C.,
1691 Gielen, C., Müller, J.-F., Pinardi, G., Theys, N., Brenot, H., and Van Roozendaal, M.:
1692 Evaluation of tropospheric SO₂ retrieved from MAX-DOAS measurements in Xianghe,
1693 China, *Atmos. Chem. Phys.*, 14, 11149-11164, <https://doi.org/10.5194/acp-14-11149-2014>,
1694 2014.
1695
1696 Wang, S., Cuevas, C. A., Frieß, U., and Saiz-Lopez, A.: MAX-DOAS retrieval of aerosol
1697 extinction properties in Madrid, Spain, *Atmos. Meas. Tech.*, 9, 5089-5101,
1698 <https://doi.org/10.5194/amt-9-5089-2016>, 2016.
1699
1700 Wang, Y., Beirle, S., Lampel, J., Koukouli, M., De Smedt, I., Theys, N., Li, A., Wu, D., Xie,
1701 P., Liu, C., Van Roozendaal, M., Stavrou, T., Müller, J.-F., and Wagner, T.: Validation of
1702 OMI, GOME-2A and GOME-2B tropospheric NO₂, SO₂ and HCHO products using MAX-
1703 DOAS observations from 2011 to 2014 in Wuxi, China: investigation of the effects of priori
1704 profiles and aerosols on the satellite products, *Atmos. Chem. Phys.*, 17, 5007-5033,
1705 <https://doi.org/10.5194/acp-17-5007-2017>, 2017a.
1706
1707 Wang, Y., Lampel, J., Xie, P., Beirle, S., Li, A., Wu, D., and Wagner, T.: Ground-based
1708 MAX-DOAS observations of tropospheric aerosols, NO₂, SO₂ and HCHO in Wuxi, China,

1709 from 2011 to 2014, *Atmos. Chem. Phys.*, 17, 2189–2215, doi:10.5194/acp-17-2189-2017,
1710 2017b.
1711
1712 Wang, Y., Beirle, S., Hendrick, F., Hilboll, A., Jin, J., Kyuberis, A. A., Lampel, J., Li, A.,
1713 Luo, Y., Lodi, L., Ma, J., Navarro, M., Ortega, I., Peters, E., Polyansky, O. L., Remmers, J.,
1714 Richter, A., Puentedura, O., Van Roozendael, M., Seyler, A., Tennyson, J., Volkamer, R.,
1715 Xie, P., Zobov, N. F., and Wagner, T.: MAX-DOAS measurements of HONO slant column
1716 densities during the MAD-CAT campaign: inter-comparison, sensitivity studies on spectral
1717 analysis settings, and error budget, *Atmos. Meas. Tech.*, 10, 3719-3742,
1718 <https://doi.org/10.5194/amt-10-3719-2017>, 2017c.
1719
1720 Wiegner, M. and Geiß, A.: Aerosol profiling with the Jenoptik ceilometer CHM15kx, *Atmos.*
1721 *Meas. Tech.*, 5, 1953-1964, <https://doi.org/10.5194/amt-5-1953-2012>, 2012.
1722
1723 Winterrath, T., T. P. Kurosu, A. Richter and J. P. Burrows, Enhanced O₃ and NO₂ in
1724 thunderstorm clouds: convection or production?, *Geophys. Res. Lett.*, No. 26, pp. 1291-1294,
1725 1999.
1726
1727 Wittrock, F., H. Oetjen, A. Richter, S. Fietkau, T. Medeke, A. Rozanov, J. P. Burrows
1728 MAX-DOAS measurements of atmospheric trace gases in Ny-Ålesund - Radiative transfer
1729 studies and their application, *Atmos. Chem. Phys.*, 4, 955-966, 2004
1730
1731 Zieger, P., Weingartner, E., Henzing, J., Moerman, M., de Leeuw, G., Mikkilä, J., Ehn, M.,
1732 Petäjä, T., Clémer, K., van Roozendael, M., Yilmaz, S., Frieß, U., Irie, H., Wagner, T.,
1733 Shaiganfar, R., Beirle, S., Apituley, A., Wilson, K., and Baltensperger, U.: Comparison of
1734 ambient aerosol extinction coefficients obtained from in-situ, MAX-DOAS and LIDAR
1735 measurements at Cabauw, *Atmos. Chem. Phys.*, 11, 2603-2624, [https://doi.org/10.5194/acp-](https://doi.org/10.5194/acp-11-2603-2011)
1736 [11-2603-2011](https://doi.org/10.5194/acp-11-2603-2011), 2011.
1737
1738
1739
1740
1741
1742
1743
1744
1745
1746
1747
1748
1749
1750
1751
1752
1753
1754
1755
1756
1757
1758
1759

1760
1761
1762
1763

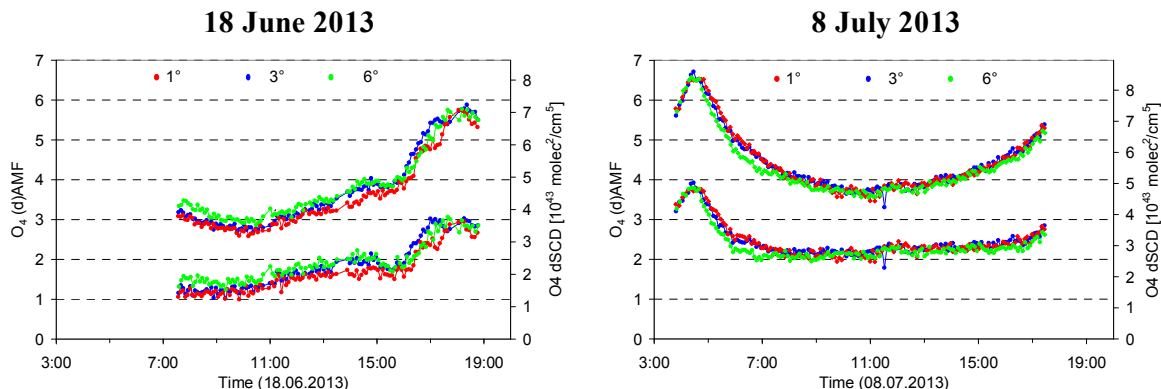
Figures



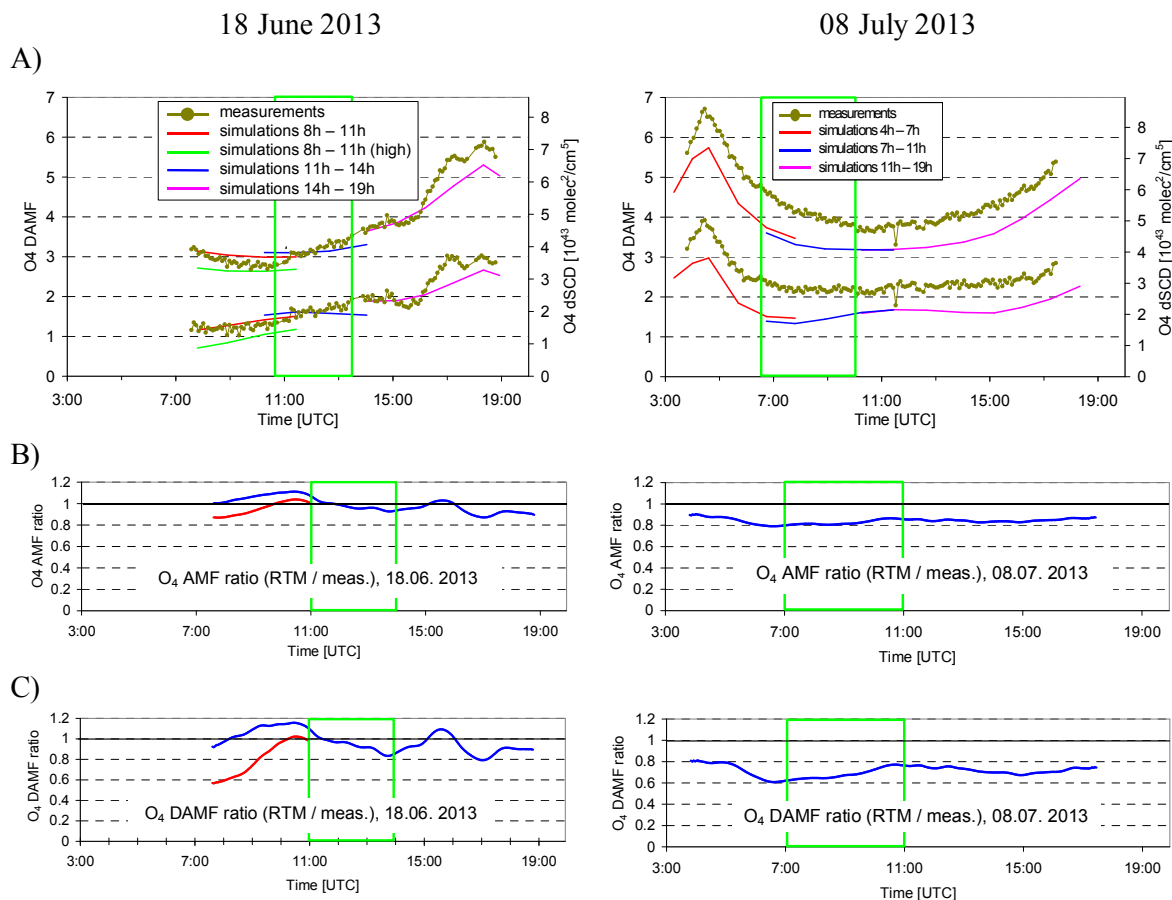
1764 Fig. 1 Various aerosol properties on the two selected days (left: 18 June 2013; right: 8 July
1765 2013). A) Aerosol backscatter profiles from ceilometer measurements; B) AOD at 340, 360,
1766 and 380 nm (360 values are interpolated from 340 and 380 nm) from AERONET sun
1767 photometer measurements; C) Ångström parameters for two wavelength pairs (340 – 440 nm
1768 and 440 – 870 nm) from AERONET sun photometer measurements; D) Surface in situ
1769 measurements of PM_{2.5} and PM₁₀ measured at different air quality monitoring stations in
1770 Mainz and the nearby city of Wiesbaden .

1771
1772
1773
1774
1775

1776
1777
1778

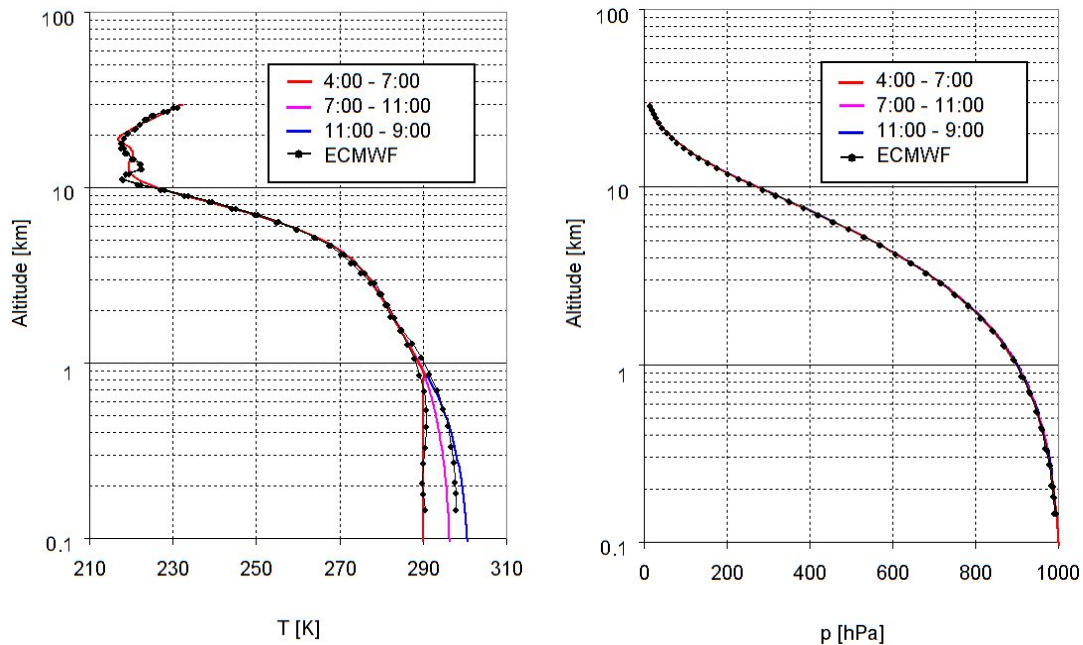


1779 Fig. 2 O₄ AMFs (upper lines) and dAMFs (lower lines) for 1°, 3°, and 6° elevation angles
1780 derived from the MPIC MAX-DOAS measurements on the two selected days. Interestingly,
1781 on 18 June the lowest values are in general found for the lowest elevation angles, which is an
1782 indication for the high aerosol load close to the surface. The y-axis on the right side shows the
1783 corresponding O₄ (d)SCDs for O₄ VCDs of $1.23 \cdot 10^{43} \text{ molec}^2/\text{cm}^5$ and of $1.28 \cdot 10^{43}$
1784 $\text{molec}^2/\text{cm}^5$ for 18 June and 08 July, respectively (see section 4.1.2).
1785
1786



1787 Fig. 3 A) Comparison of O₄ (d)AMFs from MAX-DOAS measurements and forward model
1788 simulations for the two selected days. The green rectangle indicates the middle periods on
1789 both days, which are the focus of the quantitative comparison. The green line on 18 June

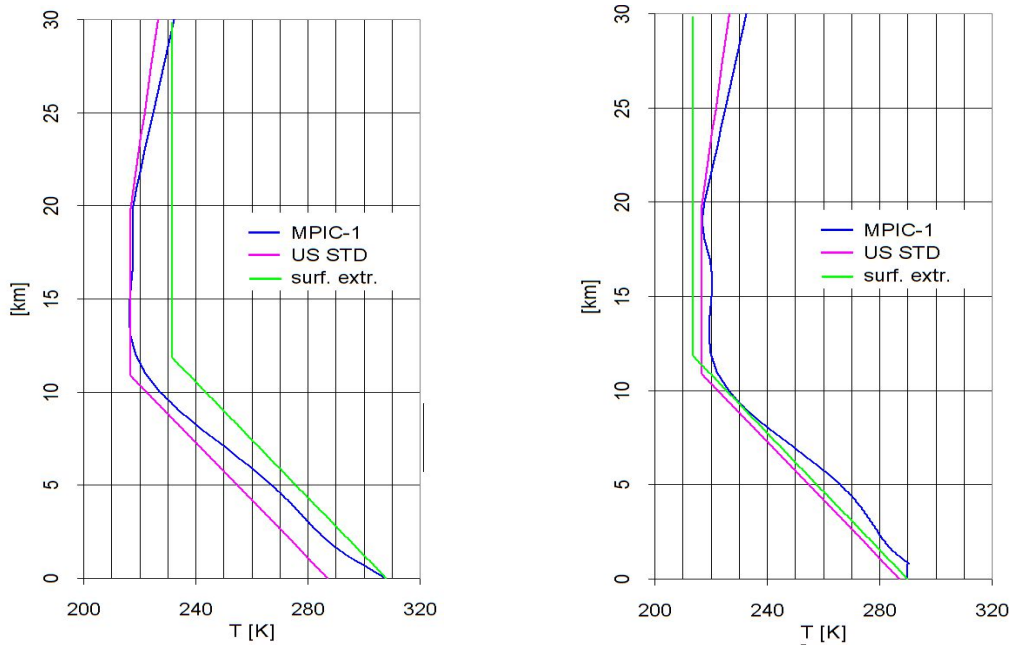
1790 represents forward model results for a modified aerosol profile (see text). The y-axis on the
 1791 right side shows the corresponding O₄ (d)SCDs for O₄ VCDs of $1.23 \cdot 10^{43}$ molec²/cm⁵ and of
 1792 $1.28 \cdot 10^{43}$ molec²/cm⁵ for 18 June and 08 July, respectively (see section 4.1.2). In B) and C)
 1793 the ratios of the simulated and measured AMFs and dAMFs are shown, respectively. The red
 1794 line on 18 June represents the ratios for the modified aerosol scenario.
 1795



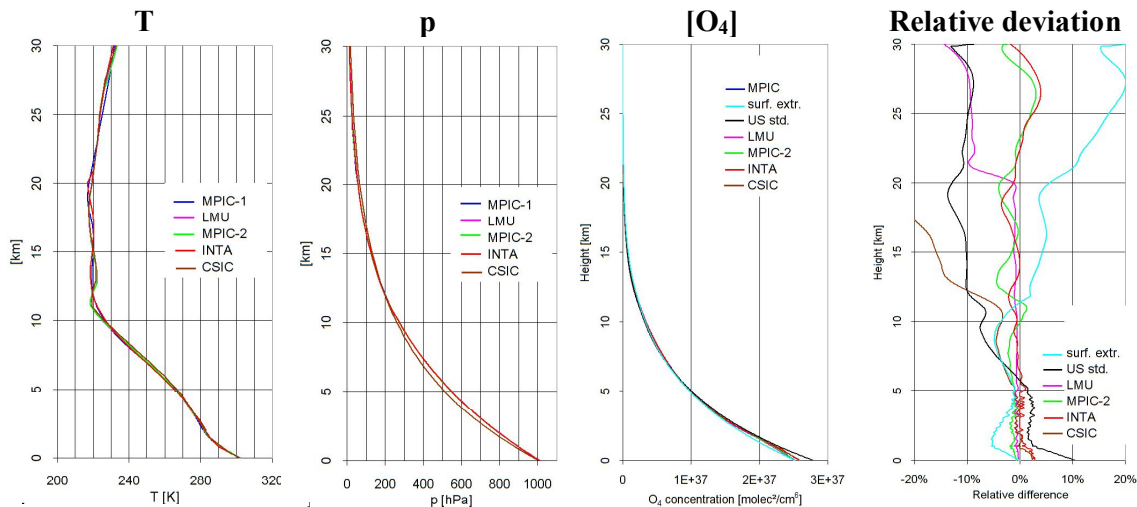
1796 Fig. 4 Extracted temperature (left) and pressure (right) profiles for the three periods on 8 July
 1797 2013. Also shown are ECMWF profiles above Mainz for 6:00 and 18:00. To better account
 1798 for the diurnal variation of the temperatures near the surface, below 1 km the temperature is
 1799 linearly interpolated between the surface measurements and the ECMWF temperatures at 1
 1800 km (for details see text). Note that the altitude is given relative to the height of the
 1801 measurement site (150 m).
 1802

18 June 14:00 – 19:00

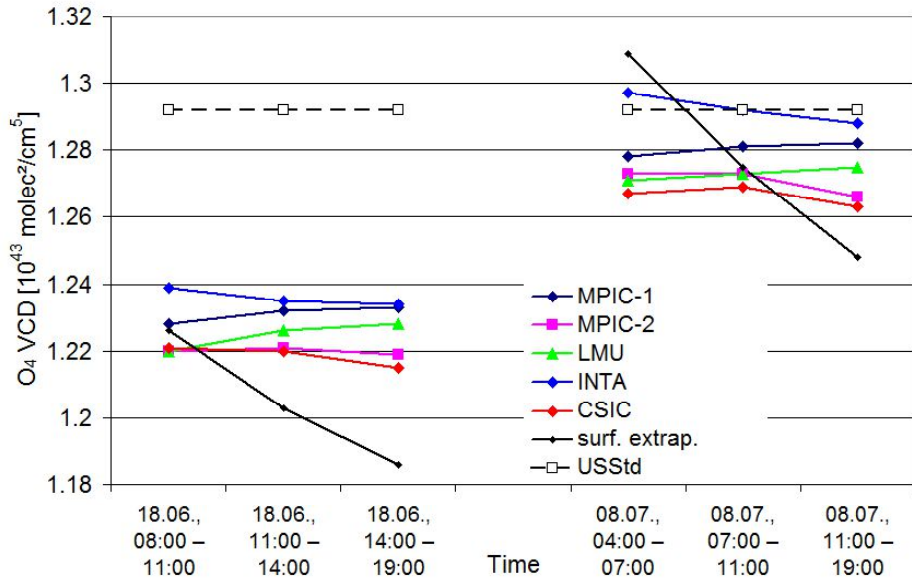
8 July 4:00 – 7:00



1803 Fig. 5 Temperature profiles extracted in different ways for two periods (Left: 18 June 14:00 –
 1804 19:00; right: 8 July 4:00 – 7:00). The blue profiles are extracted from in situ measurements and ECMWF profiles as described in the text. The green profiles are extracted from the
 1805 surface temperatures and assuming a constant lapse rate of $-6.5\text{K} / \text{km}$ up to 12 km and a
 1806 constant temperature above. The pink curves represent the temperature profile from the US
 1807 standard atmosphere.
 1808
 1809



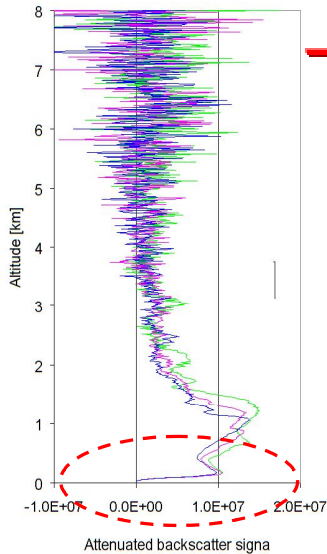
1810 Fig. 6 Comparison of the vertical profiles of temperature, pressure and O_4 concentration
 1811 (expressed as the square of the O_2 concentration) for 8 July, 11:00 – 19 :00, extracted by the
 1812 different groups. In the right figure the relative deviations of the O_4 concentration compared
 1813 to the MPIC standard extraction are shown. There, also the profiles derived from the
 1814 extrapolation from the surface values and the US standard atmosphere are included.
 1815
 1816



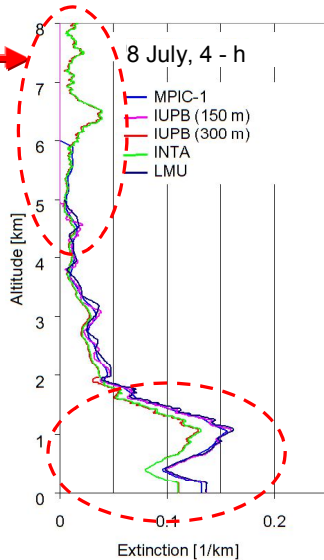
1817
1818
1819
1820
1821
1822
1823
1824
1825
1826
1827
1828
1829

Fig. 7 Comparison of the O₄ VCDs for the selected periods on both days calculated from the profiles extracted by the different groups. Also the results for the profiles extrapolated from the surface values and the US standard atmosphere are shown.

Ceilometer backscatter profiles at 1064 nm (hourly averages)



Extinction profiles at 360 nm derived by different groups



The backscatter profiles are converted into extinction profiles by scaling with the AOD from the sun photometer.

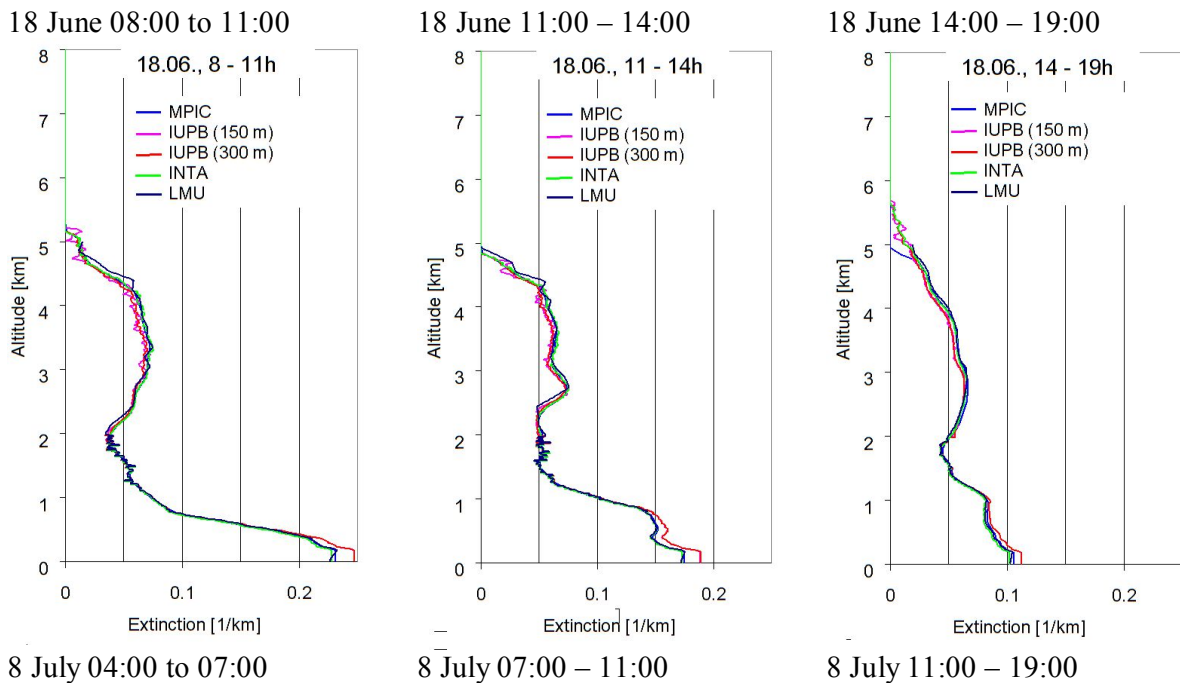
The self attenuation of the aerosol is accounted for.

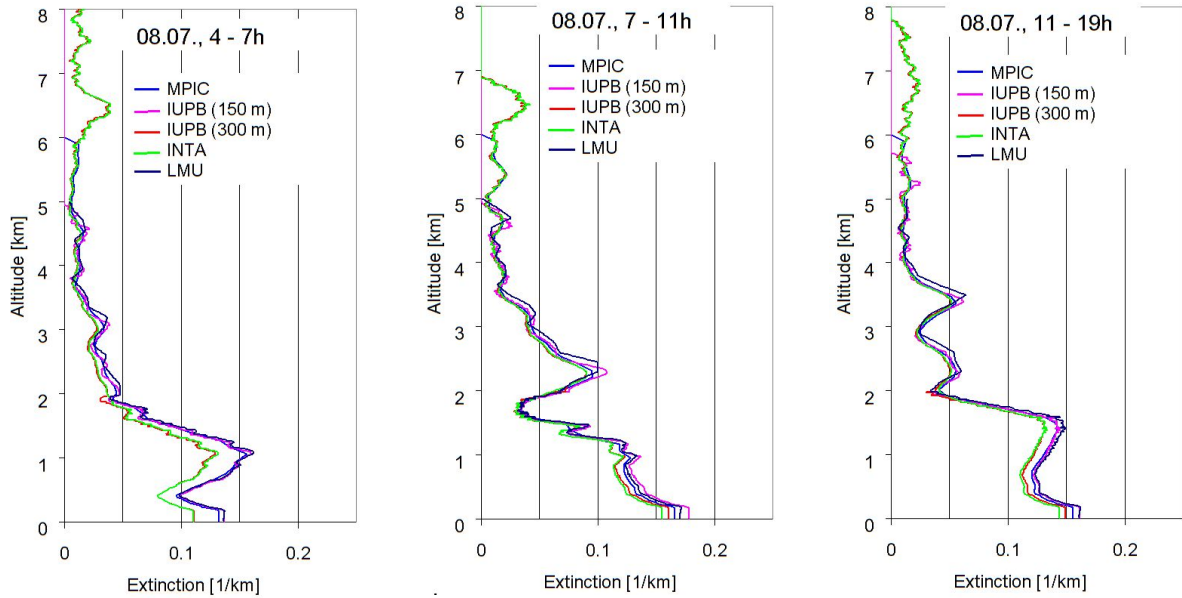
Below 180m, the profiles are extrapolated (constant value, or constant or double slope).

1830
1831
1832

Fig. 8 Left: Hourly averaged backscatter profiles from the ceilometer measurements for the period 4:00 – 7:00 on 8 July 2013. Below 180 m the values rapidly decrease to zero due to the

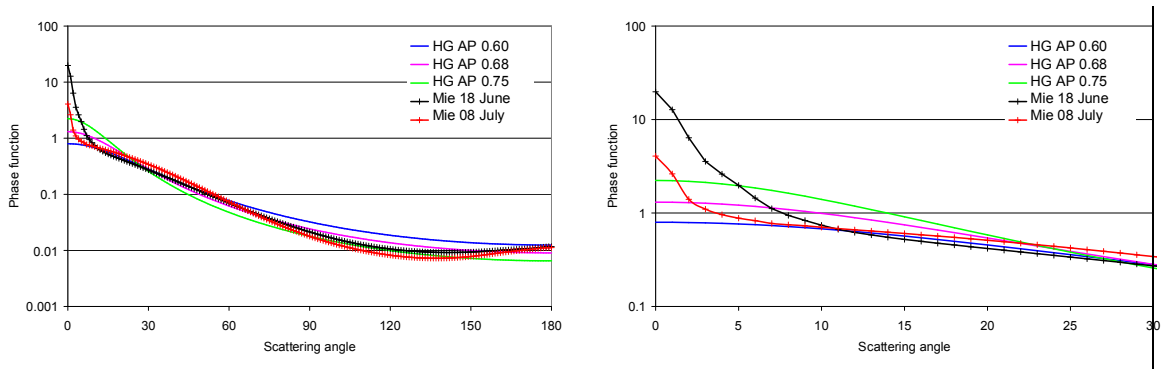
1833 missing overlap between the outgoing beam and the field of view of the telescope. Right:
 1834 Aerosol extinction profiles extracted by the different groups from the ceilometer profiles
 1835 (assuming a constant extinction below 180 m). The red circles indicate the height intervals
 1836 with the largest deviations (IUPB 150 m and IUPB 300 m indicate profile extractions with
 1837 different widths of the smoothing kernels: Hanning windows of 150 and 300 m, respectively).
 1838
 1839
 1840
 1841
 1842
 1843
 1844
 1845
 1846
 1847
 1848
 1849
 1850
 1851
 1852
 1853
 1854
 1855
 1856
 1857
 1858
 1859
 1860
 1861
 1862





1863 Fig. 9 Comparison of the aerosol extinction profiles extracted by the different groups for all
 1864 three periods on both days.
 1865

1866
 1867
 1868
 1869
 1870
 1871
 1872
 1873
 1874
 1875
 1876



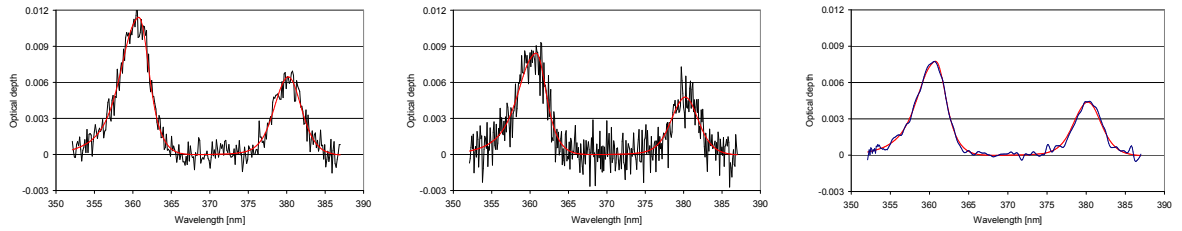
1877 Fig. 10 Comparison of different aerosol phase functions used in the radiative transfer
 1878 simulations. The right figure is a zoom of the left figure.
 1879

1880
 1881
 1882

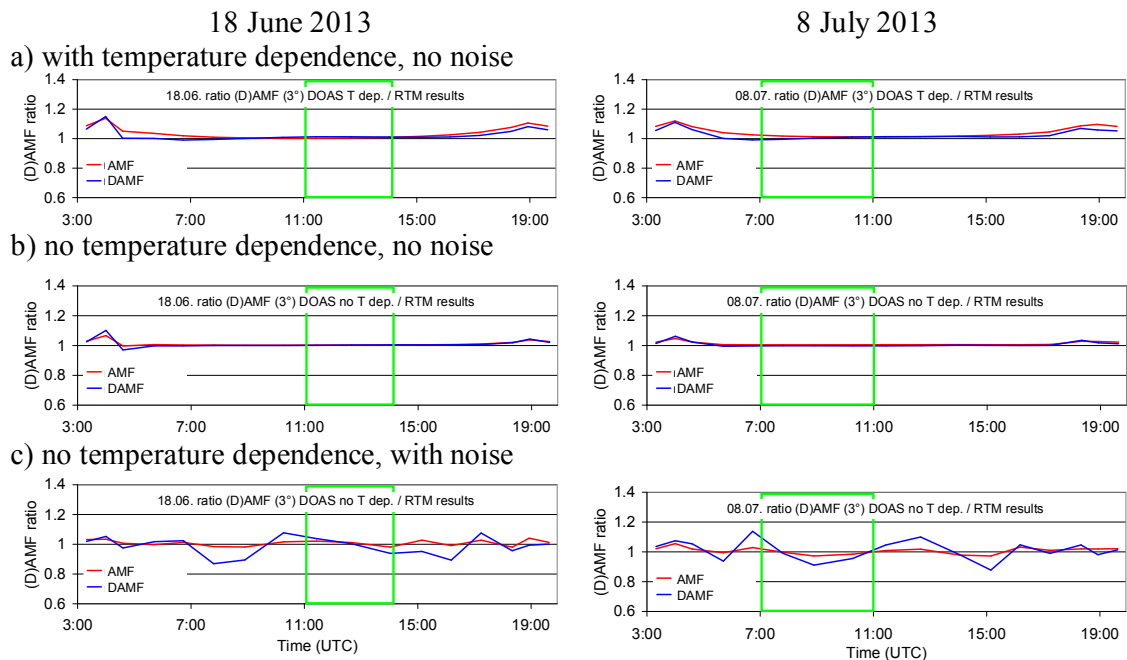
Real measurements
 $2.71 \cdot 10^{43} \text{ molec}^2/\text{cm}^5$

Synthetic spectra with noise
 $2.00 \cdot 10^{43} \text{ molec}^2/\text{cm}^5$

Synthetic spectra without noise
 $1.84 \cdot 10^{43} \text{ molec}^2/\text{cm}^5$

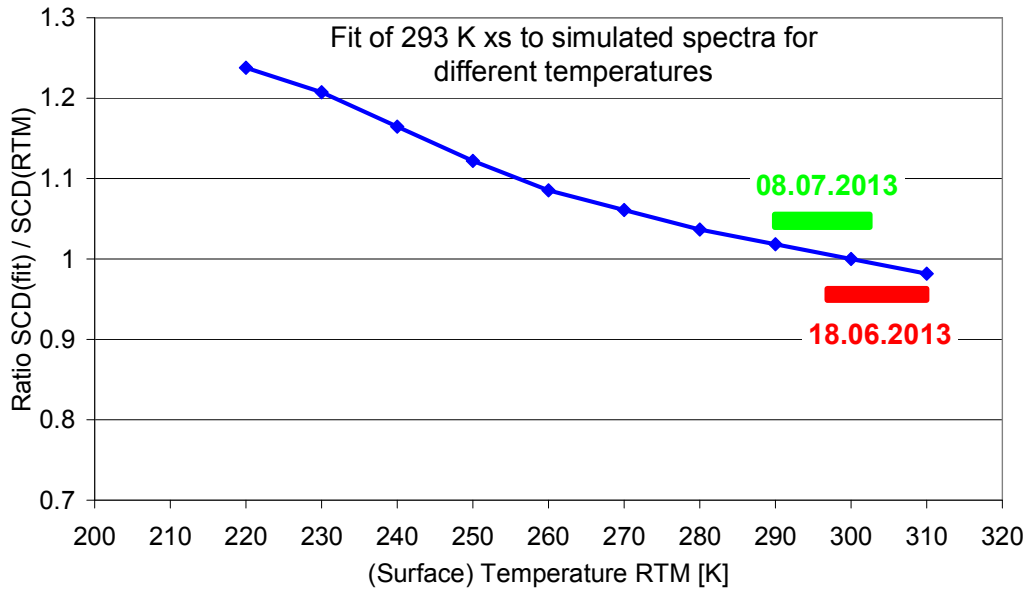


1883 Fig. 11 Spectral analysis results for a real measurement from the MPIC instrument (left) and a
 1884 synthetic spectrum with and without noise. Spectra are taken from 8 July 2013 at 11:26
 1885 (elevation angle = 1°). The derived O₄ dSCD is shown above the individual plots.
 1886
 1887
 1888
 1889
 1890
 1891
 1892
 1893
 1894
 1895
 1896
 1897
 1898
 1899
 1900
 1901
 1902
 1903
 1904
 1905
 1906



1907
1908
1909
1910
1911
1912
1913

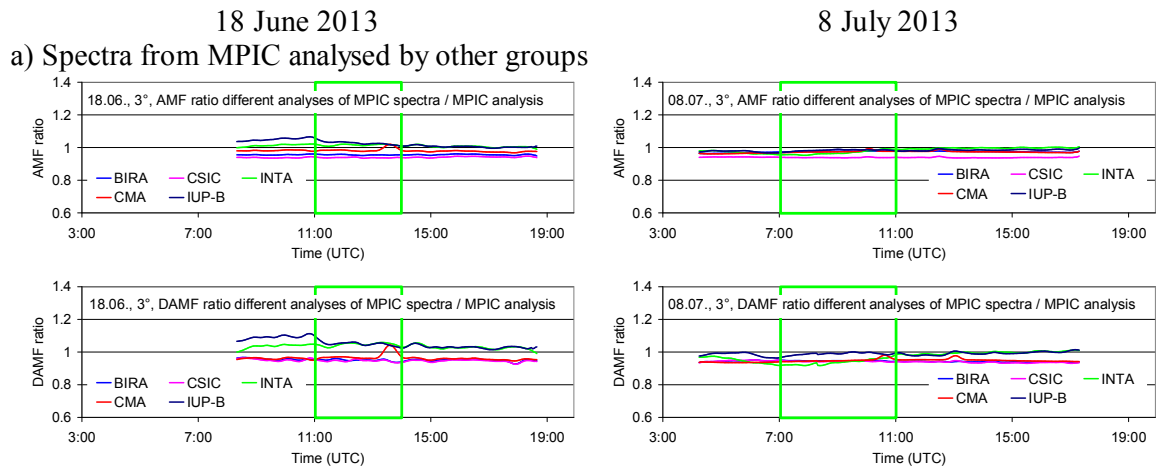
Fig. 12 Ratio of the O₄ (d)AMFs derived from synthetic spectra versus those obtained from radiative transfer simulations at 360 nm for both selected days.



1914
1915
1916
1917
1918
1919
1920
1921
1922
1923
1924

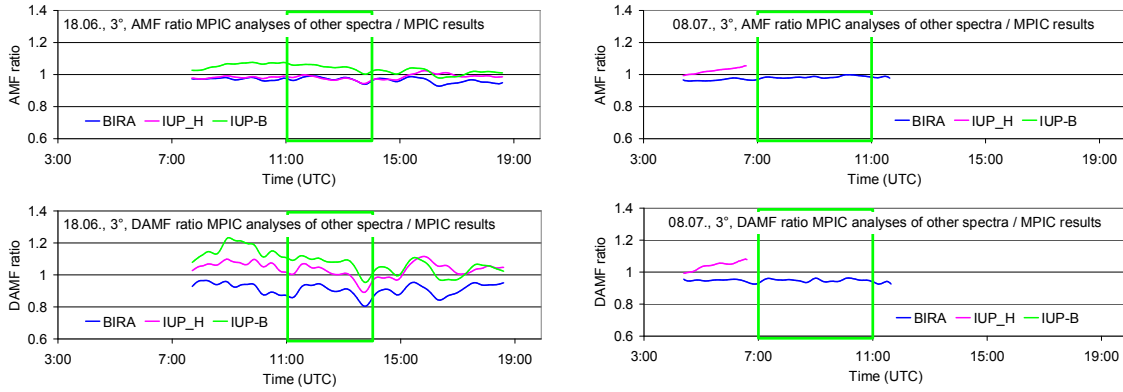
Fig. 13 Ratio of the O₄ dAMF obtained from simulated spectra for different surface temperatures by the corresponding O₄ dAMFs derived from radiative transfer simulations. The results represent MAX-DOAS observations at low elevation angles (2° to 3°).

1925



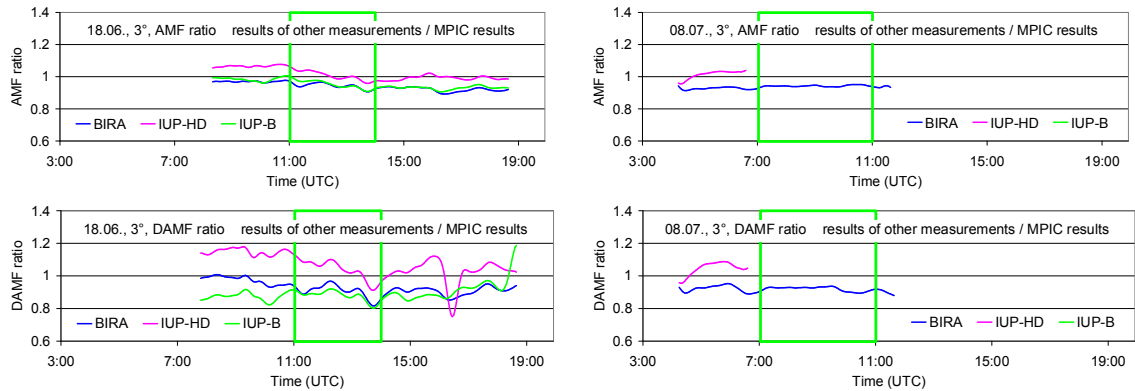
1926
1927

b) Spectra from other groups analysed by MPIC (all analyses for 335 – 374 nm)



1928
1929

c) Spectra from other groups analysed by the same groups

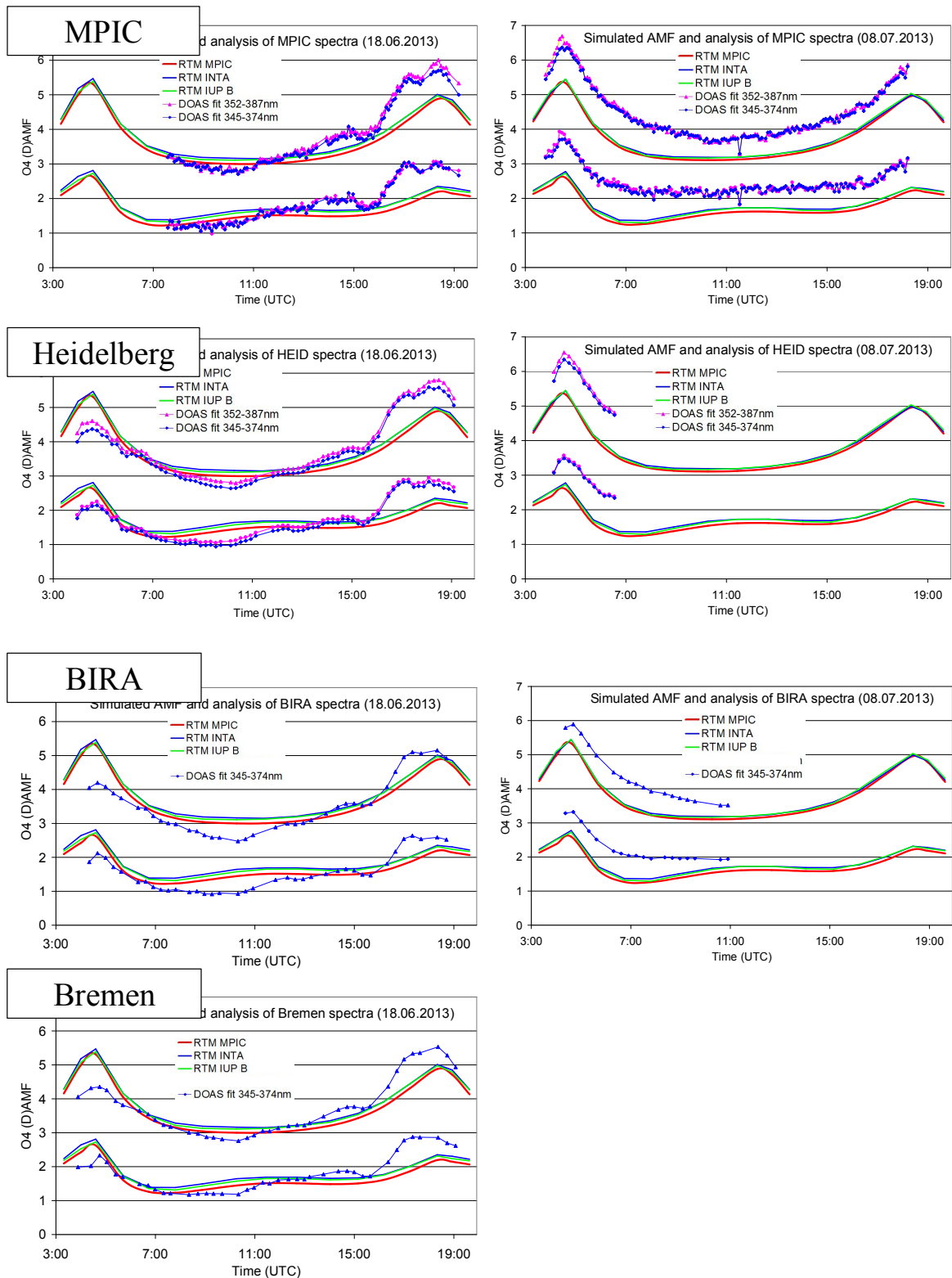


1930
1931
1932
1933
1934
1935
1936
1937
1938
1939
1940

Fig. 14 a) Ratio of the O₄ (d)AMFs derived from MPIC spectra when analysed by other groups versus those analysed by MPIC for both selected days; b) Ratio of the O₄ (d)AMFs derived from spectra measured and analysed by other groups (using different wavelength ranges and settings) versus those for the MPIC instrument analysed by MPIC; c) Ratio of the O₄ (d)AMFs derived from spectra measured by other groups but analysed by MPIC versus those for the MPIC instrument analysed by MPIC (using the spectral range 335 – 374 nm for all instruments).

18 June 2013

8 July 2013



1941

1942
 1943
 1944
 1945
 1946
 1947

Fig. 15 Comparison of measured and simulated O₄ (d)AMFs for both selected days. Measurements are from 4 different instruments, but analysed by MPIC using the standard settings (see Table 7). Simulations are performed by three different groups using Mie phase functions and otherwise the standard settings (see Table 6).

1948 **Appendix A1 Settings used for the simulation of synthetic spectra**

1949

1950

1951 Table A1 Vertical resolution used in radiative transfer simulations for different altitude
1952 ranges.

Lower boundary [km]	Upper boundary [km]	Vertical resolution [km]
0	0.5	0.02
0.5	2	0.1
2	12	0.2
12	25	1
25	45	2
45	100	5
100	1000	900

1953

1954

1955

1956

1957 Table A2 Dependence of SZA and relative azimuth angle on time (UTC) for the standard
1958 viewing direction (51° with respect to North).

Time (UTC)	SZA	RAZI
03:19	90	-0.1
04:00	85	7.7
04:36	80	14.2
05:42	70	26
06:44	60	37.5
07:48	50	50.1
08:54	40	66.2
10:16	30	94.6
11:26	26	129
12:40	30	163.3
14:02	40	191.8
15:09	50	207.9
16:11	60	220.5
17:14	70	232
18:20	80	243.8
18:56	85	250.3
19:38	90	258

1959

1960

1961

1962

1963

1964

1965

1966

1967

1968

1969

1970

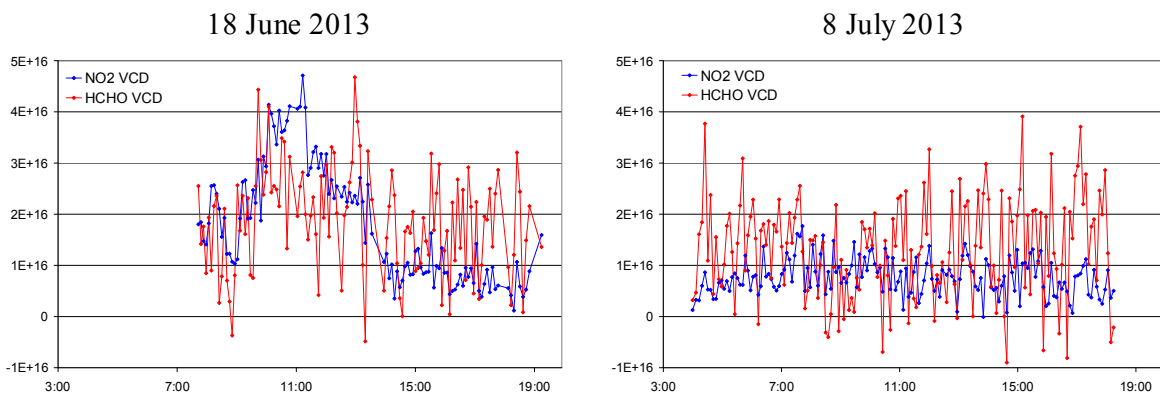
1971 Table A3 Trace gas profiles and cross sections used for the simulation of the synthetic
 1972 spectra.

Trace gas	Vertical profile	Cross section (reference and T)
O ₄	Derived from temperature and pressure profiles during. 18.06.: average profiles 11:00 – 14:00 08.07.: average profiles 7:00 – 11:00	Thalman and Volkamer (2013) (203, 223, 253, 273, 293 K)*
HCHO	18.06.: 0-1000m, constant concentration of $2 \cdot 10^{11}$ molec/cm ³ (about 8 ppb) 08.07.: 0-1000m, constant concentration of $1 \cdot 10^{11}$ molec/cm ³ (about 4 ppb)	Meller and Moortgat (2000) (298 K)
NO ₂	Troposphere 18.06.: 0-500m, constant concentration of $4 \cdot 10^{11}$ molec/cm ³ (about 16 ppb) 08.07.: 0-500m, constant concentration of $2 \cdot 10^{11}$ molec/cm ³ (about 8 ppb) Stratosphere: Gaussian profile with maximum at 25 km, and FWHM of 16 km, VCD = $5 \cdot 10^{15}$ molec/cm ²	Vandaele et al. (1997) (220, 294 K)
O ₃	Troposphere (0-8km): constant concentration $6 \cdot 10^{11}$ molec/cm ³ (about 24 ppb) Stratosphere: Gaussian profile with maximum at 22 km, and FWHM of 15 km, VCD = 314 DU	Serdyuchenko et al. (2014) (193 – 293 K in steps of 10 K)**

1973 *The temperature dependence is either considered or a constant temperature of 293 K is
 1974 assumed (see text for details).

1975 **The temperature dependence was parameterised according to Paur and Bass (1984).

1976
 1977
 1978
 1979
 1980
 1981

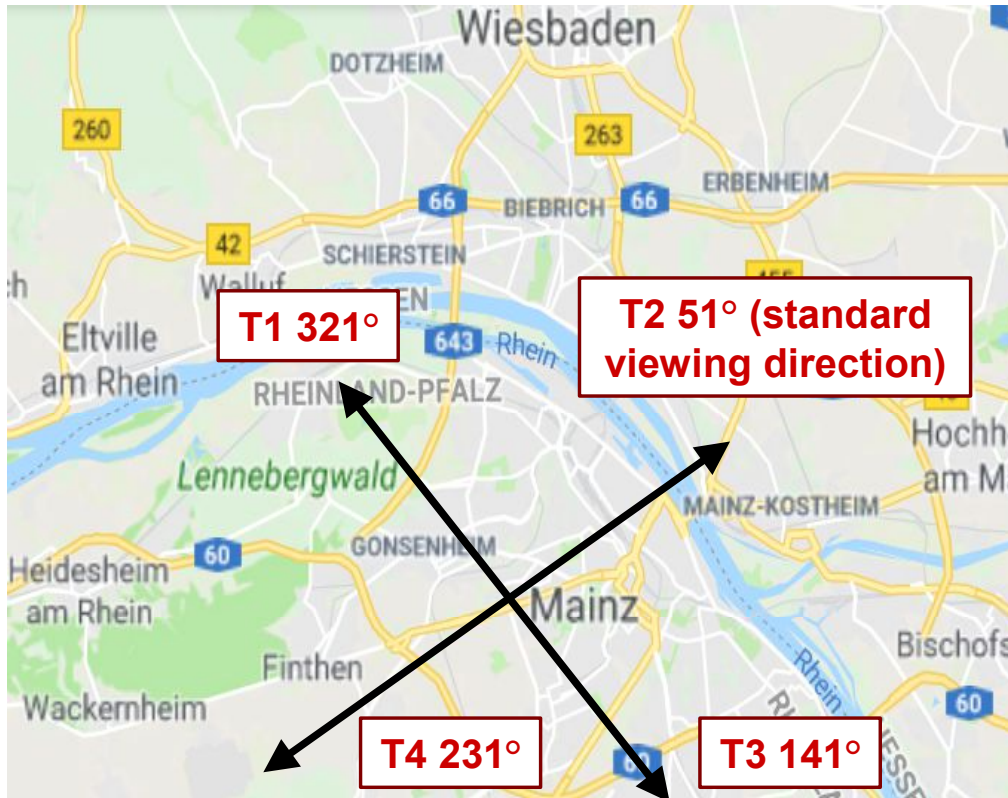


1982 Fig. A1 Tropospheric VCDs of NO₂ (blue) and HCHO (red) derived from measurements at
 1983 30° elevation using the geometric approximation.

1984
 1985

1986 **Appendix A2 Comparison of measured and simulated O₄ (d)AMFs for all azimuth and**
1987 **elevation angles of the MPIC MAX-DOAS measurements.**
1988

1989 The settings for the simulation of the synthetic spectra are given in Table 6 and Tables A1,
1990 A2, and A3 in appendix 1. Measurements are analysed using the standard settings (see Table
1991 7).
1992
1993

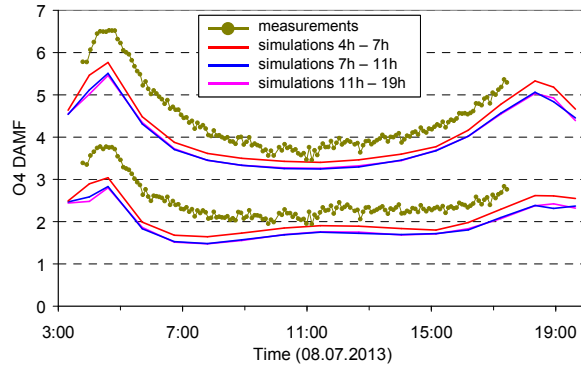


1994 Fig. A2 Azimuth viewing directions of the 4 telescopes (T1 to T4) of the MPIC MAX-DOAS
1995 instrument. The azimuth angles are defined with respect to North (map: © google maps).
1996
1997
1998

T1 North-West

For T1 and T4 azimuth direction, no measurements at 1° elevation were possible due to obstacles.

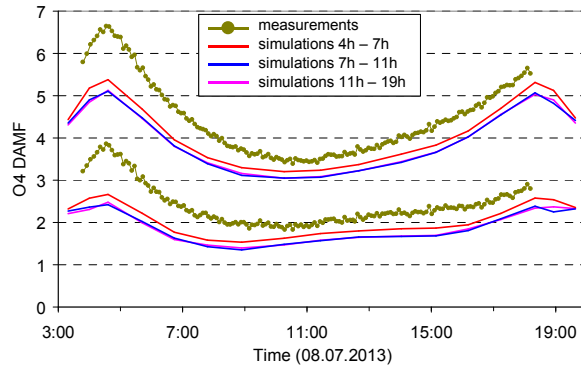
T2 North-East



T4 South-West

For T1 and T4 azimuth direction, no measurements at 1° elevation were possible due to obstacles.

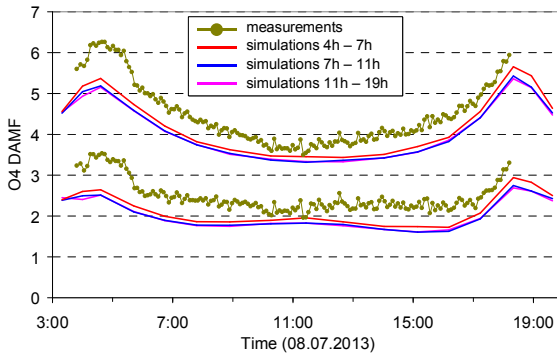
T3 South-East



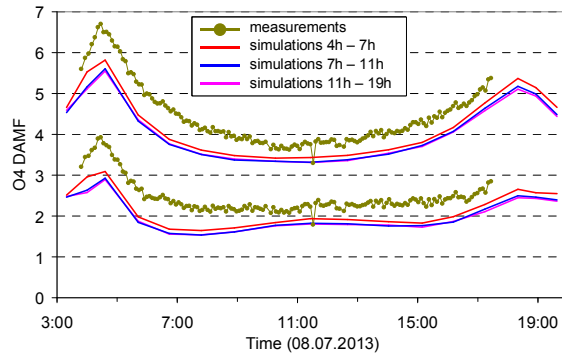
1999
2000
2001
2002

Fig. A3a Comparison results for 1° elevation angles on 8 July 2013. The upper lines indicate the O₄ AMFs, the lower lines the O₄ dAMFs (see also Fig. 2 and 3).

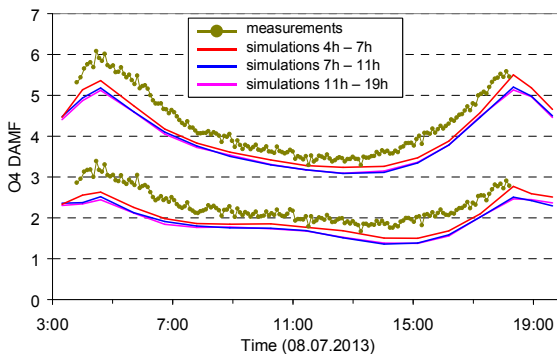
T1 North-West



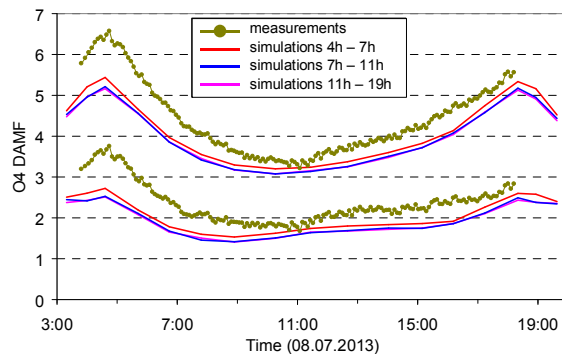
T2 North-East



T4 South-West



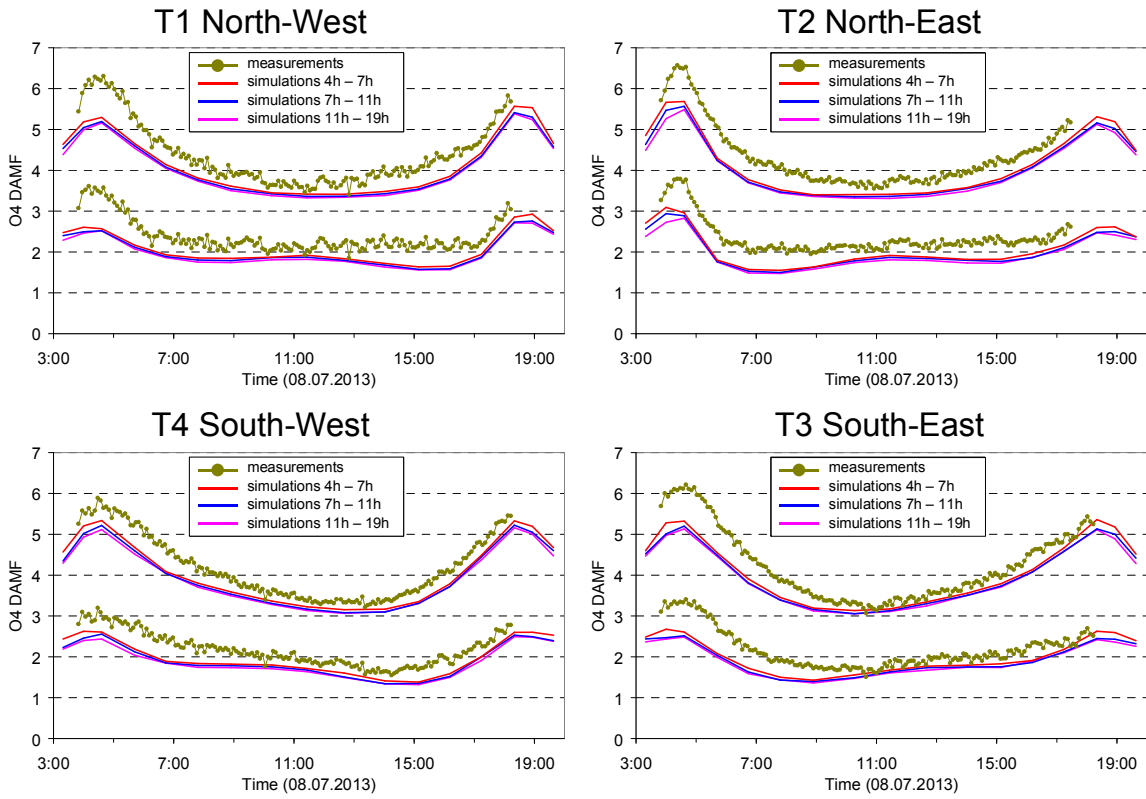
T3 South-East



2003
2004

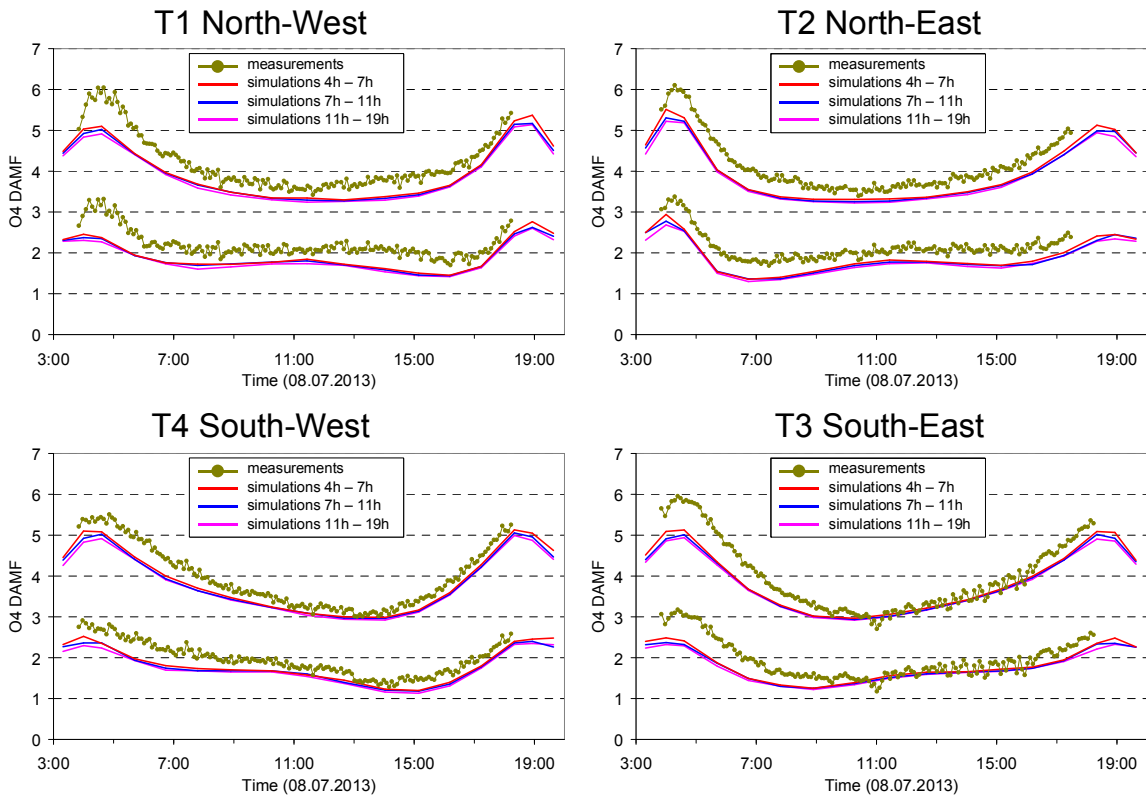
Fig. A3b Comparison results for 3° elevation angles on 8 July 2013.

2005



2006
2007
2008

Fig. A3c Comparison results for 6° elevation angles on 8 July 2013.



2009
2010
2011

Fig. A3d Comparison results for 10° elevation angles on 8 July 2013.

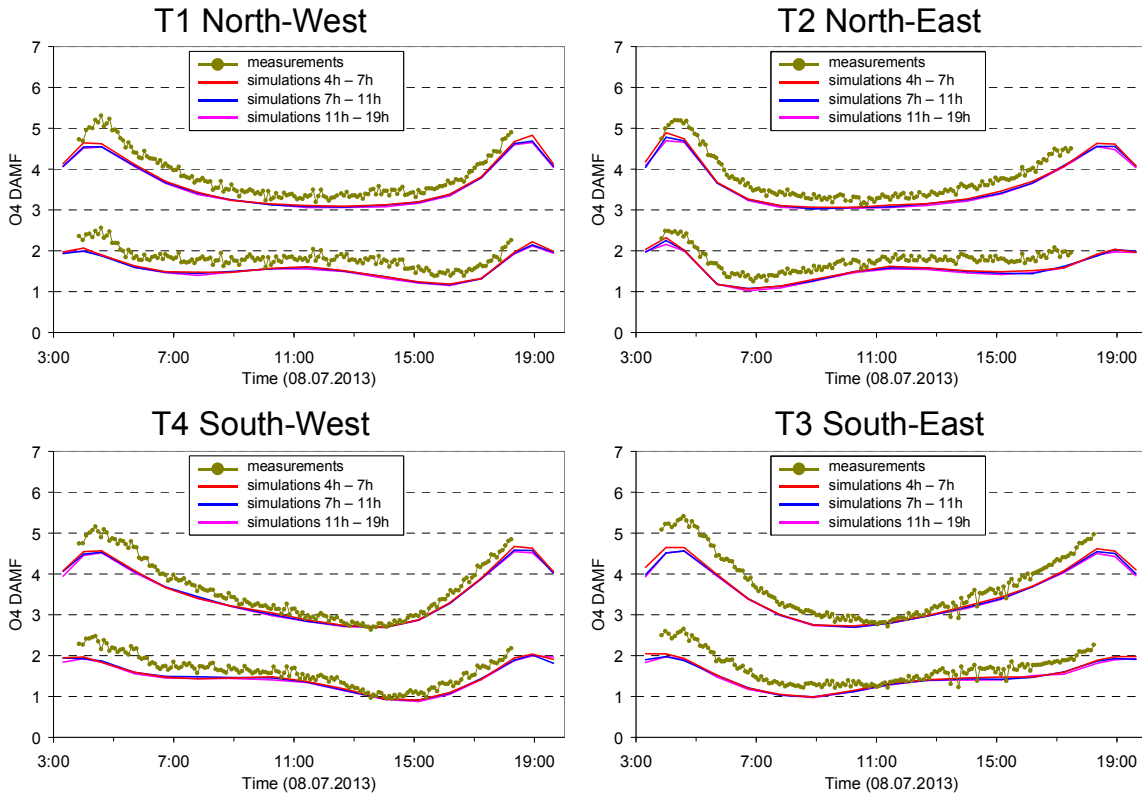


Fig. A3e Comparison results for 15° elevation angles on 8 July 2013.

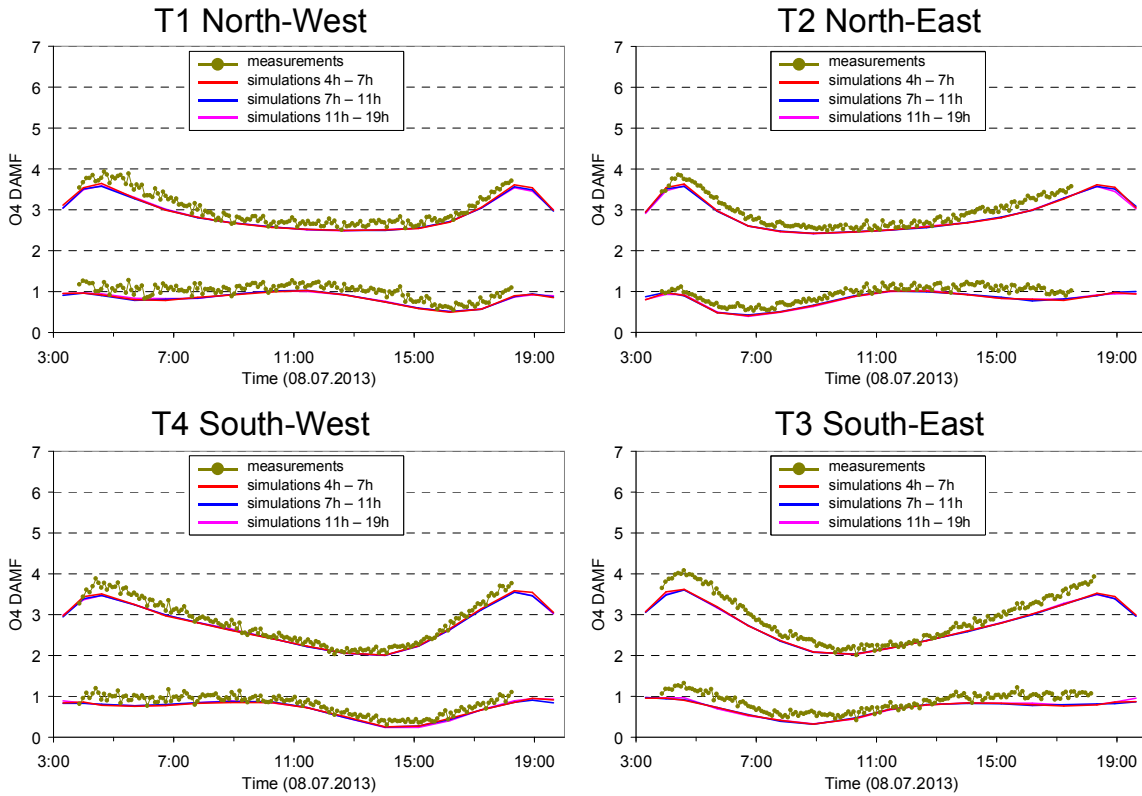


Fig. A3f Comparison results for 30° elevation angles on 8 July 2013.

2012
2013
2014

2015
2016
2017
2018

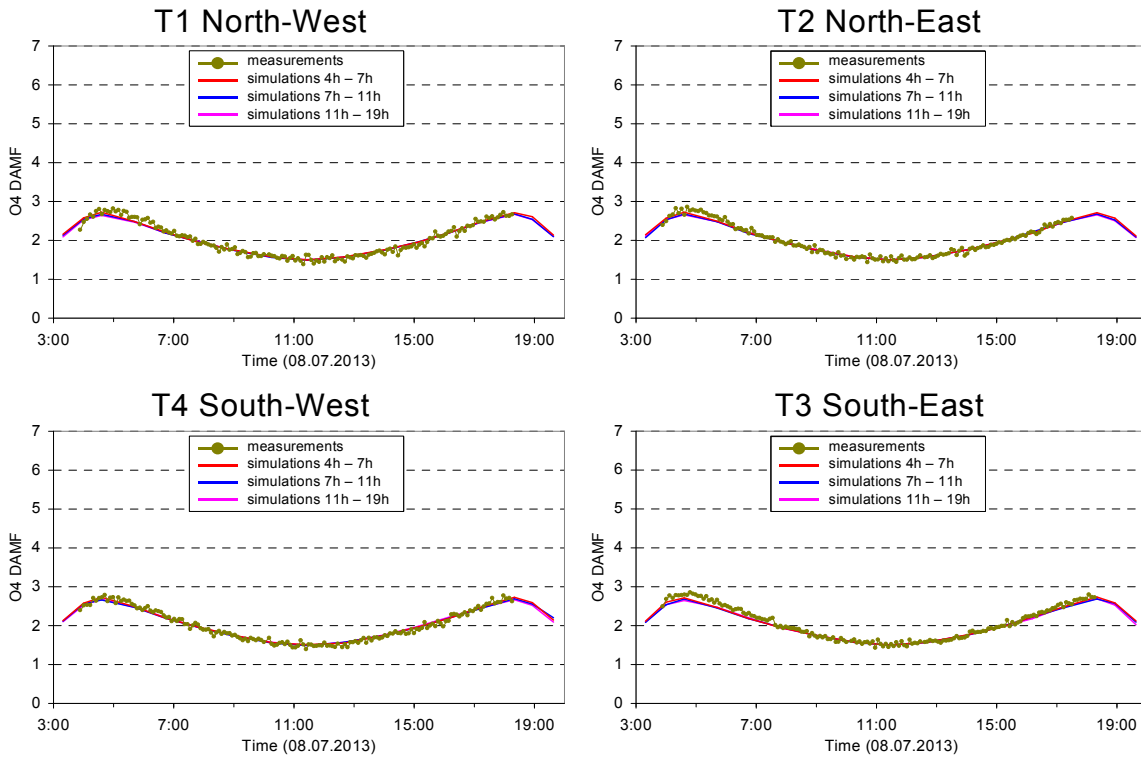
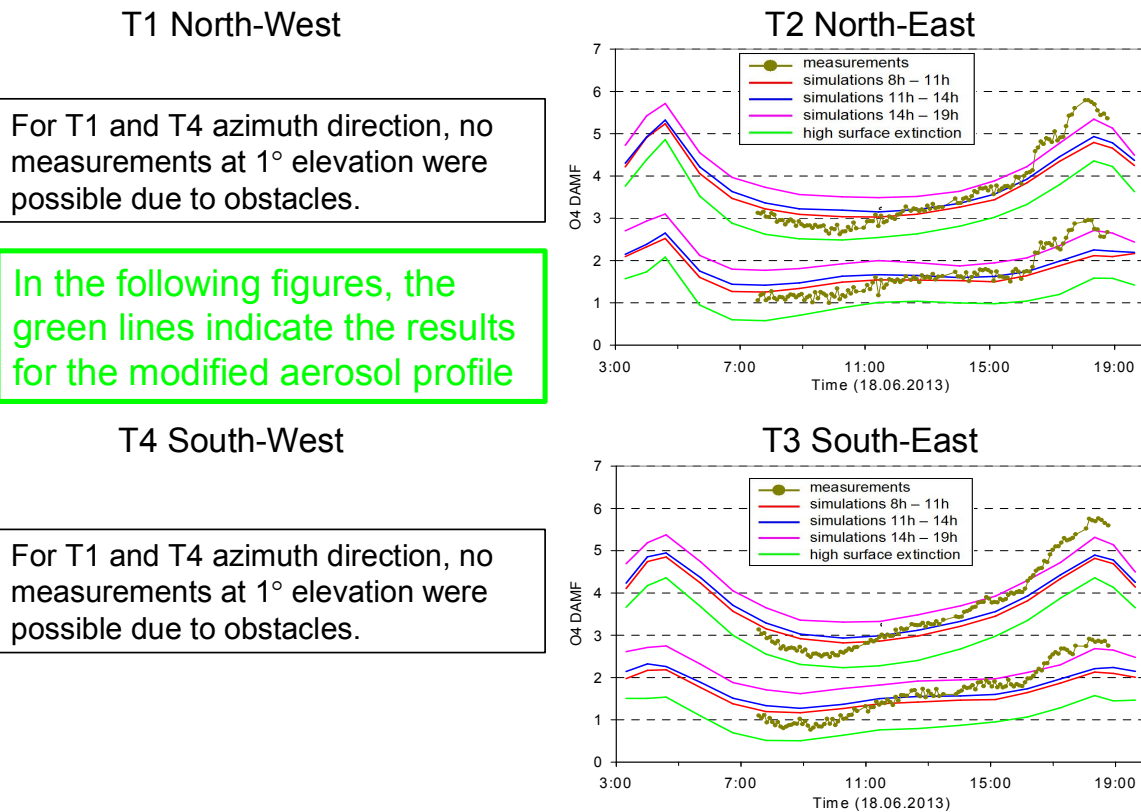


Fig. A3g Comparison results (only O₄ AMFs) for 90° elevation angles on 8 July 2013.

2019
2020
2021



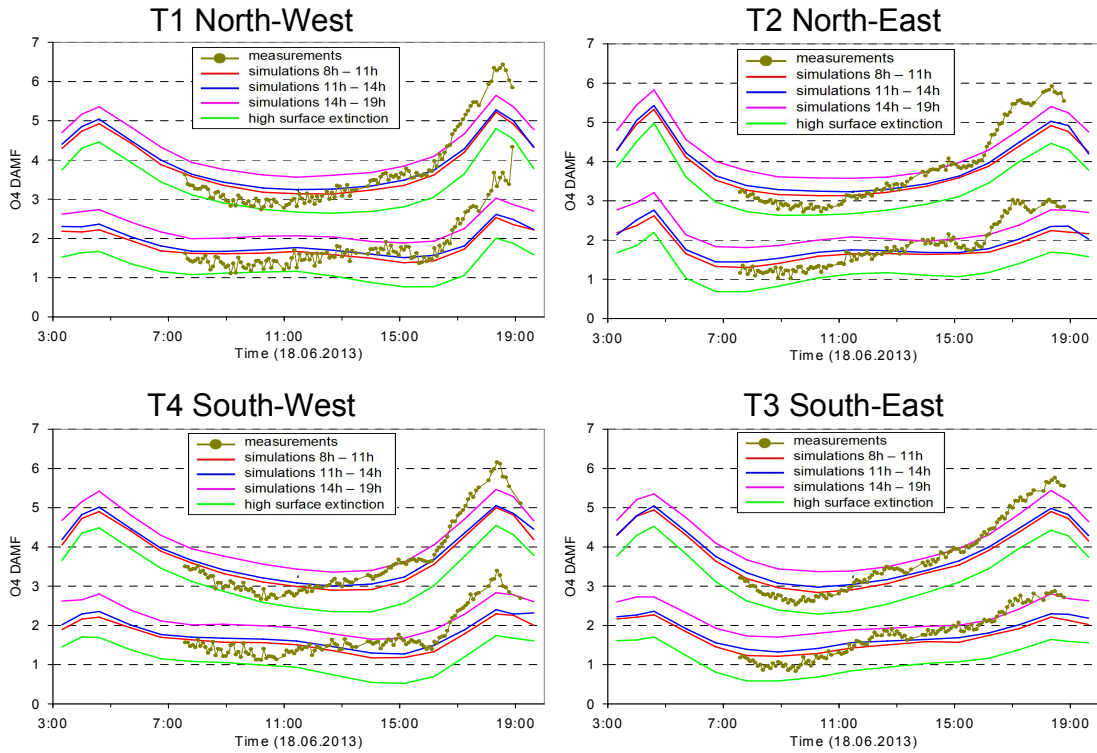
For T1 and T4 azimuth direction, no measurements at 1° elevation were possible due to obstacles.

In the following figures, the green lines indicate the results for the modified aerosol profile

For T1 and T4 azimuth direction, no measurements at 1° elevation were possible due to obstacles.

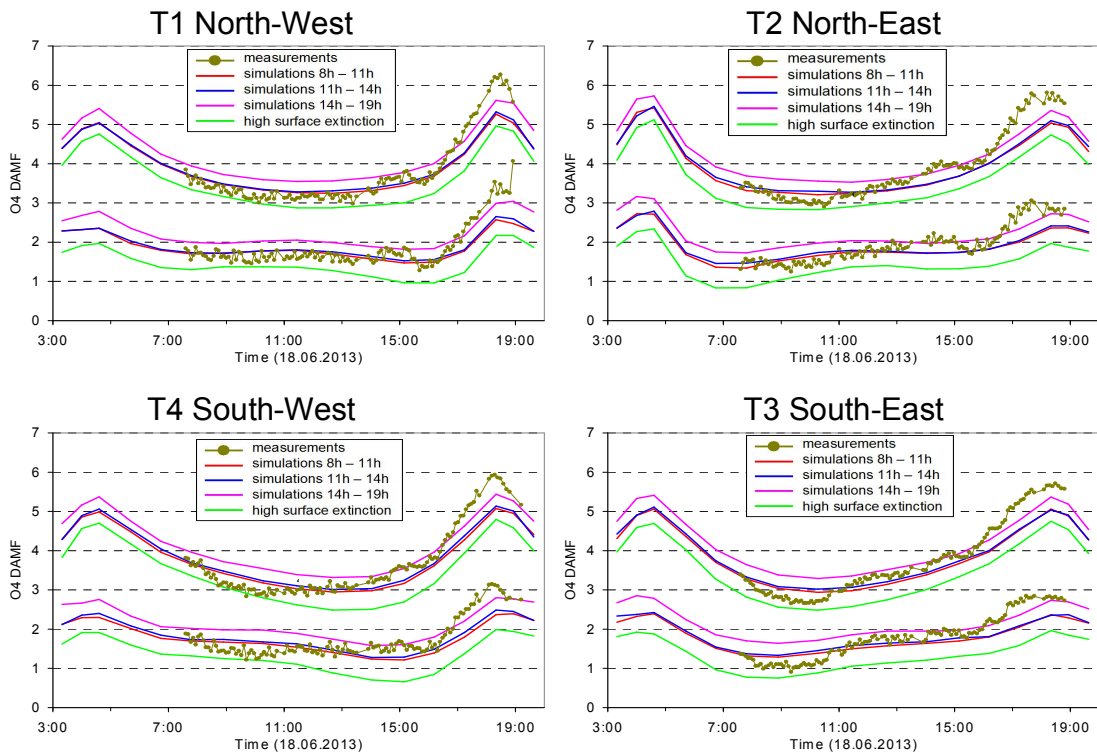
Fig. A4a Comparison results for 1° elevation angles on 18 June 2013 including the RTM results for the modified aerosol extinction profile (green line).

2022
2023
2024
2025



2026
2027
2028

Fig. A4b Comparison results for 3° elevation angles on 18 June 2013 including the RTM results for the modified aerosol extinction profile (green line)..



2029
2030
2031

Fig. A4c Comparison results for 6° elevation angles on 18 June 2013 including the RTM results for the modified aerosol extinction profile (green line).-

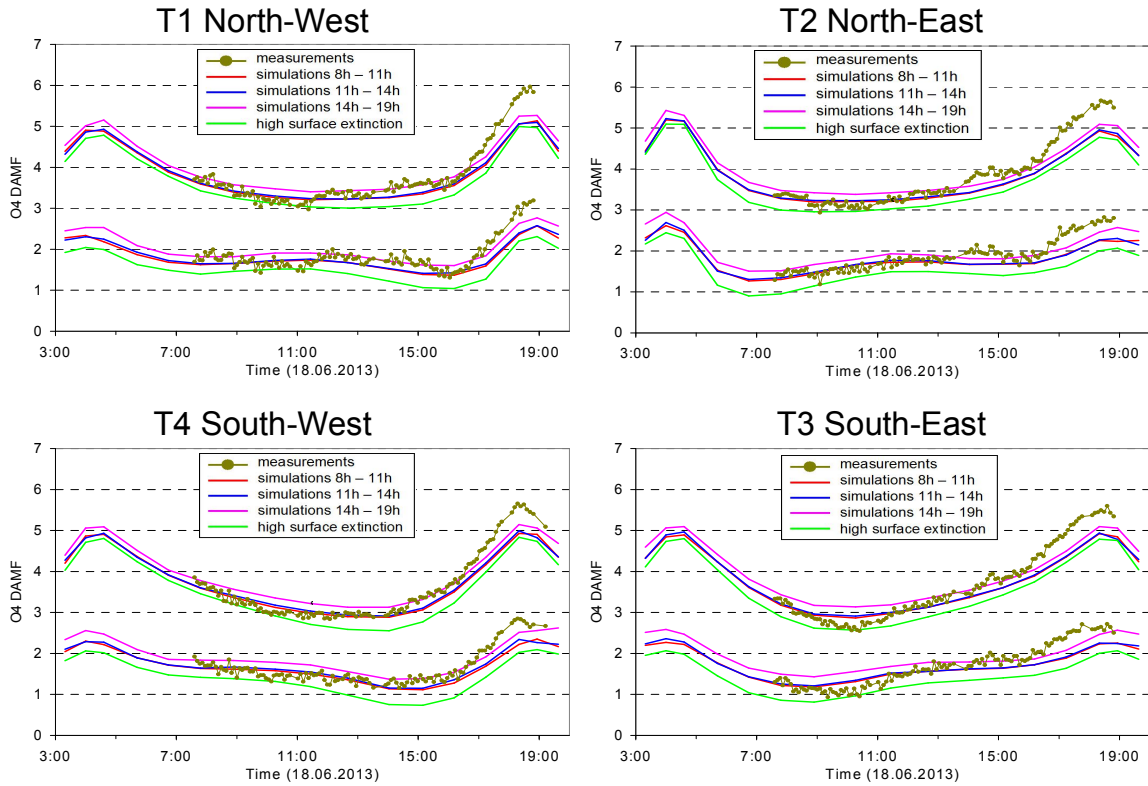


Fig. A4d Comparison results for 10° elevation angles on 18 June 2013 including the RTM results for the modified aerosol extinction profile (green line).

2032
2033
2034
2035

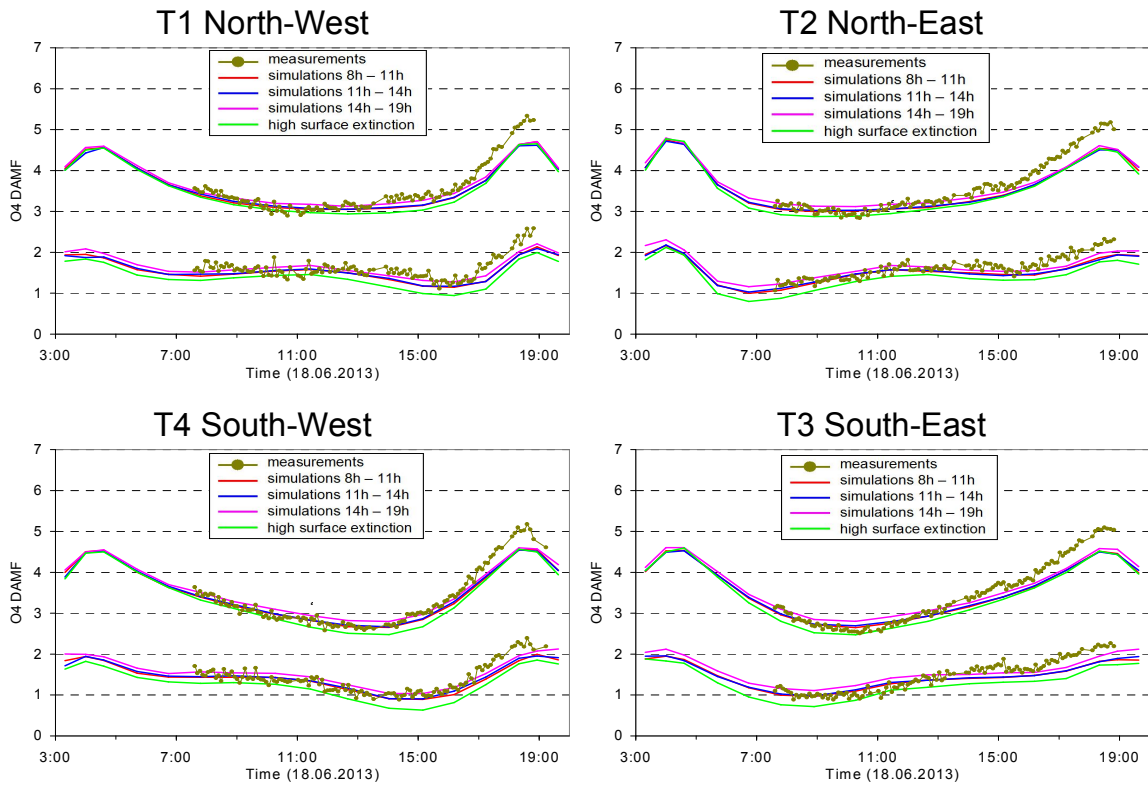
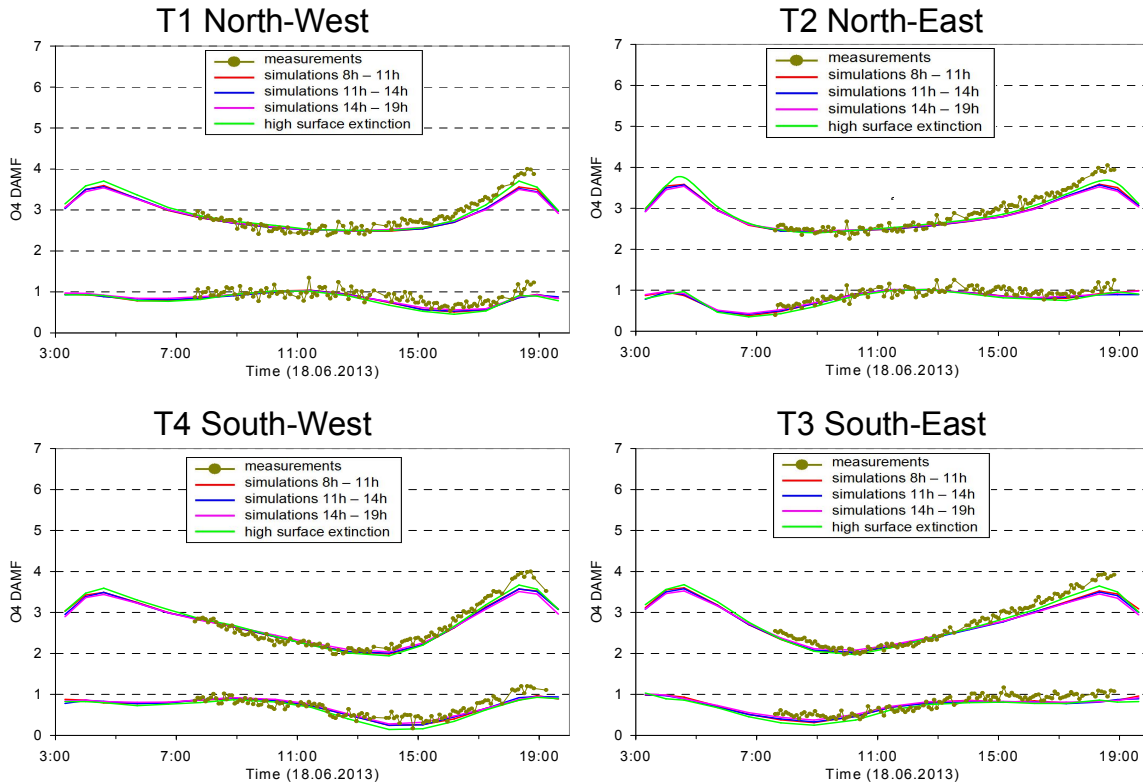


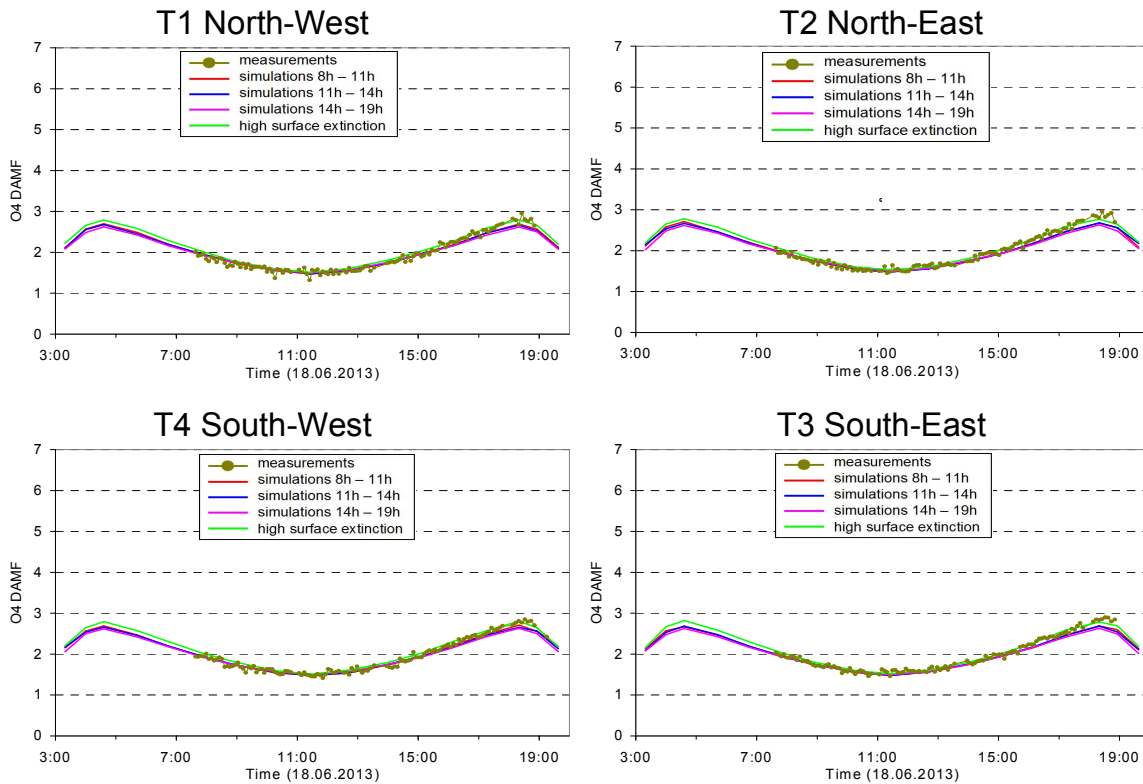
Fig. A4e Comparison results for 15° elevation angles on 18 June 2013 including the RTM results for the modified aerosol extinction profile (green line)..

2036
2037
2038



2039
2040
2041
2042

Fig. A4f Comparison results for 30° elevation angles on 18 June 2013 including the RTM results for the modified aerosol extinction profile (green line)..



2043
2044
2045

Fig. A4g Comparison results (only O₄ AMFs) for 90° elevation angles on 18 June 2013 including the RTM results for the modified aerosol extinction profile (green line).

2046 **Appendix A3 Comparison of the different procedures to extracted height profiles of**
2047 **temperature, pressure and O₄ concentration**

2048
2049 **Extraction of temperature and pressure profiles**

2050
2051 For the two selected days during the MAD-CAT campaign two data sets of temperature and
2052 pressure are available: surface measurements close to the measurement site and vertical
2053 profiles from ECMWF ERA-Interim re-analysis data (see Table 5). Both data sets are used to
2054 derive the O₄ concentration profiles for the three selected periods on both days. The general
2055 procedure is that first the temperature profiles are determined. In a second step, the pressure
2056 profiles are derived from the temperature profiles and the measured surface pressure. For the
2057 temperature profile extraction, three height layers are treated differently:

2058 -below 1 km

2059 Between the surface (~150 m above sea level) and 1 km, the temperature is linearly
2060 interpolated between the average of the in situ measurements of the respective period and the
2061 ECMWF data at 1 km (see next paragraph). This procedure is used to account for the diurnal
2062 variation of the temperature close to the surface. Here it is important to note that for this
2063 surface-near layer the highest accuracy is required, because a) the maximum O₄ concentration
2064 is located near the surface, and b) the MAX-DOAS measurements are most sensitive close to
2065 the surface.

2066 -1 km to 20 km

2067 In this altitude range, the diurnal variation of the temperature becomes very small. Thus the
2068 average of the four ECMWF profiles of each day is used (for simplicity, a 6th order
2069 polynomial is fitted to the ECMWF data).

2070 -Above 20 km

2071 In this altitude range the accuracy of the temperature profile is not critical and thus the
2072 ECMWF temperature profile for 00:00 UTC of the respective day is used for simplicity.

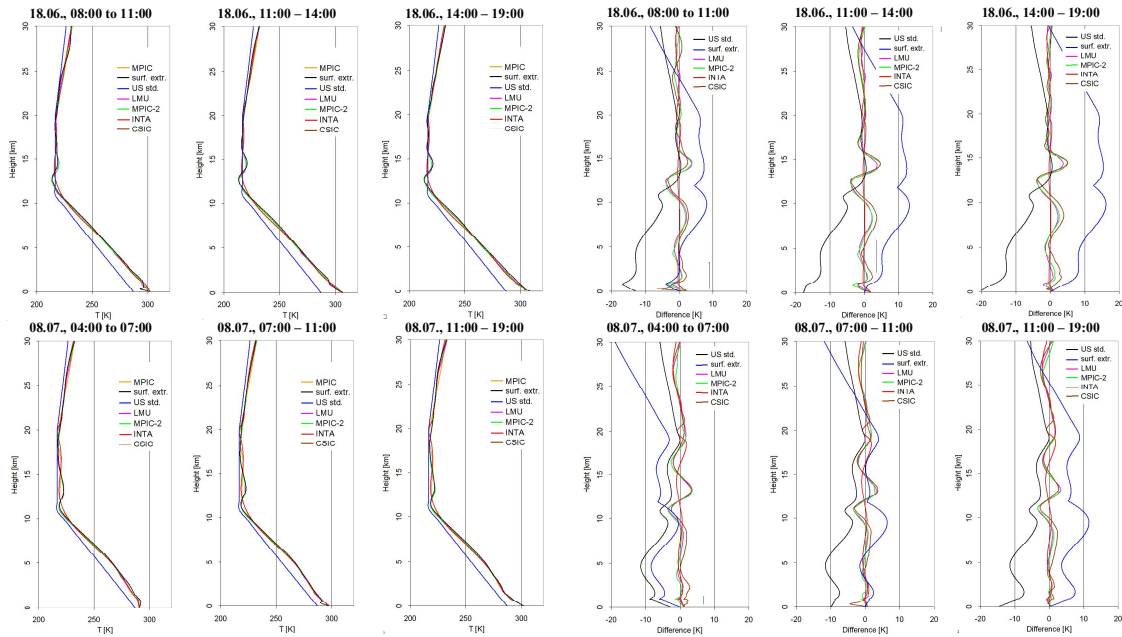
2073 The temperature profiles for 8 July 2013 extracted in this way are shown in Fig. 4 (left). Close
2074 to the surface the temperature variation during the day is about 10 K.

2075 In the next step, the pressure profiles are determined from the surface pressure (obtained from
2076 the in situ measurements) and the extracted temperature profiles according to the ideal gas
2077 law. In principle the effect of atmospheric humidity could also be taken into account, but the
2078 effect is very small for surface-near layers and is thus ignored here. The derived pressure
2079 profiles for 8 July 2013 are shown in Fig. 4 (right). Excellent agreement with the
2080 corresponding ECMWF pressure profiles is found.

2081 Here it should be noted that in principle also the ECMWF pressure profiles could be used.
2082 However, we chose to determine the pressure profiles from the surface pressure and the
2083 extracted temperature profiles, because this procedure can also be applied if no ECMWF data
2084 (or other information on temperature and pressure profiles) is available.

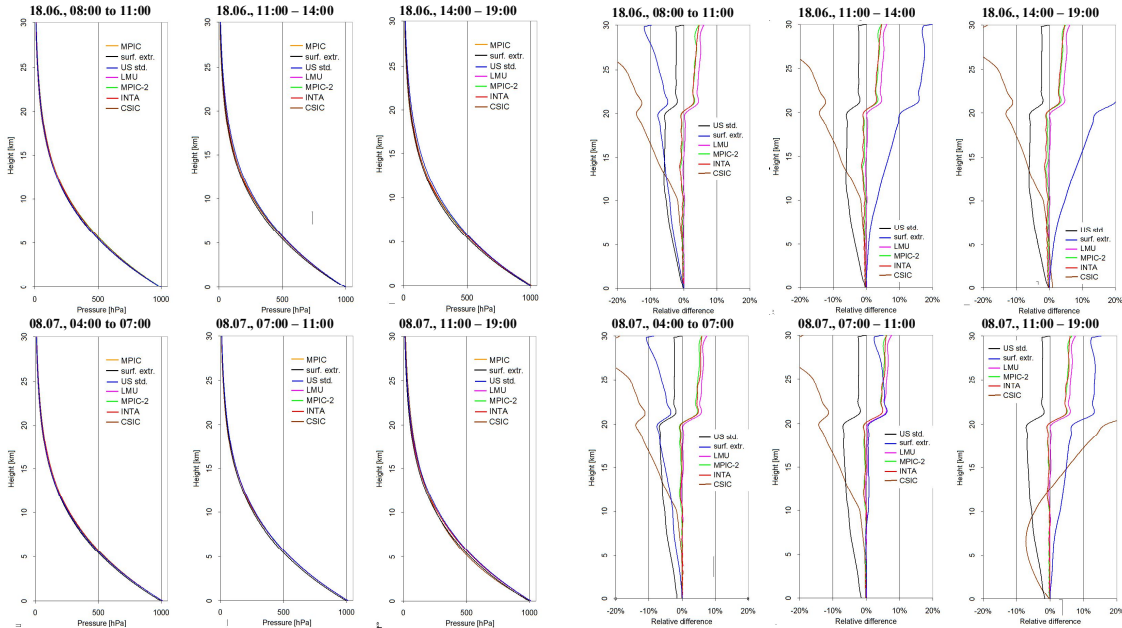
2085 If no profile data (e.g. from ECMWF) are available, temperature and pressure profiles can
2086 also be extrapolated from surface measurements e.g. by assuming a constant lapse rate of
2087 -0.65 K / 100 m for the altitude range between the surface and 12 km, and a constant
2088 temperature above 12 km (as stated above, uncertainties at this altitude range have only a
2089 negligible effect on the O₄ VCD). If no measurements or model data are available at all, a
2090 fixed temperature and pressure profile can be used, e.g. the US standard atmosphere (United
2091 States Committee on Extension to the Standard Atmosphere, 1976).

2092



2093
2094
2095
2096
2097
2098

Fig. A5a Left: Comparison of temperature profiles extracted by the different groups (also shown are the profiles from the US standard atmosphere and the profiles extrapolated from the surface measurements). Right: Differences of these profiles compared to the MPIC standard extraction.



2099
2100
2101
2102
2103
2104
2105
2106
2107
2108

Fig. A5b Left: Comparison of pressure profiles extracted by the different groups (also shown are the profiles from the US standard atmosphere and the profiles extrapolated from the surface measurements). Right: Differences of these profiles compared to the MPIC standard extraction.

2109
 2110
 2111
 2112
 2113
 2114
 2115
 2116
 2117
 2118
 2119
 2120
 2121
 2122
 2123
 2124
 2125
 2126
 2127
 2128
 2129
 2130
 2131
 2132
 2133
 2134

Determination of the uncertainties of the O₄ profiles and O₄ VCDs caused by uncertainties of the input parameters

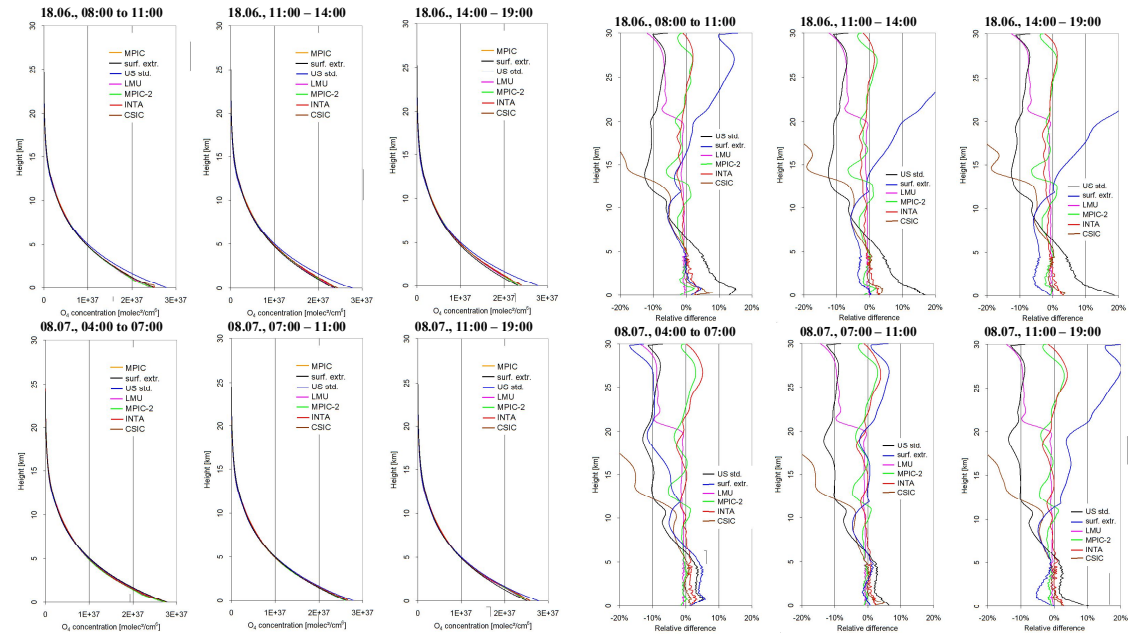
The uncertainties of the O₄ profiles and O₄ VCDs are derived by varying the input parameters according to their uncertainties. The following results are obtained:

-The variation of the temperature (whole profile) by about 2K leads to variations of the O₄ concentration (or O₄ VCD) by about 0.8%.

-The variation of the surface pressure by about 3 hPa leads to variations of the O₄ concentration (or O₄ VCD) by about 0.7%.

-The effect of uncertainties of the relative humidity depends strongly on temperature: For surface temperatures of 0°C, 10°C, 20°C, 30°C, and 35°C a variation of the relative humidity of 30% leads to variations of the O₄ concentration (or O₄ VCDs) of about 0.15%, 0.3%, 0.6%, 1.2%, and 1.6%, respectively. If the effect of atmospheric humidity is completely ignored (dry air is assumed), the resulting O₄ concentrations (or O₄ VCDs) are systematically overestimated by about 0.3%, 0.7%, 1.3%, 2.5%, and 4% for surface temperatures of 0°C, 10°C, 20°C, 30°C, and 35°C, respectively (assuming a relative humidity of 70%). In this study we used the relative humidity measured by the in situ sensors. We took these values not only for the surface layers, but also for the whole troposphere. Here it should be noted that the related uncertainties of the absolute humidity decrease quickly with altitude because the absolute humidity itself decreases quickly with altitude. Since both selected days were warm or even hot summer days, we estimate the uncertainty of the O₄ concentration and O₄ VCDs due to uncertainties of the relative humidity to 1% and 0.4% on 18 June and 8 July, respectively.

Assuming that the uncertainties of the three input parameters are independent, the total uncertainty related to these parameters is estimated to be about 1.5%.

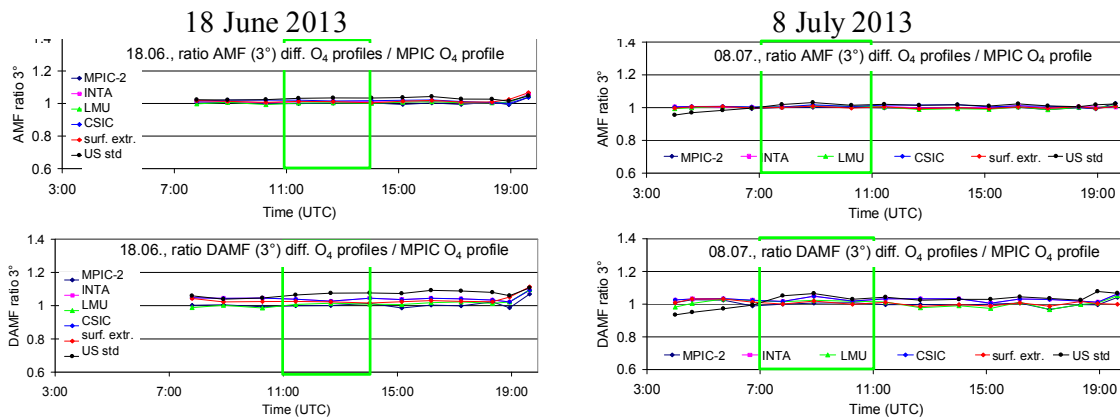


2135
 2136
 2137
 2138
 2139
 2140
 2141
 2142

Fig. A5c Left: Comparison of O₄ concentration profiles extracted by the different groups (also shown are the profiles from the US standard atmosphere and the profiles extrapolated from the surface measurements). Right: Differences of these profiles compared to the MPIC standard extraction.

2143
 2144
 2145
 2146
 2147
 2148
 2149
 2150
 2151
 2152
 2153
 2154
 2155
 2156
 2157
 2158
 2159
 2160
 2161
 2162
 2163
 2164
 2165
 2166
 2167

Appendix A4 Results of the sensitivity studies of simulated and measured O₄ (d)MFs



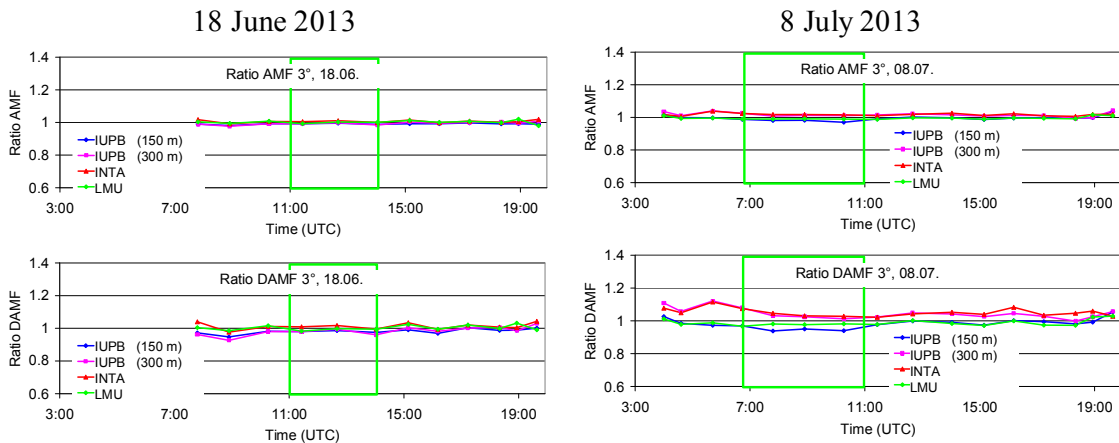
2168
 2169
 2170
 2171
 2172
 2173
 2174
 2175
 2176
 2177
 2178
 2179

Fig. A6 Ratio of the O₄ AMFs (top) and O₄ dAMFs (bottom) derived for different O₄ profiles versus the standard O₄ profile (MPIC) for both selected days. Besides the O₄ profiles extracted by the different groups, also the O₄ profiles derived from the US standard atmosphere and for the extrapolation of the surface values are included.

2180 Table A4 Average ratios of O₄ (d)AMFs simulated for different O₄ profiles versus the results
 2181 for the standard settings (using the MPIC O₄ profiles) for the two middle periods on both
 2182 selected days.

O ₄ profile extraction	AMF ratios		dAMF ratios	
	18 June 2013, 11:00 – 14:00	8 July 2013, 7:00 – 11:00	18 June 2013, 11:00 – 14:00	8 July 2013, 7:00 – 11:00
MPIC-2	1.00	1.00	1.00	1.00
INTA	1.01	1.01	1.02	1.01
LMU	1.00	1.00	1.01	1.02
CSIC	1.02	1.01	1.04	1.02
Lapse rate	1.01	1.00	1.02	1.01
US std. atm.	1.03	1.02	1.07	1.04

2183
 2184
 2185
 2186
 2187
 2188
 2189
 2190
 2191



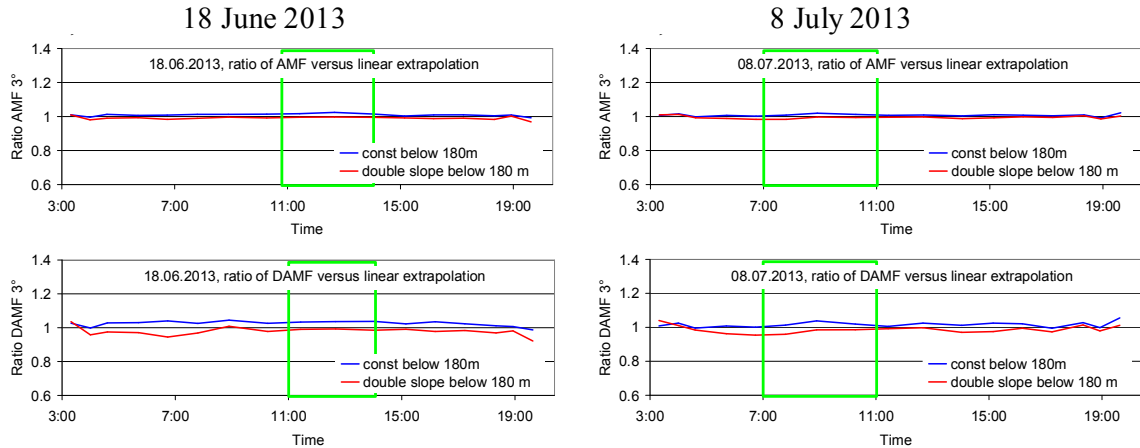
2192 Fig. A7 Ratio of the O₄ AMFs (top) and O₄ dAMFs (bottom) derived for aerosol extinction
 2193 profiles extracted by different groups versus the standard aerosol extinction profiles (MPIC)
 2194 for both selected days.
 2195

2196
 2197 Table A5 Average ratios of O₄ (d)AMFs simulated for different aerosol extinction profiles
 2198 versus the results for the standard settings (using the MPIC aerosol extinction profiles) for the
 2199 two middle periods on both selected days.

Aerosol profile extraction	AMF ratios		dAMF ratios	
	18 June 2013, 11:00 – 14:00	8 July 2013, 7:00 – 11:00	18 June 2013, 11:00 – 14:00	8 July 2013, 7:00 – 11:00
INTA	1.01	1.02	1.01	1.04

IUP-B 150 m	0.99	0.98		0.98	0.96
IUP-B 300 m	0.99	1.01		0.98	1.03
LMU	1.00	0.99		0.99	0.98

2200
2201



2202
2203
2204
2205
2206
2207
2208
2209
2210
2211

Fig. A8 Ratio of the O₄ AMFs (top) and O₄ dAMFs (bottom) derived for different extrapolations of the aerosol extinction profiles below 180 m versus those for the standard settings (linearly extrapolated profiles) for both selected days.

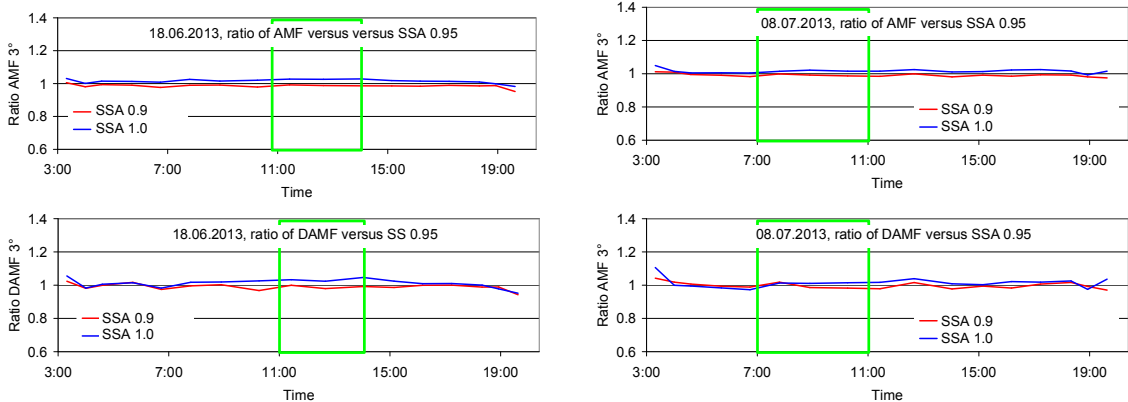
Table A6 Average ratios of O₄ (d)AMFs simulated for aerosol extinction profiles with different extrapolations below 180 m versus the results for the standard settings (linear extrapolation) for the two middle periods on both selected days.

Extrapolation below 180 m	AMF ratios		dAMF ratios	
	18 June 2013, 11:00 – 14:00	8 July 2013, 7:00 – 11:00	18 June 2013, 11:00 – 14:00	8 July 2013, 7:00 – 11:00
Constant extinction	1.02	1.01	1.04	1.02
Double slope	1.00	0.99	0.99	0.98

2212
2213
2214

18 June 2013

8 July 2013



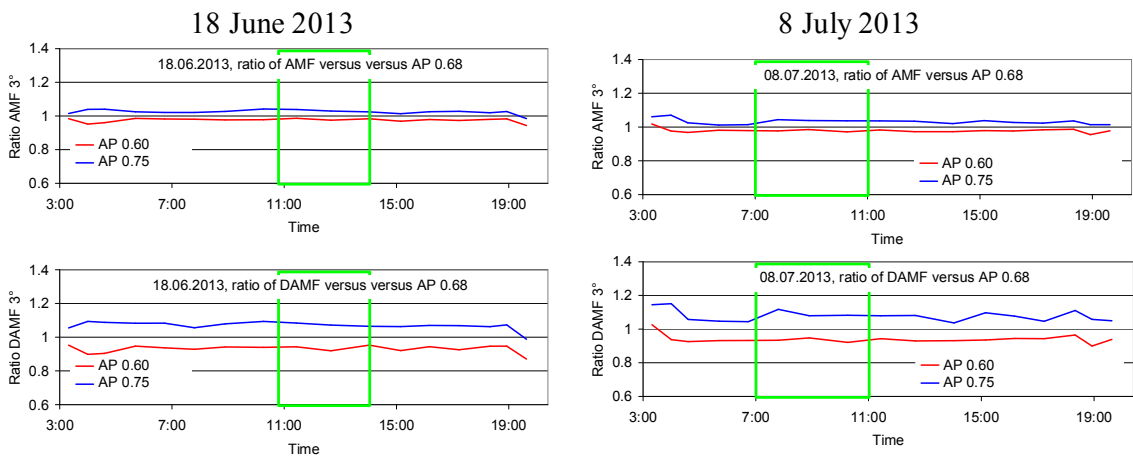
2215
 2216
 2217
 2218
 2219
 2220
 2221
 2222
 2223
 2224
 2225

Fig. A9 Ratio of the O₄ AMFs (top) and O₄ dAMFs (bottom) derived for different aerosol single scattering albedos versus those for the standard settings (single scattering albedo of 0.95) for both selected days.

Table A7 Average ratios of O₄ (d)AMFs simulated for different aerosol single scattering albedos (SSA) versus the results for the standard settings (single scattering albedo of 0.95) for the two middle periods on both selected days.

Single scattering albedo	AMF ratios		dAMF ratios	
	18 June 2013, 11:00 – 14:00	8 July 2013, 7:00 – 11:00	18 June 2013, 11:00 – 14:00	8 July 2013, 7:00 – 11:00
0.9	0.99	0.99	0.99	0.99
1.0	1.03	1.01	1.03	1.01

2226
 2227
 2228
 2229
 2230
 2231
 2232

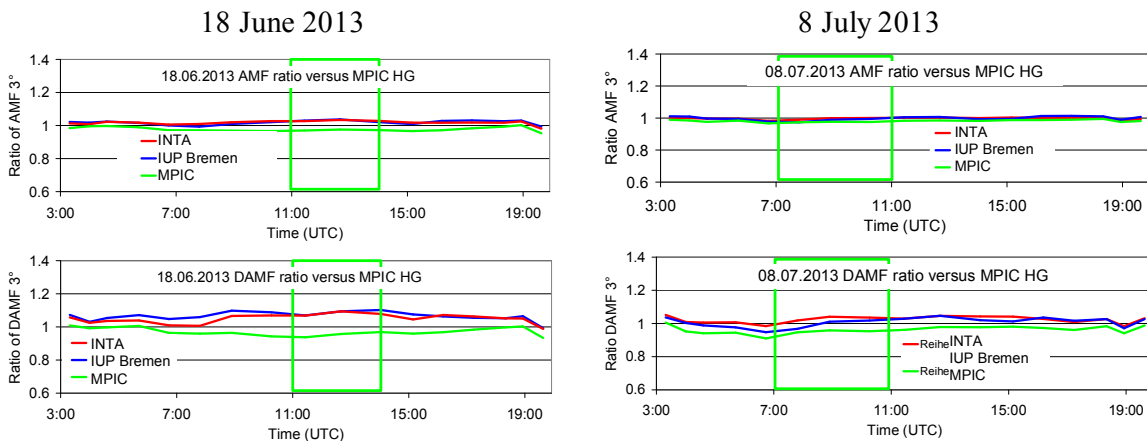


2233 Fig. A10 Ratio of the O₄ AMFs (top) and O₄ dAMFs (bottom) derived for different aerosol
 2234 phase functions (HG-parameterisation with different asymmetry parameters) versus those for
 2235 the standard settings (asymmetry parameter of 0.68) for both selected days.
 2236
 2237
 2238
 2239

2240 Table A8 Average ratios of O₄ (d)AMFs simulated for different aerosol phase functions (HG-
 2241 parameterisation with different asymmetry parameters (AP) versus the results for the standard
 2242 settings (asymmetry parameter of 0.68) for the two middle periods on both selected days.

	AMF ratios			dAMF ratios	
Asymmetry parameter	18 June 2013, 11:00 – 14:00	8 July 2013, 7:00 – 11:00		18 June 2013, 11:00 – 14:00	8 July 2013, 7:00 – 11:00
0.6	0.98	0.98		0.94	0.94
0.75	1.03	1.03		1.08	1.07

2243
 2244
 2245

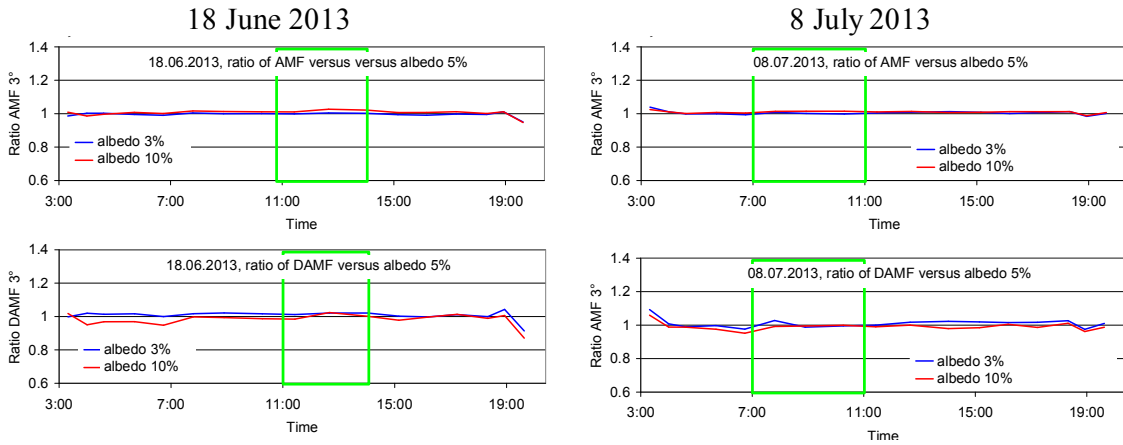


2246 Fig. A11 Ratio of the O₄ AMFs (top) and O₄ dAMFs (bottom) simulated by INTA and IUP-
 2247 Bremen and MPIC (SCIATRAN) for phase functions derived from the sun photometer
 2248 measurements versus those simulated by MPIC using the Henyey Greenstein phase function
 2249 for asymmetry parameter of 0.68 for both selected days.
 2250
 2251

2252 Table A9 Average ratios of O₄ (d)AMFs simulated by INTA and IUP-Bremen and MPIC
 2253 (SCIATRAN) for phase functions derived from the sun photometer measurements versus
 2254 those simulated by MPIC using the Henyey Greenstein phase function for asymmetry
 2255 parameter of 0.68 for the two middle periods on both selected days.

	AMF ratios			dAMF ratios	
Group (RTM)	18 June 2013, 11:00 – 14:00	8 July 2013, 7:00 – 11:00		18 June 2013, 11:00 – 14:00	8 July 2013, 7:00 – 11:00
INTA (LIDORT)	1.03	1.00		1.09	1.02
IUP-Bremen (SCIATRAN)	1.03	0.99		1.08	0.99
MPIC	0.97	0.98		0.95	0.95

2256
2257
2258



2259
2260
2261
2262
2263
2264
2265
2266
2267
2268

Fig. A12 Ratio of the O₄ AMFs (top) and O₄ dAMFs (bottom) for different surface albedos versus those for an albedo of 5 % for both selected days.

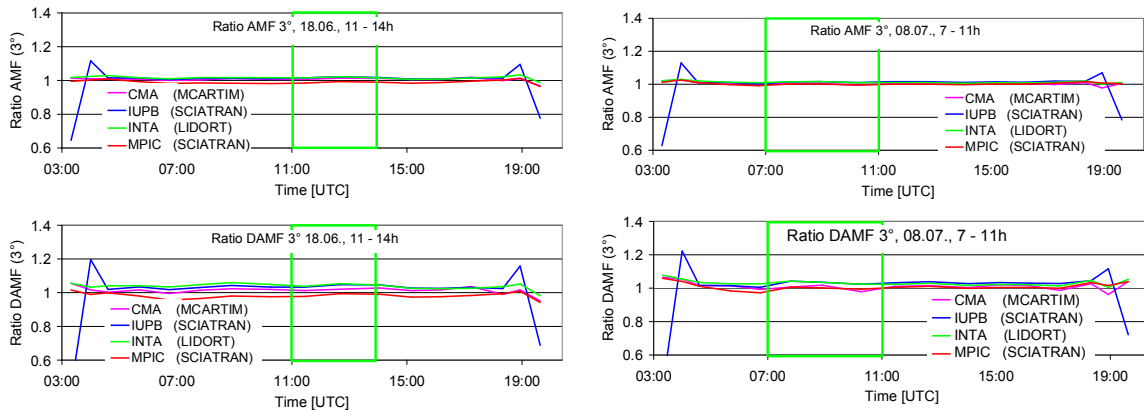
Table A12-A10 Average ratios of O₄ (d)AMFs for different surface albedos versus those for an albedo of 5 % for the two middle periods on both selected days.

Surface albedo	AMF ratios		dAMF ratios	
	18 June 2013, 11:00 – 14:00	8 July 2013, 7:00 – 11:00	18 June 2013, 11:00 – 14:00	8 July 2013, 7:00 – 11:00
3 %	1.00	1.00	1.02	1.00
10 %	1.02	1.01	1.00	0.99

2269
2270
2271
2272
2273
2274
2275

18 June 2013

8 July 2013



2276
2277
2278
2279
2280
2281
2282
2283
2284
2285
2286

Fig. A13 Ratio of the O₄ AMFs (top) and O₄ dAMFs (bottom) simulated by different groups using different radiative transfer models versus those for the MPIC simulations using MCARTIM for both selected days.

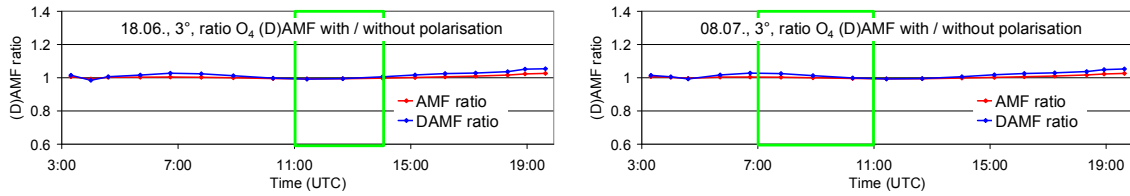
Table A11 Average ratios of O₄ (d)AMFs simulated by different groups using different radiative transfer models versus those for the MPIC simulations using MCARTIM for the two middle periods on both selected days.

Group (RTM)	AMF ratios		dAMF ratios	
	18 June 2013, 11:00 – 14:00	8 July 2013, 7:00 – 11:00	18 June 2013, 11:00 – 14:00	8 July 2013, 7:00 – 11:00
CMA (MCARTIM)	1.01	1.00	1.02	1.00
IUP-Bremen (SCIATRAN)	1.02	1.01	1.04	1.03
INTA (LIDORT)	1.02	1.01	1.05	1.03
MPIC (SCIATRAN)	0.99	1.00	0.99	1.00

2287
2288
2289
2290
2291
2292
2293
2294
2295
2296
2297
2298
2299
2300
2301

18 June 2013

8 July 2013



2302
2303
2304
2305
2306
2307
2308
2309

Fig. A14 Ratio of the O₄ (d)AMFs considering polarisation versus those without considering polarisation for both selected days.

Table A12 Average ratios of O₄ (d)AMFs considering polarisation versus those without considering polarisation for the two middle periods on both selected days.

	AMF ratios			dAMF ratios	
	18 June 2013, 11:00 – 14:00	8 July 2013, 7:00 – 11:00		18 June 2013, 11:00 – 14:00	8 July 2013, 7:00 – 11:00
Considering polarisation	1.00	1.00		1.00	1.01

2310
2311
2312
2313
2314
2315
2316
2317
2318

Table A13 Average ratios of O₄ (d)AMFs derived from synthetic spectra versus those obtained from radiative transfer simulations at 360 nm for the two middle periods on both selected days.

	AMF ratios			dAMF ratios	
Temperature dependence / noise	18 June 2013, 11:00 – 14:00	8 July 2013, 7:00 – 11:00		18 June 2013, 11:00 – 14:00	8 July 2013, 7:00 – 11:00
T dep. considered / no noise	1.01	1.02		1.01	1.00
no T dep. considered / no noise	1.00	1.01		1.00	1.00
no T dep. considered / noise	0.99	1.00		1.00	1.01

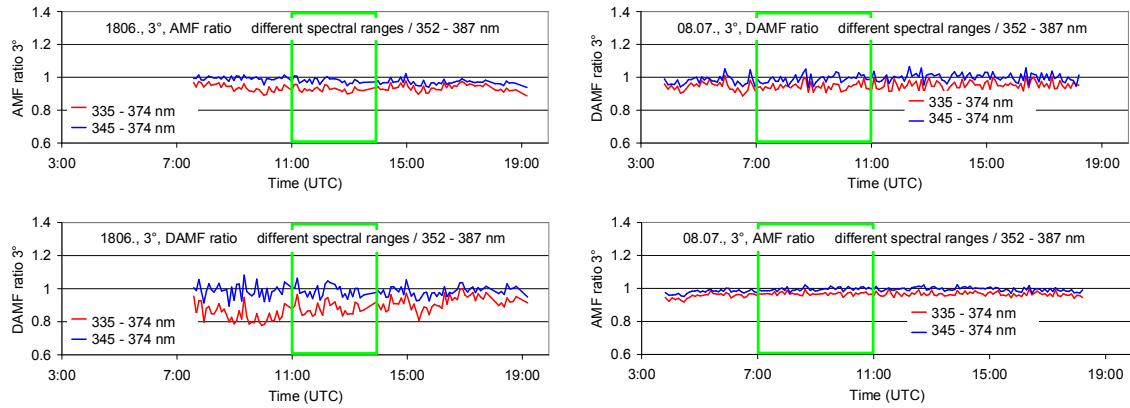
2319
2320
2321
2322
2323
2324
2325
2326

18 June 2013

8 July 2013

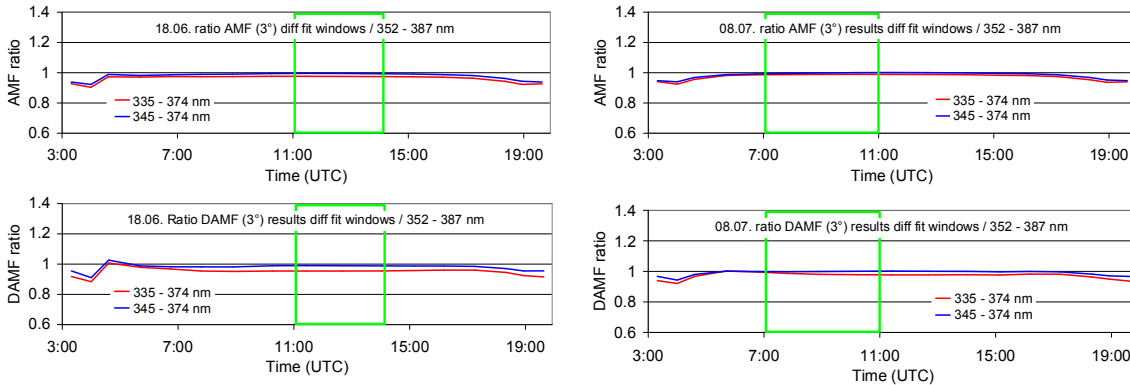
2327

a) measured spectra



2328
2329

b) synthetic spectra



2330

2331

2332

2333

2334

2335

2336

2337

2338

2339

2340

Fig. A15 Ratio of the O₄ (d)AMFs derived for different fit windows versus those for the standard fit window (352 – 387 nm) for both selected days (top: results for spectra measured by the MPIC instrument; bottom: results for synthetic spectra taking into account the temperature dependence of the O₄ cross section).

Table A14 Average ratios of O₄ (d)AMFs derived for different fit windows versus those for the standard fit window (352 – 387 nm) for the two middle periods on both selected days (top: results for spectra measured by the MPIC instrument; bottom: results for synthetic spectra taking into account the temperature dependence of the O₄ cross section).

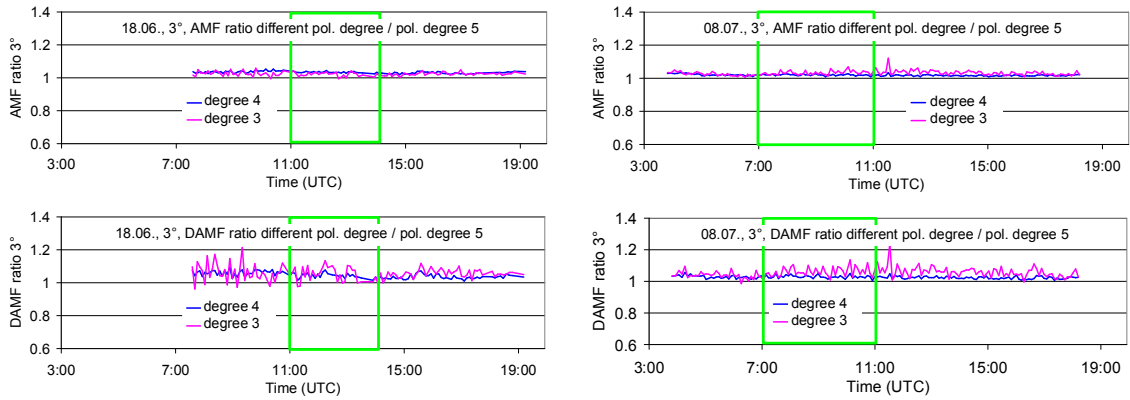
	AMF ratios			dAMF ratios	
Spectral range	18 June 2013, 11:00 – 14:00	8 July 2013, 7:00 – 11:00		18 June 2013, 11:00 – 14:00	8 July 2013, 7:00 – 11:00
Measured Spectra					
335 – 374 nm	0.93	0.97		0.88	0.94
345 – 374 nm	0.98	1.00		0.99	0.99
Synthetic Spectra					
335 – 374 nm	0.98	0.99		0.95	0.98
345 – 374 nm	0.99	1.00		0.99	1.00

2341

18 June 2013

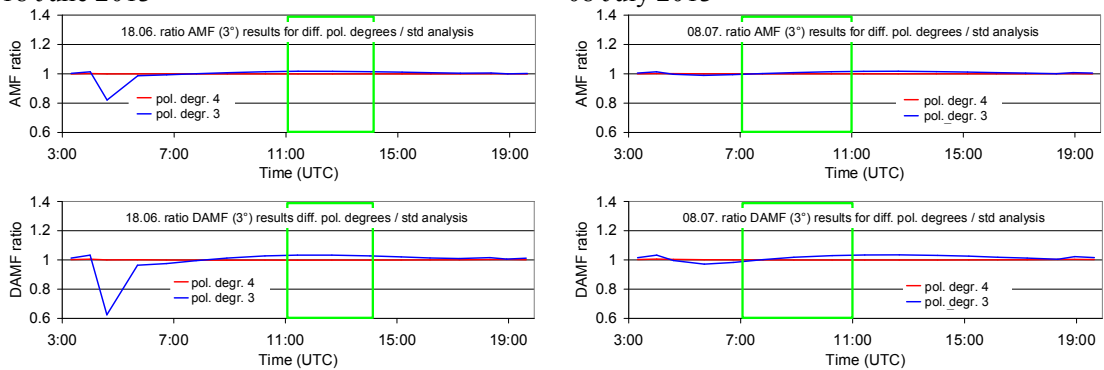
8 July 2013

2342 a) measured spectra



2343
2344

b) synthetic spectra



2345
2346
2347
2348
2349
2350
2351
2352

Fig. A16 Ratio of the O₄ (d)AMFs derived for different polynomials versus those for the standard analysis (polynomial degree 5) for both selected days (top: results for spectra measured by the MPIC instrument; bottom: results for synthetic spectra taking into account the temperature dependence of the O₄ cross section).

2353
2354
2355
2356

Table A15 Average ratios of O₄ (d)AMFs derived for different polynomials versus those for the standard analysis (polynomial degree 5) for the two middle periods on both selected days (top: results for spectra measured by the MPIC instrument; bottom: results for synthetic spectra taking into account the temperature dependence of the O₄ cross section).

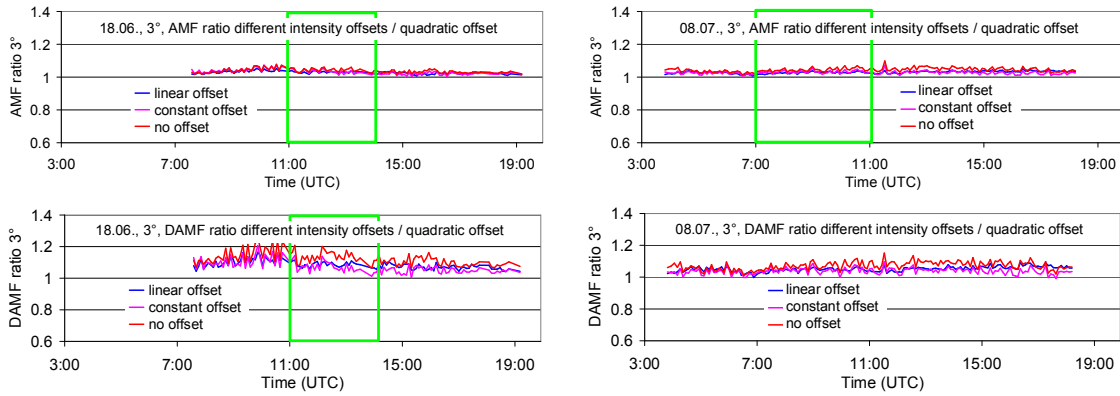
Degree of polynomial	AMF ratios			dAMF ratios	
	18 June 2013, 11:00 – 14:00	8 July 2013, 7:00 – 11:00		18 June 2013, 11:00 – 14:00	8 July 2013, 7:00 – 11:00
Measured Spectra					
4	1.04	1.02		1.06	1.03
3	1.03	1.03		1.06	1.06
Synthetic Spectra					
4	1.00	1.00		1.00	1.00
3	1.02	1.01		1.03	1.01

2357

18 June 2013

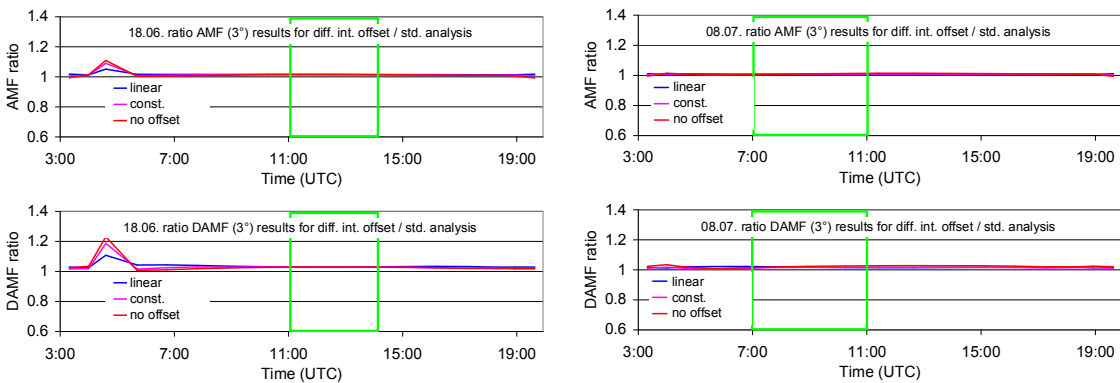
8 July 2013

2358 a) measured spectra



2359
2360

b) synthetic spectra



2361
2362
2363
2364
2365
2366
2367
2368
2369
2370
2371
2372
2373
2374
2375
2376
2377
2378
2379
2380
2381
2382
2383
2384
2385
2386
2387

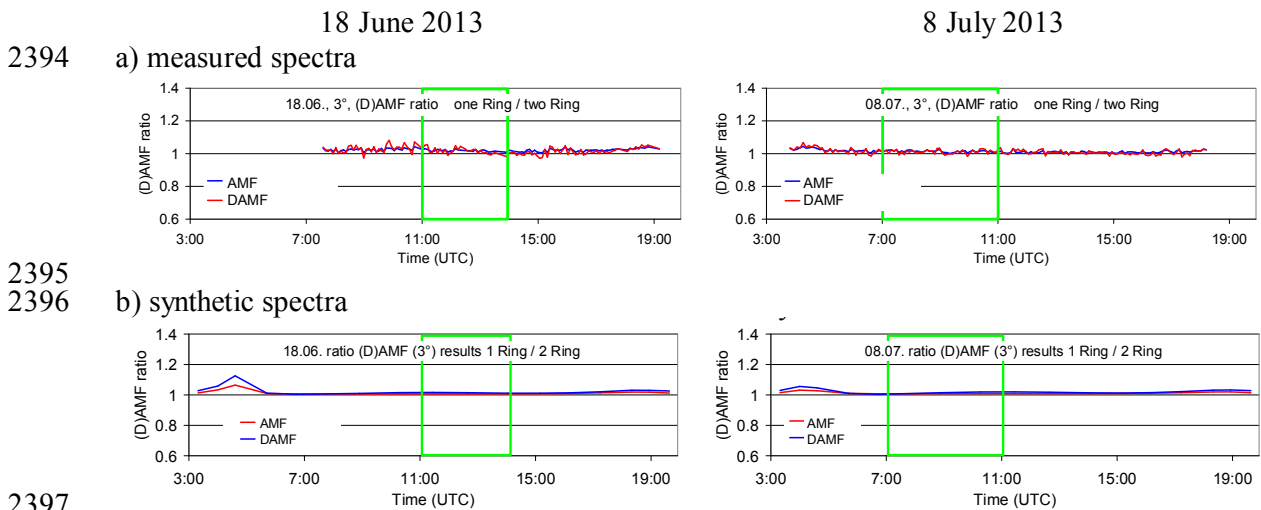
Fig. A17 Ratio of the O_4 (d)AMFs derived for different intensity offsets versus those for the standard analysis (intensity offset of degree 2) for both selected days (top: results for spectra measured by the MPIC instrument; bottom: results for synthetic spectra taking into account the temperature dependence of the O_4 cross section).

Table A16 Average ratios of O_4 (d)AMFs derived for different intensity offsets versus those for the standard analysis (intensity offset of degree 2) for the two middle periods on both

2388 selected days (top: results for spectra measured by the MPIC instrument; bottom: results for
 2389 synthetic spectra taking into account the temperature dependence of the O₄ cross section).

	AMF ratios			dAMF ratios	
Intensity offset	18 June 2013, 11:00 – 14:00	8 July 2013, 7:00 – 11:00		18 June 2013, 11:00 – 14:00	8 July 2013, 7:00 – 11:00
Measured Spectra					
Linear	1.04	1.03		1.11	1.05
Constant	1.05	1.03		1.11	1.04
No offset	1.05	1.05		1.16	1.07
Synthetic Spectra					
Linear	1.01	1.01		1.03	1.02
Constant	1.02	1.01		1.03	1.02
No offset	1.02	1.01		1.03	1.02

2390
 2391
 2392
 2393



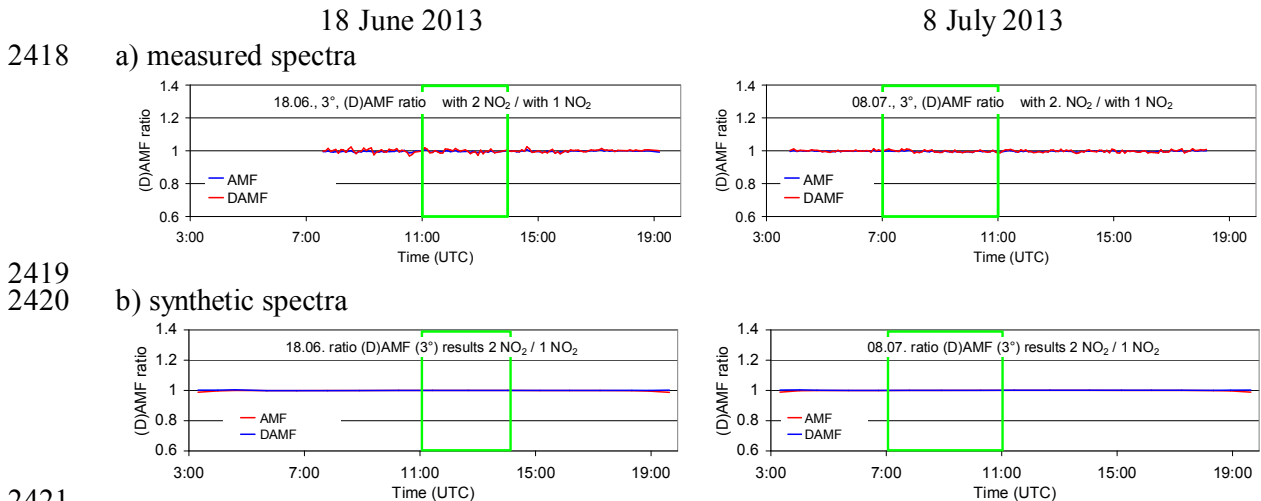
2397
 2398 Fig. A18 Ratio of the O₄ (d)AMFs derived for the analysis with only one Ring spectrum
 2399 versus those for the standard analysis (using two Ring spectra) for both selected days (top:
 2400 results for spectra measured by the MPIC instrument; bottom: results for synthetic spectra
 2401 taking into account the temperature dependence of the O₄ cross section).
 2402
 2403
 2404
 2405
 2406
 2407
 2408

2409 Table A17 Average ratios of O₄ (d)AMFs derived for the analysis with only one Ring
 2410 spectrum versus those for the standard analysis (using two Ring spectra) for the two middle
 2411 periods on both selected days (top: results for spectra measured by the MPIC instrument;

2412 bottom: results for synthetic spectra taking into account the temperature dependence of the O₄
 2413 cross section).

	AMF ratios			dAMF ratios	
Ring correction	18 June 2013, 11:00 – 14:00	8 July 2013, 7:00 – 11:00		18 June 2013, 11:00 – 14:00	8 July 2013, 7:00 – 11:00
Measured Spectra					
Only one Ring spectrum	1.02	0.99		1.01	0.99
Synthetic Spectra					
Only one Ring spectrum	1.01	1.01		1.01	1.01

2414
 2415
 2416
 2417

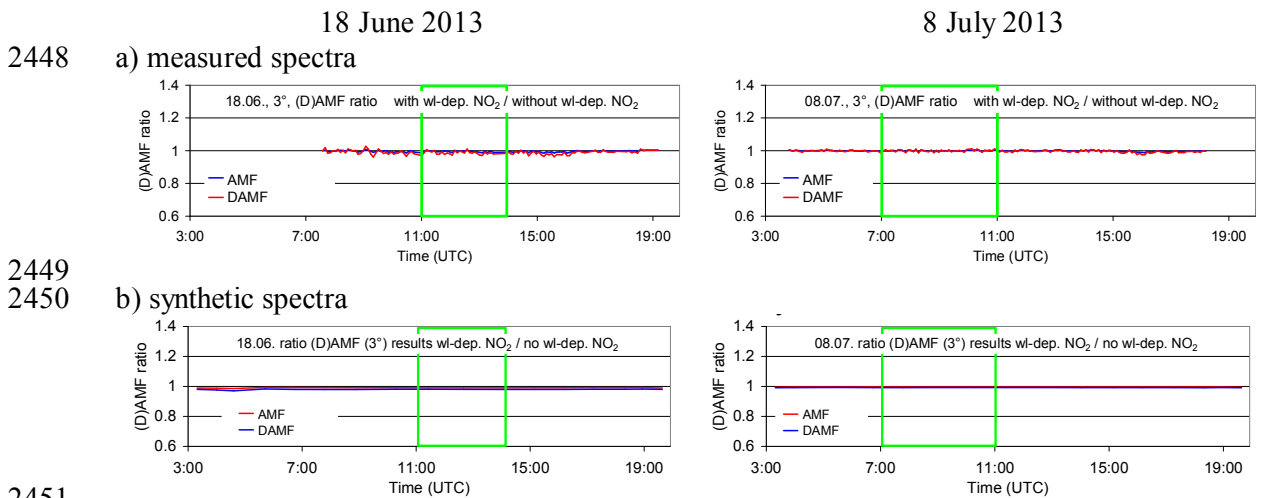


2421
 2422 Fig. A19 Ratio of the O₄ (d)AMFs derived for the analysis with a second NO₂ cross section
 2423 (for 220 K) versus those for the standard analysis (only NO₂ cross section for 294 K) for both
 2424 selected days (top: results for spectra measured by the MPIC instrument; bottom: results for
 2425 synthetic spectra taking into account the temperature dependence of the O₄ cross section).
 2426
 2427
 2428
 2429
 2430
 2431
 2432
 2433
 2434
 2435
 2436
 2437
 2438

2439 Table A18 Average ratios of O₄ (d)AMFs derived for the analysis with a second NO₂ cross
 2440 section (for 220 K) versus those for the standard analysis (only NO₂ cross section for 294 K)
 2441 for the two middle periods on both selected days (top: results for spectra measured by the
 2442 MPIC instrument; bottom: results for synthetic spectra taking into account the temperature
 2443 dependence of the O₄ cross section).

	AMF ratios			dAMF ratios	
NO ₂ cross sections	18 June 2013, 11:00 – 14:00	8 July 2013, 7:00 – 11:00		18 June 2013, 11:00 – 14:00	8 July 2013, 7:00 – 11:00
Measured Spectra					
294 & 220 K	1.00	1.00		1.00	1.00
Synthetic Spectra					
294 & 220 K	1.00	1.00		1.00	1.00

2444
 2445
 2446
 2447

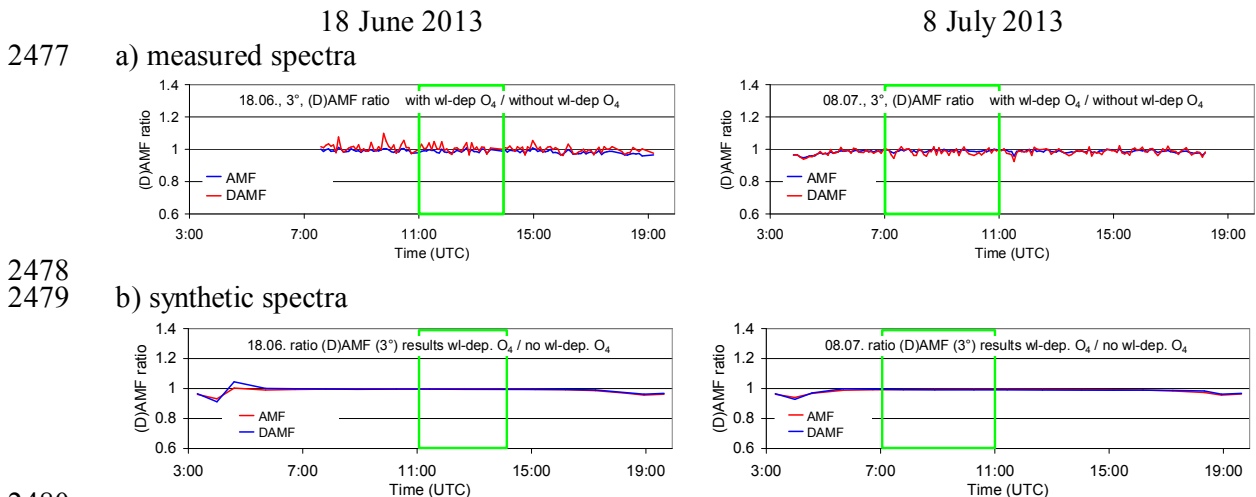


2451
 2452 Fig. A20 Ratio of the O₄ (d)AMFs derived for the analysis with a second NO₂ cross
 2453 section (cross section times wavelength) versus those for the standard analysis (only one NO₂ cross
 2454 section) for both selected days (top: results for spectra measured by the MPIC instrument;
 2455 bottom: results for synthetic spectra taking into account the temperature dependence of the O₄
 2456 cross section).
 2457
 2458
 2459
 2460
 2461
 2462
 2463
 2464
 2465
 2466
 2467

2468 Table A19 Average ratios of O₄ (d)AMFs derived for the analysis with a second NO₂ cross
 2469 section (cross section times wavelength) versus those for the standard analysis (only one NO₂
 2470 cross section) for the two middle periods on both selected days (top: results for spectra
 2471 measured by the MPIC instrument; bottom: results for synthetic spectra taking into account
 2472 the temperature dependence of the O₄ cross section).

	AMF ratios			dAMF ratios	
NO ₂ wavelength dependence	18 June 2013, 11:00 – 14:00	8 July 2013, 7:00 – 11:00		18 June 2013, 11:00 – 14:00	8 July 2013, 7:00 – 11:00
Measured Spectra					
additional cross for wavelength dependence	1.00	1.00		0.99	1.00
Synthetic Spectra					
additional cross for wavelength dependence	0.99	1.00		0.98	0.99

2473
 2474
 2475
 2476



2480
 2481 Fig. A21 Ratio of the O₄ (d)AMFs derived for the analysis with a second O₄ cross
 2482 section (accounting for the wavelength dependence) versus those for the standard analysis (only one
 2483 O₄ cross section) for both selected days (top: results for spectra measured by the MPIC
 2484 instrument; bottom: results for synthetic spectra taking into account the temperature
 2485 dependence of the O₄ cross section).
 2486
 2487
 2488
 2489
 2490
 2491
 2492

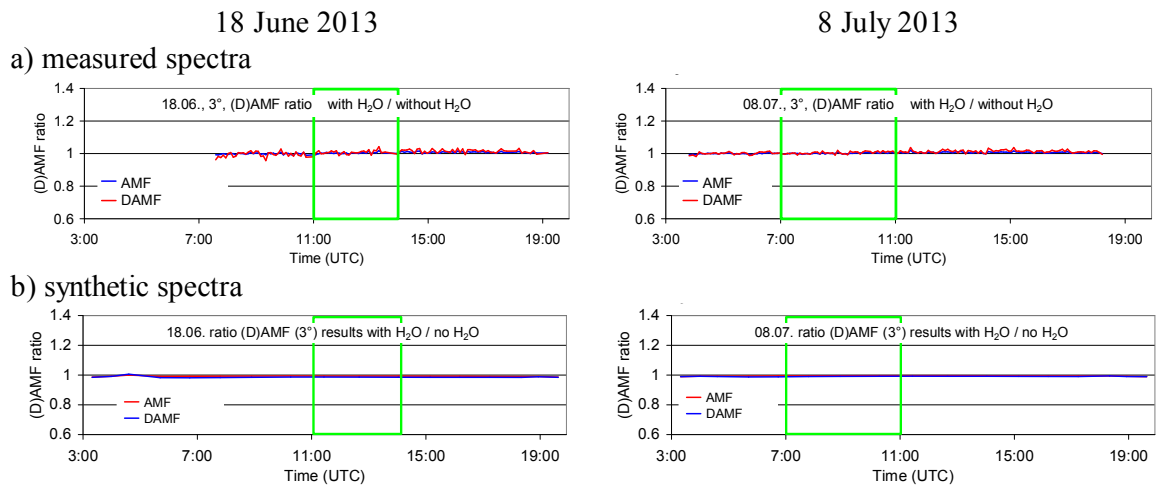
2493
 2494
 2495
 2496
 2497
 2498

Table A20 Average ratios of O₄ (d)AMFs derived for the analysis with a second O₄ cross section (accounting for the wavelength dependence) versus those for the standard analysis (only one O₄ cross section) for the two middle periods on both selected days (top: results for spectra measured by the MPIC instrument; bottom: results for synthetic spectra taking into account the temperature dependence of the O₄ cross section).

	AMF ratios			dAMF ratios	
O ₄ wavelength dependence	18 June 2013, 11:00 – 14:00	8 July 2013, 7:00 – 11:00		18 June 2013, 11:00 – 14:00	8 July 2013, 7:00 – 11:00
Measured Spectra					
additional cross for wavelength dependence	0.99	0.99		1.01	0.99
Synthetic Spectra					
additional cross for wavelength dependence	1.00	0.99		1.00	0.99

2499
 2500
 2501
 2502
 2503

2504



2505
 2506

2507
 2508
 2509
 2510
 2511
 2512
 2513
 2514
 2515
 2516
 2517
 2518
 2519

Fig. A22 Ratio of the O₄ (d)AMFs derived for the analysis including a H₂O cross section versus those for the standard analysis (no H₂O cross section) for both selected days (top: results for spectra measured by the MPIC instrument; bottom: results for synthetic spectra taking into account the temperature dependence of the O₄ cross section).

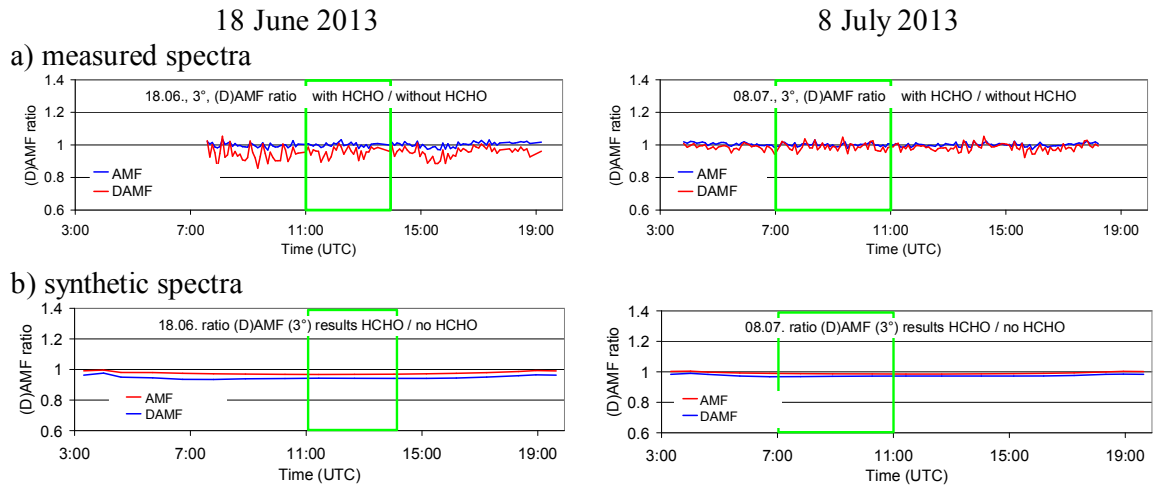
2520
 2521
 2522
 2523
 2524
 2525

Table A21 Average ratios of O₄ (d)AMFs derived for the analysis including a H₂O cross section versus those for the standard analysis (no H₂O cross section) for the standard analysis (only one O₄ cross section) for the two middle periods on both selected days (top: results for spectra measured by the MPIC instrument; bottom: results for synthetic spectra taking into account the temperature dependence of the O₄ cross section).

	AMF ratios			dAMF ratios	
H ₂ O cross section	18 June 2013, 11:00 – 14:00	8 July 2013, 7:00 – 11:00		18 June 2013, 11:00 – 14:00	8 July 2013, 7:00 – 11:00
Measured spectra					
H ₂ O cross section included	1.00	1.00		1.01	1.01
Synthetic Spectra					
H ₂ O cross section included	0.99	1.00		0.99	0.99

2526
 2527
 2528

2529



2530

2531
 2532
 2533
 2534
 2535
 2536
 2537
 2538
 2539
 2540
 2541
 2542
 2543
 2544

Fig. A23 Ratio of the O₄ (d)AMFs derived for the analysis including a HCHO cross section versus those for the standard analysis (no HCHO cross section) for both selected days (top: results for spectra measured by the MPIC instrument; bottom: results for synthetic spectra taking into account the temperature dependence of the O₄ cross section).

2545
 2546
 2547
 2548
 2549
 2550

Table A22 Average ratios of O₄ (d)AMFs derived for the analysis including a HCHO cross section versus those for the standard analysis (no HCHO cross section) for the standard analysis (only one O₄ cross section) for the two middle periods on both selected days (top: results for spectra measured by the MPIC instrument; bottom: results for synthetic spectra taking into account the temperature dependence of the O₄ cross section).

	AMF ratios			dAMF ratios	
HCHO cross section	18 June 2013, 11:00 – 14:00	8 July 2013, 7:00 – 11:00		18 June 2013, 11:00 – 14:00	8 July 2013, 7:00 – 11:00
Measured Spectra					
HCHO cross section included	1.00	1.00		0.96	0.98
Synthetic Spectra					
HCHO cross section included	0.97	0.99		0.94	0.97

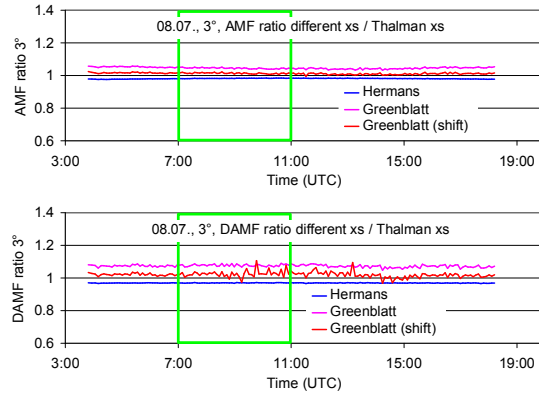
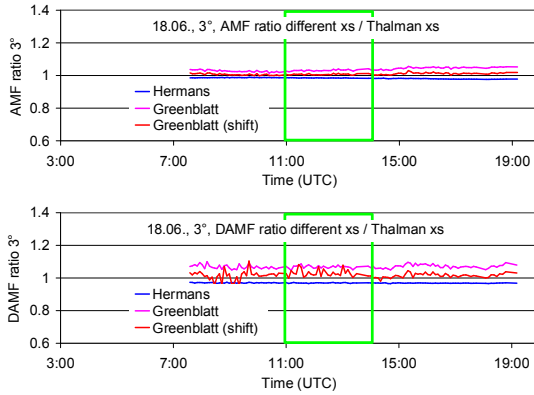
2551
 2552
 2553
 2554
 2555
 2556
 2557
 2558
 2559
 2560
 2561
 2562
 2563
 2564
 2565
 2566
 2567
 2568
 2569
 2570
 2571
 2572
 2573
 2574
 2575
 2576
 2577
 2578
 2579
 2580
 2581

18 June 2013

8 July 2013

2582

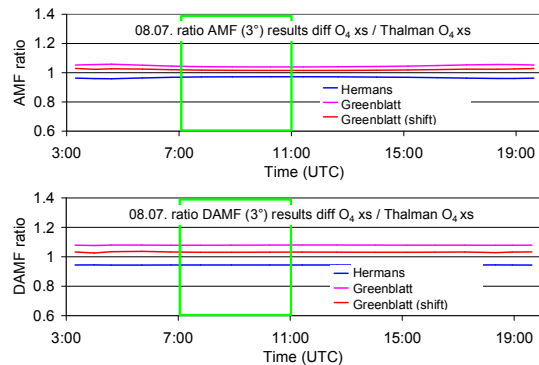
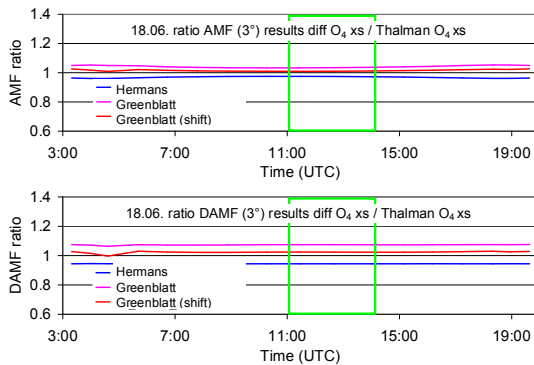
a) measured spectra



2583

2584

b) synthetic spectra



2585

2586

2587

2588

2589

2590

2591

2592

2593

2594

2595

2596

2597

2598

2599

2600

2601

2602

2603

2604

2605

2606

2607

2608

2609

2610

Fig. A24 Ratio of the O_4 (d)AMFs derived for the analyses using different O_4 cross sections versus those for the standard analysis (using the Thalman and Volkamer (2013) cross section) for both selected days (top: results for spectra measured by the MPIC instrument; bottom: results for synthetic spectra taking into account the temperature dependence of the O_4 cross section).

2611 Table A23 Average ratios of O₄ (d)AMFs derived for the analyses using different O₄ cross
 2612 section versus those for the standard analysis (using the Thalman et al. cross section) for the
 2613 standard analysis (only one O₄ cross section) for the two middle periods on both selected days
 2614 (top: results for spectra measured by the MPIC instrument; bottom: results for synthetic
 2615 spectra taking into account the temperature dependence of the O₄ cross section).

	AMF ratios			dAMF ratios	
O ₄ cross section	18 June 2013, 11:00 – 14:00	8 July 2013, 7:00 – 11:00		18 June 2013, 11:00 – 14:00	8 July 2013, 7:00 – 11:00
Measured spectra					
Hermans	0.98	0.98		0.97	0.97
Greenblatt	1.03	1.04		1.07	1.08
Greenblatt shifted	1.01	1.01		1.03	1.03
Synthetic Spectra					
Hermans	0.97	0.97		0.94	0.94
Greenblatt	1.03	1.04		1.07	1.08
Greenblatt shifted	1.01	1.02		1.02	1.03

2616
 2617
 2618

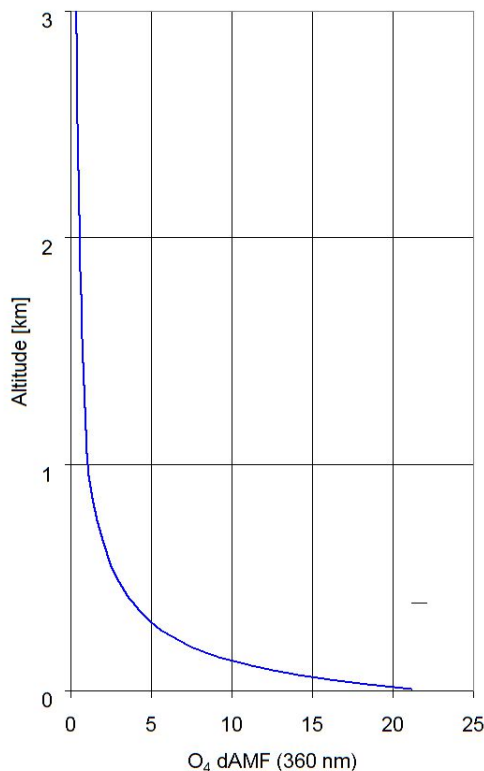


Fig. 25 O₄ differential box-AMFs (with 20m vertical resolution) used for the simulation of the temperature-dependent O₄ absorption spectra. They are averages of radiative transfer simulations for several scenarios. Simulations are performed for a surface albedo of 6 %, aerosol profiles with constant extinction between 0 and 1000m and different AOD (0.1, 0.3, 0.7) and for all combinations of SZA (40, 60°), relative azimuth angles (0, 90, 180°) and elevation angles (2° and 3°).

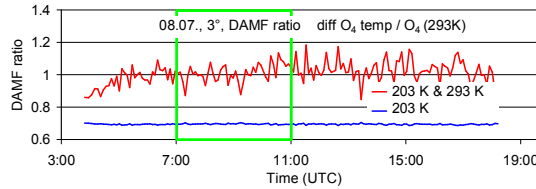
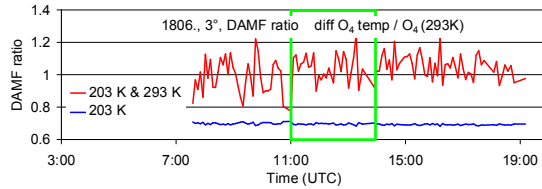
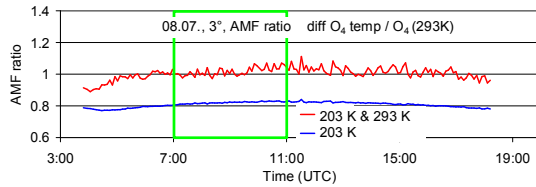
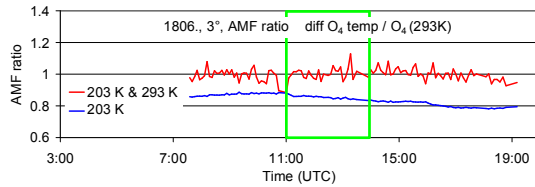
2619

18 June 2013

8 July 2013

2620

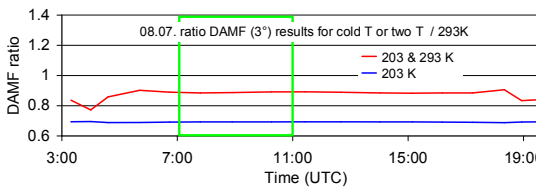
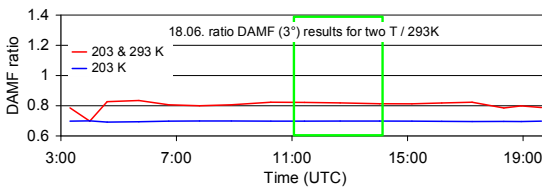
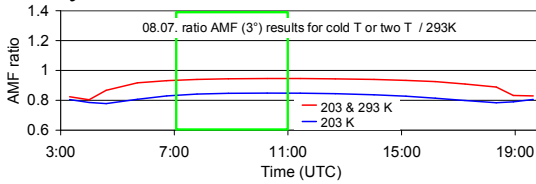
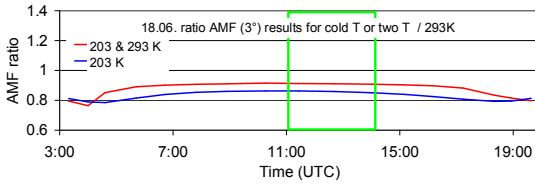
a) measured spectra



2621

2622

b) synthetic spectra



2623

2624

2625

2626

2627

2628

2629

2630

2631

2632

2633

2634

2635

2636

2637

2638

2639

2640

2641

2642

2643

2644

2645

2646

2647

2648

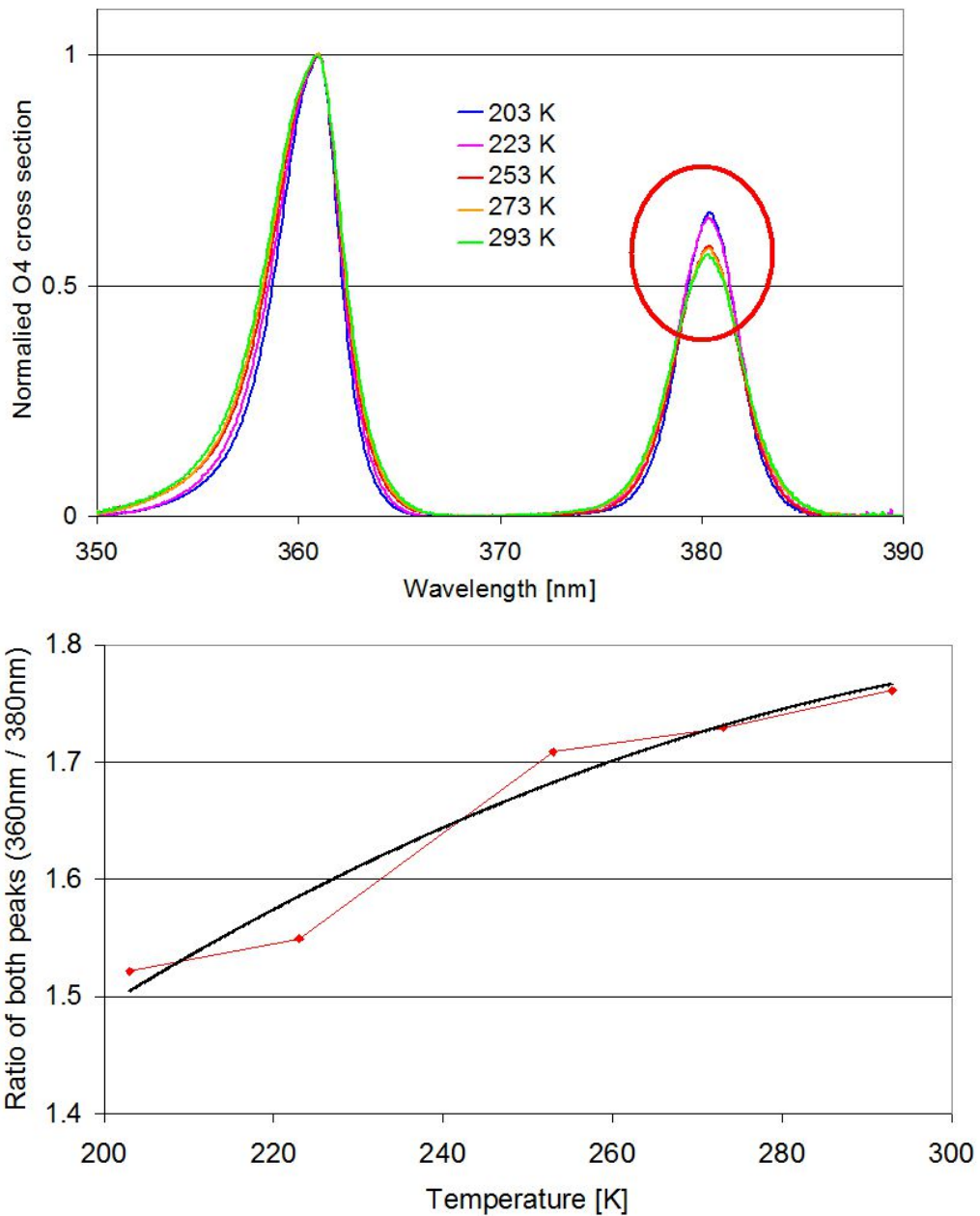
2649

Fig. A26 Ratio of the O₄ (d)AMFs derived for O₄ cross sections at different temperatures (either 203 K or both 203 and 293 K) versus those for the standard analysis (using the O₄ cross section for 293 K) for both selected days (top: results for spectra measured by the MPIC instrument; bottom: results for synthetic spectra taking into account the temperature dependence of the O₄ cross section).

2650 Table A24 Average ratios of O₄ (d)AMFs derived O₄ cross sections at different temperatures
 2651 (either 203 K or both 203 and 293 K) versus those for the standard analysis (using the O₄
 2652 cross section for 293 K) for the two middle periods on both selected days (top: results for
 2653 spectra measured by the MPIC instrument; bottom: results for synthetic spectra taking into
 2654 account the temperature dependence of the O₄ cross section). For the simultaneous fit of both
 2655 temperatures also the results for the spectral range 345 – 374 nm (one O₄ absorption band) are
 2656 included.

	AMF ratios			dAMF ratios	
O ₄ cross sections	18 June 2013, 11:00 – 14:00	8 July 2013, 7:00 – 11:00		18 June 2013, 11:00 – 14:00	8 July 2013, 7:00 – 11:00
Measured Spectra					
203 K	0.85	0.82		0.70	0.70
203 & 293 K	1.00	1.02		1.04	1.01
203 & 293 K (345 – 374 nm)	0.91	1.04		0.95	1.02
Synthetic Spectra					
203 K	0.86	0.84		0.70	0.69
203 & 293 K	0.91	0.94		0.82	0.89
203 & 293 K (345 – 374 nm)	0.99	1.00		0.99	1.00

2657
 2658
 2659
 2660
 2661
 2662
 2663
 2664
 2665
 2666
 2667
 2668
 2669
 2670
 2671
 2672
 2673
 2674
 2675
 2676
 2677
 2678
 2679
 2680
 2681
 2682



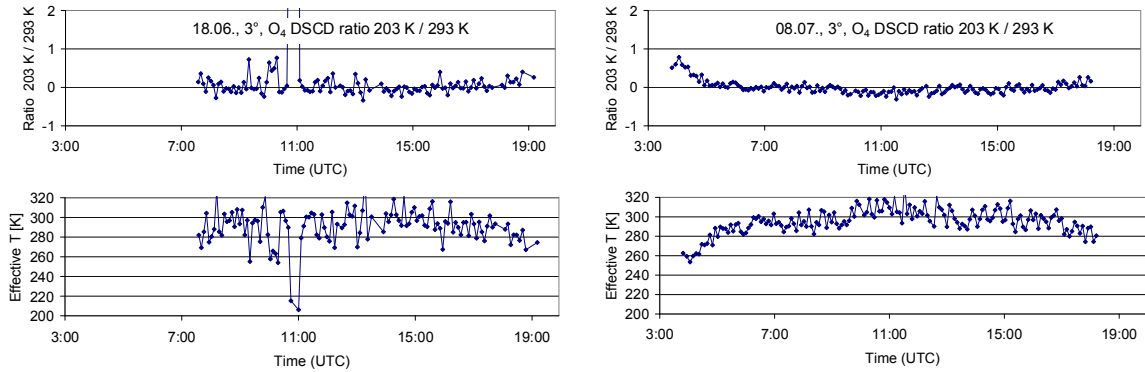
2684 Fig. A27 Top: Comparison of the O₄ cross sections from Thalman and Volkamer (2013) for
 2685 different temperatures. The cross sections are divided by the maximum values at 360 nm.
 2686 After this normalisation, the resulting values at 380 nm fall into two groups (high values for
 2687 203 & 223K, low values for 253, 273, 293K). Bottom: Ratio of the peaks of the O₄
 2688 cross section at 360 nm and 380 nm as function of temperature (red points). The black curve is a
 2689 fitted low order polynomial.
 2690
 2691
 2692
 2693
 2694
 2695
 2696

2697
2698

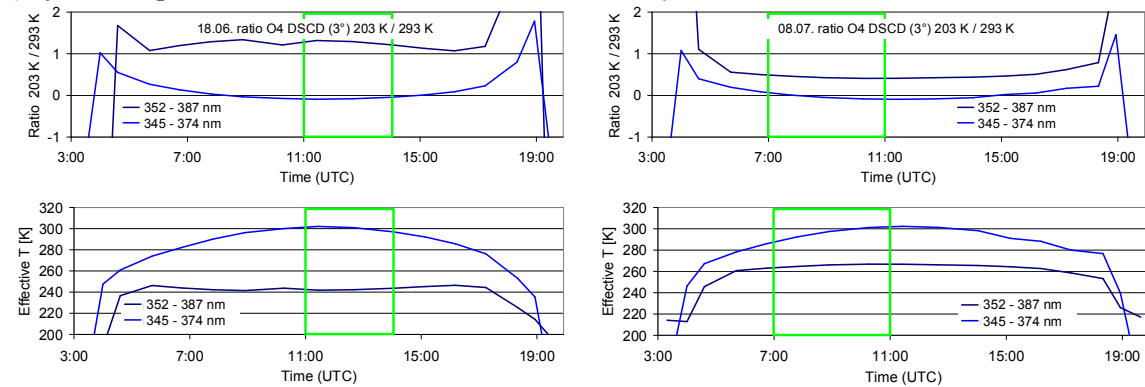
18 June 2013

8 July 2013

2699 a) measured spectra



2700 b) synthetic spectra



2701
2702
2703
2704
2705
2706
2707
2708
2709
2710
2711
2712
2713
2714
2715
2716
2717
2718
2719
2720
2721
2722
2723
2724
2725

Fig. A28 Ratio of the derived O₄ dSCDs for 203 K and 293 K as well s the derived effective temperatures for the analyses with both cross sections included.

2726
 2727
 2728
 2729
 2730
 2731
 2732
 2733
 2734

Table A25 a) Average ratios of O₄ (d)AMFs derived from the analysis of MPIC spectra by different groups versus the analysis of MPIC spectra by MPIC (standard analysis). b) Average ratios of O₄ (d)AMFs derived from spectra of other groups analysed by MPIC versus the analysis of MPIC spectra by MPIC (using the same analysis settings and spectral range: 335 – 374 nm). c) Average ratios of O₄ (d)AMFs derived from spectra of other groups analysed by the same groups using individual analysis settings versus the analysis of MPIC spectra by MPIC (standard analysis).

Measurements / Analysis	AMF ratios			dAMF ratios	
	18 June 2013, 11:00 – 14:00	8 July 2013, 7:00 – 11:00		18 June 2013, 11:00 – 14:00	8 July 2013, 7:00 – 11:00
a) MPIC spectra analysed by other groups					
BIRA	0.96	0.98		0.95	0.95
IUP-B	1.03	0.98		1.05	0.99
INTA	1.02	0.97		1.05	0.94
CMA	0.97	0.98		0.98	0.95
CSIC	0.94	0.94		0.95	0.94
b) Other spectra analysed by MPIC (335 – 374 nm)					
BIRA	0.98	0.99		0.89	0.95
IUP-B	1.05			1.07	
IUP-HD	0.97			1.00	
c) Other spectra analysed by the same groups					
BIRA	0.94	0.94		0.91	0.92
IUP-B	0.95			0.88	
IUP-HD	1.01			1.04	

2735
 2736
 2737
 2738
 2739
 2740
 2741
 2742
 2743
 2744
 2745
 2746
 2747
 2748
 2749
 2750
 2751
 2752
 2753
 2754

2755 **Appendix A5 Extraction of aerosol extinction profiles**

2756

2757 In this section, the procedure for the extraction of aerosol extinction profiles is described. The
2758 aerosol profiles are derived from the ceilometer measurements (yielding the profile
2759 information) in combination with the sun photometer measurements (yielding the vertically
2760 integrated aerosol extinction, the aerosol optical depth AOD).

2761 The ceilometer raw data consist of range-corrected backscatter profiles averaged over 15
2762 minutes. The profiles range from the surface to an altitude of 15360m with a height resolution
2763 of 15m. Here it is important to note that due to limited overlap of the outgoing Laser beam and
2764 the field of view of the telescope, no profile data is available below 180 m. The ceilometer
2765 profiles (hourly averages) are shown in Fig. A29 for both selected days.

2766 The AERONET sun photometer data provide the AOD at different wavelengths (340, 360,
2767 440, 500, 675, 870, and 1020 nm) in time intervals of 2 – 25 min if the direct sun is visible.

2768 To determine profiles of aerosol extinction from the ceilometer backscatter data, several
2769 processing steps have to be performed. They are described in the sub-sections below.

2770

2771

A) Smoothing and extrapolating of the ceilometer backscatter profiles

2772

2773 First, the ceilometer data are averaged over several hours to reduce the scatter. For that
2774 purpose on both days three time periods are identified, for which the backscatter profile show
2775 relatively small variations. The profiles for these periods are shown in Fig. A29. In addition
2776 to the temporal averaging, the profiles are also vertically smoothed above 2 km. Above
2777 altitudes between 5 to 6 km (depending on the period) the (smoothed) ceilometer backscatter
2778 profiles become zero. Thus the aerosol extinction profiles above these altitudes are set to zero.
2779 Below 180 m above the surface the ceilometer becomes ‘blind’ for the aerosol extinction
2780 because of the insufficient overlap between the outgoing laser beam and the field of view of
2781 the telescope. Thus the profiles have to be extrapolated down to the surface. This
2782 extrapolation constitutes an important source of uncertainty. To estimate the associated errors,
2783 the extrapolation is performed in three different ways:

2784

1) The value below 180 m are set to the value measured at 180m.

2785

2) The values below 180m are linearly extrapolated assuming the same slope below 180 m as
2786 between 180m and 240m.

2787

3) The values below 180m are linearly extrapolated by the double slope between 180m and
2788 240m.

2789

2790

2791

2792

2793

2794

2795

2796

2797

2798

2799

2800

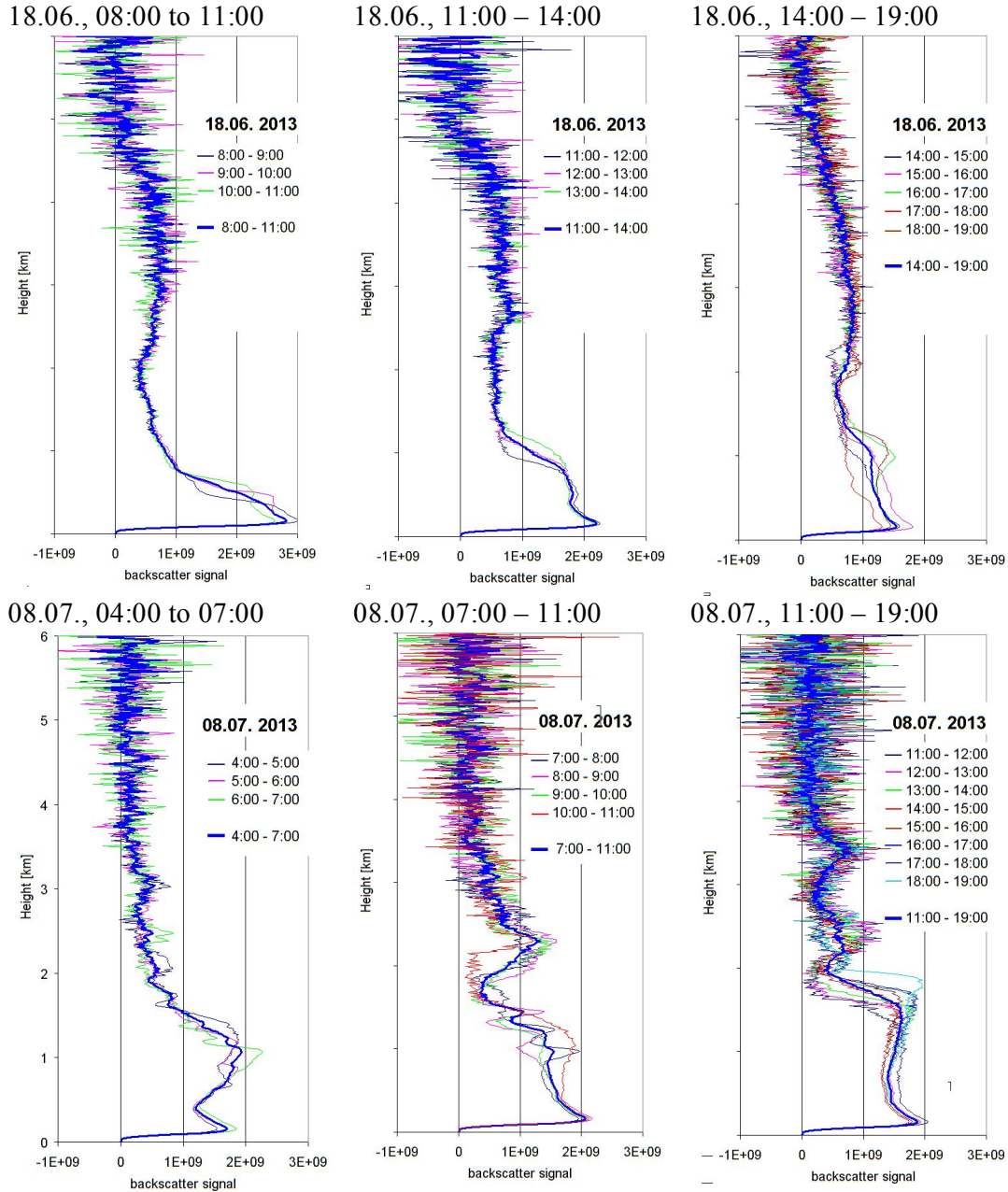
2801

2802

2803

2804

2805



2807 Fig. A29 Range-corrected backscatter profiles (hourly averages) for the three selected periods
 2808 on both days. Also the averages over the the whole periods are shown (thick lines).
 2809

2810

2811

B) Scaling of the Ceilometer profiles by sun photometer AOD at 1020 nm

2812

2813 The scaling of the ceilometer backscatter profiles by the AOD at 1020 nm is an intermediate
 2814 step, which is necessary for the correction of the aerosol self-extinction. The average AOD at
 2815 1020 nm for the different selected time periods on both days is shown in Table A26. In that
 2816 table also the average values at 380 nm are shown, which are used for a second scaling (see
 2817 below).

2818 The backscatter profiles are vertically integrated and then the whole profiles are scaled by the
 2819 ratio:

2820
2821
2822
2823
2824
2825
2826
2827
2828
2829

$$AOD_{1020nm} / B_{int} \tag{A1}$$

Here B_{int} indicates the integrated backscatter profile.

Note that the wavelength of the ceilometer measurements (1064 nm) is slightly different from the sun photometer measurements (1020 nm), but the difference of the AOD is negligible (typically < 4%).

Table A26 Average AOD at 1020 and 360 nm derived from the sun photometer.

Time	AOD 1020 nm	AOD 360 nm*
18.06.2013, 08:00 - 11:00	0.124	0.379
18.06.2013, 11:00 - 14:00	0.122	0.367
18.06.2013, 14:00 - 19:00	0.118	0.296
08.07.2013, 04:00 - 07:00	0.045	0.295
08.07.2013, 07:00 - 14:00	0.053	0.333
08.07.2013, 11:00 - 19:00	0.055	0.348

2830
2831
2832
2833
2834

*Average of AOD at 340 nm and 380 nm.

C) Correction of the aerosol extinction

2835
2836
2837
2838
2839
2840

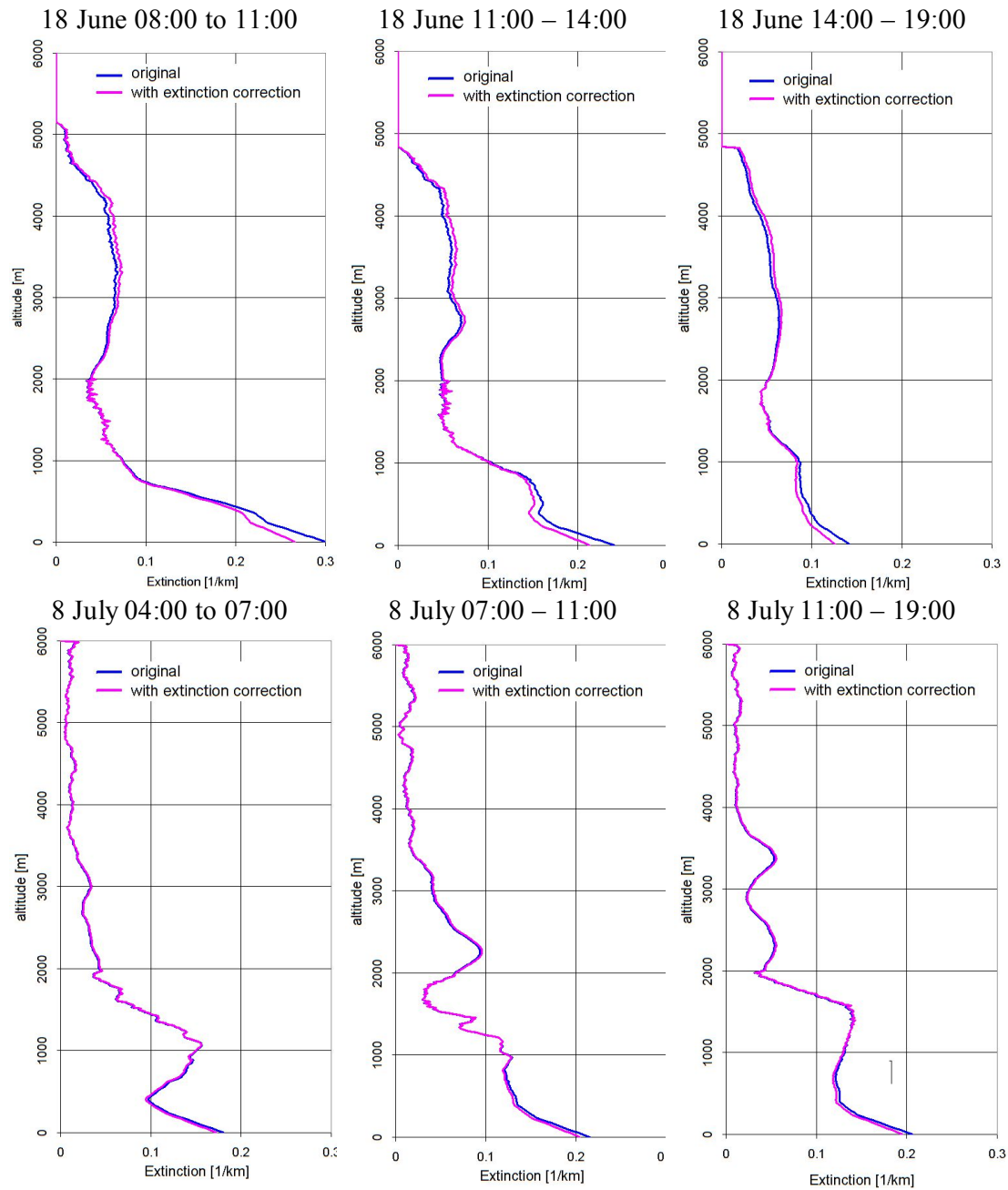
The photons received by the ceilometer have undergone atmospheric extinction. Here, Rayleigh scattering can be ignored because of the long wavelength of the ceilometer (optical depth below 2 km is < 0.001). However, while the extinction due to aerosol scattering is also small at these long wavelengths it systematically affects the ceilometer signal and has to be corrected. The extinction correction is performed according to the following formula:

2841

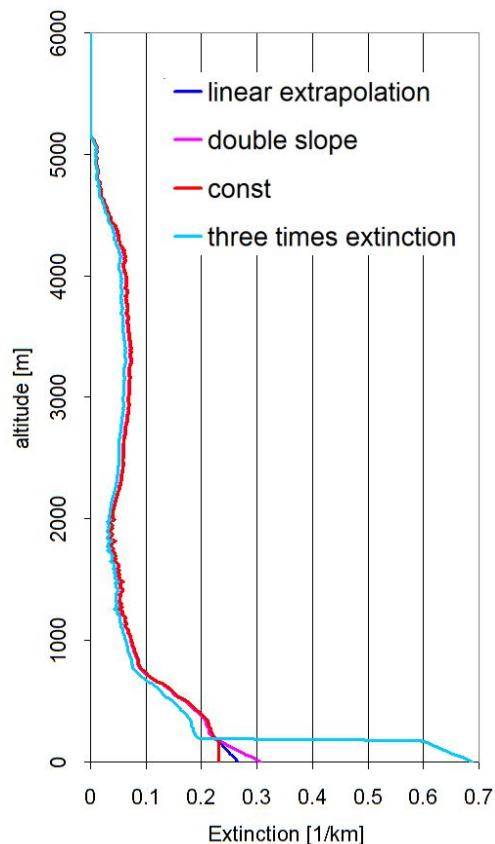
$$\alpha_{i,corr} = \frac{\alpha_i}{\exp\left(-2 \cdot \sum_{z_0}^{z_{i-1}} \alpha_{j,corr} \cdot (z_j - z_{j-1})\right)} \tag{A2}$$

2842
2843
2844
2845
2846
2847
2848
2849
2850
2851
2852
2853
2854
2855
2856
2857
2858
2859

Here α_i represent the uncorrected extinction and $\alpha_{i,corr}$ represents the corrected extinction at height layer i (with z_i is the lower boundary of that height layer). Equation C1 has to be subsequently applied to all height layers starting from the surface (z_0). Note that the factor of two accounts for the extinction both paths between the instrument and the scattering altitude (way up and down). The extinction correction is performed at a vertical resolution of 15m. After the extinction correction, the profiles are scaled by the corresponding AOD at 360 nm (see table A26 In Fig. A30 the profiles with and without extinction correction are shown. The extinction correction slightly increases the values at higher altitudes and decreases the values close to the surface. The effect of the extinction correction is larger on 18 June 2013 (up to 12 %).



2860 Fig. A30 Comparison of profiles (linear extrapolation below 180 m) without (blue) and with
 2861 (magenta) extinction correction. Both profiles are scaled to the same total AOD (at 360 nm)
 2862 determined from the sun photometer.
 2863
 2864



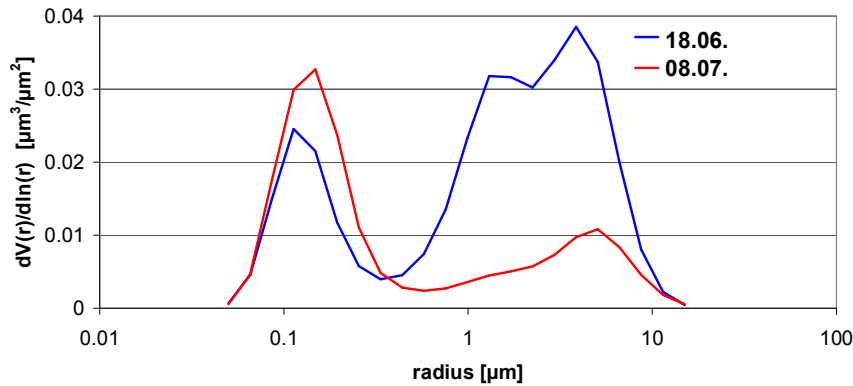
2865
 2866 Fig. A31 Aerosol profile (light blue) with extreme extinction close to the surface (below 180
 2867 m, the altitude for which the ceilometer is sensitive) extracted for the first period (8:00 –
 2868 11:00) on 18 June 2013. Also shown are the profiles extrapolated below 180 as described
 2869 above.

2870
 2871
 2872
 2873
 2874
 2875
 2876
 2877
 2878
 2879
 2880
 2881
 2882
 2883
 2884
 2885
 2886
 2887
 2888
 2889
 2890
 2891
 2892

D) Influence of a changing LIDAR ratio with altitude

For the extraction of the aerosol profiles described above, a fixed LIDAR ratio was assumed, which implies that the aerosol properties are independent from altitude. However, this is a rather strong assumption, because it can be expected that the aerosol properties (e.g. the size) change with altitude. With the available limited information, it is impossible to derive detailed information about the altitude dependence of the aerosol properties, but it can be how representative the ceilometer measurements at 1020 nm are for the aerosol extinction profiles at 360 nm. For these investigations we again focus on the middle periods of both selected days. From the AERONET Almuantar observations information on the size distribution for these periods is available (see Fig. A32). On both days two pronounced modes (fine and coarse mode) are found with a much larger coarse mode fraction on 18 June compared to 8 July. From the AERONET observations, also separate phase functions for the fine and coarse mode as well as the relative contribution of both modes to the total aerosol optical depth at 500 nm are available. On 18 June and 8 July the relative contributions to the total AOD at 500 nm are 40 % and 5 %, respectively. Assuming that the AOD of the coarse mode fraction is independent on wavelength, the relative contributions of the coarse mode at 360 nm and 1040 nm can be derived (see Table A27).

2893
2894



2895
2896
2897
2898
2899
2900

Fig. A32 Size distributions derived from AERONET Almucatar observations on 18 June (07:24 & 15:34) and 08 July (07:32 & 15:38).

Table A27 Contribution of the coarse mode to the total AOD at different wavelengths

<u>Date</u>	<u>Total AOD 360 nm</u>	<u>Total AOD 1020 nm</u>	<u>Relative contribution of coarse mode 360 nm</u>	<u>Relative contribution of coarse mode 1020 nm</u>
<u>18 June, 11:00 – 14:00</u>	<u>0.37</u>	<u>0.12</u>	<u>24.9%</u>	<u>77.7%</u>
<u>08 July, 07:00 – 11:00</u>	<u>0.33</u>	<u>0.055</u>	<u>3.0%</u>	<u>18.1%</u>

2901
2902
2903
2904
2905
2906
2907
2908
2909
2910
2911
2912
2913
2914
2915

It is found that on 18 June the coarse mode clearly dominates the AOD at 1020 nm, whereas on 8 July it only contributes about 20 % to the total AOD. As expected the relative contributions of the coarse mode to the AOD at 360 nm are much smaller (25 % and 3%). In the last step the probability of aerosol scattering in backward direction is considered, because the ceilometer receives scattered light from that direction. For that purpose the ratios of the optical depths are multiplied by the corresponding values of the normalised phase functions at 180° and in this way the relative contributions to the backscattered signals from the coarse mode for both wavelengths and both days are calculated (Table A28). Interestingly, on 8 July the contributions of the coarse mode to the backscattered signal at both wavelengths differs only by about 10%. In contrast, on 18 June the difference is much larger.

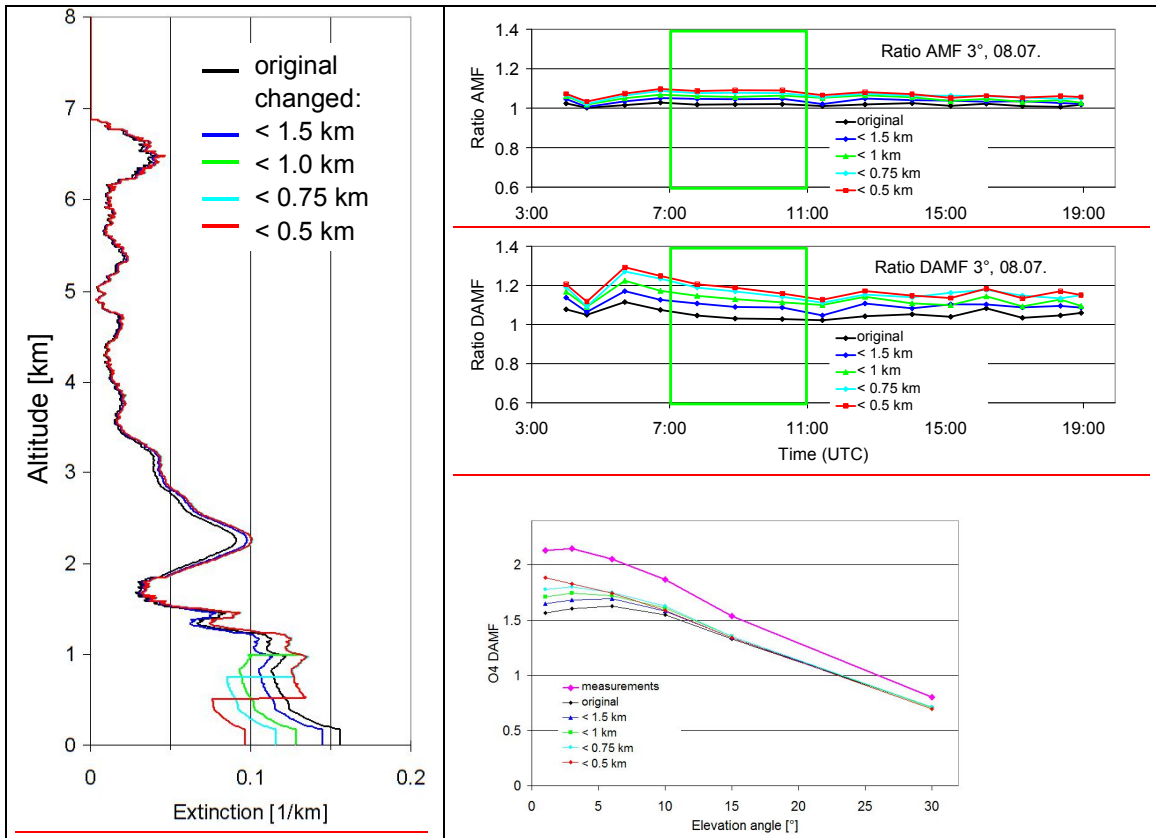
Table A28 Ratio of phase functions (coarse / fine) in backward direction and relative contribution of coarse mode to the backscattered signal at both wavelengths

<u>Date</u>	<u>Ratio phase function at 360 nm</u>	<u>Ratio phase function at 1020 nm</u>	<u>Relative contribution of coarse mode at 360 nm</u>	<u>Relative contribution of coarse mode at 1020 nm</u>
<u>18 June, 11:00 – 14:00</u>	<u>1.13</u>	<u>0.61</u>	<u>27.3%</u>	<u>68.0%</u>
<u>08 July, 07:00 – 11:00</u>	<u>2.7</u>	<u>0.99</u>	<u>7.8%</u>	<u>18.0%</u>

2916
2917
2918
2919

For 8 July, the results can be interpreted in the following way: at 360 nm the aerosol profiles extracted as described above overestimate the contribution from the coarse mode by about

2920 10%. To estimate the effect of this overestimation we construct modified aerosol extinction
 2921 profiles, in which 10% of the total AOD is relocated. Since we expect that the coarse mode
 2922 aerosols are usually located at low altitude, we construct 4 different modified profiles (see
 2923 Fig. A33) with different altitudes (1.5 km, 1 km, 0.75 km, or 0.5 km), below which 10% of
 2924 the aerosol extinction is relocated to altitudes above (assuming that the coarse mode aerosol is
 2925 only located below these altitudes). Of course, such a sharp boundary is not very realistic, but
 2926 it allows to quantify the overall effect of the relocation. Here it should be noted that we
 2927 selected the aerosol profile for 8 July extracted by INTA which reached up to 7 km (see Fig.
 2928 9).
 2929



2930 Fig. A33 Left: Modified aerosol profiles for 08 July assuming that the coarse mode aerosol is
 2931 only located in the lowest part of the atmosphere. Top right: ratios of the (d)AMFs calculated
 2932 for the modified profiles compared to the dAMFs for the standard settings. With decreasing
 2933 layer height the (d)AMFs increase systematically, because the aerosol extinction close to the
 2934 surface decreases. Right bottom: comparison of the measured elevation dependence of the O₄
 2935 dAMFs for the period 7:00 – 11:00 on 8 July and simulation results for the different profiles.

2936
 2937
 2938 Table A29 Ratio of the (d)AMFs for the modified profiles versus those of the standard
 2939 settings

	<u>original</u> <u>INTA</u>	<u>coarse mode</u> <u>below 1.5 km</u>	<u>coarse mode</u> <u>below 1 km</u>	<u>coarse mode</u> <u>below 0.75 km</u>	<u>coarse mode</u> <u>below 0.5 km</u>
<u>AMF</u>	<u>1.02</u>	<u>1.04</u>	<u>1.05</u>	<u>1.06</u>	<u>1.08</u>
<u>dAMF</u>	<u>1.04</u>	<u>1.09</u>	<u>1.13</u>	<u>1.17</u>	<u>1.18</u>

2940
 2941 For all modified profiles, a systematic increase of the O₄ (d)AMFs compared to those for the
 2942 standard settings is found. For the O₄ dAMFs this increase can be up to 18 % (see Table A29.

2943 From the comparison of the elevation dependence of the measured and simulated O₄ dAMFs
2944 (see Fig. A33), we conclude that the aerosol profile with the coarse mode aerosol below 0.75
2945 km is probably the most realistic one. The main conclusion from this section ist that the
2946 dAMFs for 8 July derived from the standard settings probably underestimates the true dAMF
2947 by about 15 ±5 %.

2948 For 18 June we did not perform similarly detailed calculations, because on that day the
2949 uncertainties of the aerosol extinction profile caused by the missing sensitivity of the
2950 ceilometer below 180 m are much larger than on 8 July. On 18 June also the magnitude of the
2951 relocation of the aerosol extinction between different altitudes would be much larger than on
2952 8 July.

2953
2954
2955
2956

2957 Appendix A6 Influence of elevated aerosol layers on the O₄ (d)AMF

2958
2959
2960
2961
2962
2963
2964
2965
2966
2967

Ortega et al. (2016) showed that for their measurements the consideration of elevated aerosol
layers (between about 3 and 5 km) is essential to bring measured and simulated O₄ (d)AMFs
into agreement. In our study, we consider aerosol layers over an even larger altitude range (up
to 7 km). Nevertheless, it is interesting to see how the simulated O₄ (d)AMFs change if the
extinctions at various altitude ranges are changed systematically. Here we chose the aerosol
extinction profile extracted by INTA for the period 7:00 to 11:00 on 8 July, because it
contains substantial amounts of aerosols in elevated layers (see Fig. 9). During that period
three distinct aerosol layers can be identified (see Table A30).

2968

Table A30 Selection of different aerosol layers on 08 July (07:00 – 11:00)

<u>layer</u>	<u>AOD</u>	<u>Relative contribution</u> <u>to total AOD</u>
<u>0 – 1.68 km</u>	<u>0.186</u>	<u>55.4 %</u>
<u>1.68 – 4.9 km</u>	<u>0.116</u>	<u>34.5 %</u>
<u>4.9 – 7 km</u>	<u>0.035</u>	<u>10.4 %</u>

2969
2970
2971
2972
2973
2974
2975
2976
2977
2978
2979
2980
2981
2982
2983
2984
2985
2986
2987
2988

Then, the extinction of the individual aerosol layers were increased by either 20 % or 40 %
compared to the original profile. These profiles (referred to as ‘without scaling’) were used
for the simulation of O₄ (d)AMFs). A further set of O₄ (d)AMFs was simulated for the same
profiles, after they were scaled by a constant factor to match the AOD of the original
extinction profile (referred to as ‘with scaling’). The modified profiles and the ratios of the
corresponding O₄ DAMFs versus the O₄ dAMFs of the original profile are shown in Fig. A34.
For the unscaled profiles the O₄ dAMFs strongly decrease (by about 30%) if the extinction in
the lowest layer is increased. If the extinction in the middle or upper layer is increased a slight
increase (about 3 %) of the O₄ dAMFs is found. For the scaled profiles different results are
found, because the increase of the extinction in one layer is now balanced by a decrease of the
aerosol extinction in the other layers. If the extinction in the lowest layer is increased by
40%, the O₄ dAMFs still decrease, but only by about 7%. If the extinction in the middle or
upper layer is increased the O₄ dAMFs increase by about 3 % and 7 %, respectively.

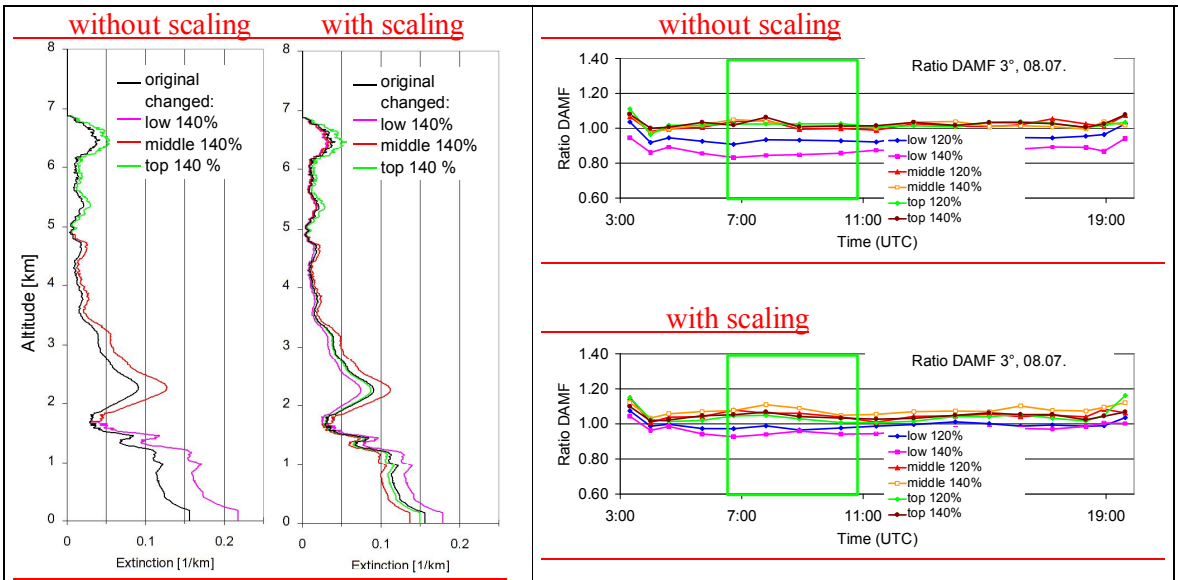


Fig. A34 Left: Aerosol profiles used for the simulations (see text). Right: Ratios of the O_4 (d)AMFs simulated for the modified profiles versus those of the original profile.

2989
 2990
 2991
 2992
 2993
 2994
 2995
 2996
 2997
 2998
 2999
 3000
 3001
 3002